Air motions and precipitation growth in Alpine storms

Socorro Medina

A thesis submitted in partial fulfillment
of the requirements for the degree of

Master of Science

University of Washington

2002

Program Authorized to Offer Degree: Atmospheric Sciences

University of Washington

Graduate School

This is to certify that I have examined this copy of a master's thesis by

Socorro Medina

and have found that it is complete and satisfactory in all respects,
and that any and all revisions required by the final
examining committee have been made.

Committee Members:

_____

Marcia B. Baker

_____

Robert A. Houze

_____

Clifford F. Mass

_____

Sandra E. Yuter

Date: _____

In presenting this thesis in partial fulfillment of the requirements for a Master's degree at the University of Washington, I agree that the Library shall make its copies freely available for inspection. I further agree that extensive copying of this thesis is allowable only for scholarly purposes, consistent with "fair use" as prescribed in the U.S. Copyright Law. Any other reproduction for any purpose or by any means shall not be allowed without my written permission.

Signature_____

Date_____

TABLE OF CONTENTS

LIST OF FIGURES

LIST OF TABLES

Chapter 1

INTRODUCTION

1.1 Alpine precipitation climatology

This thesis investigates orographic precipitation mechanisms over large mountains. It exploits data obtained recently over the European Alps during the Mesoscale Alpine Program (MAP, Bougeault et al. 2001).

Some past studies have focussed on rainfall over small hills. Bergeron (1965) described the mechanism known as seeder-feeder by which a feeder cloud formed over a small hill enhances the seeder precipitation falling from a cloud located aloft. Hill et al. (1981) studied the orographic precipitation over the hills of Southern Wales. These hills have a maximum height of about 600 m, and precipitation tends to be maximum at hilltop. The physical processes producing the orographic enhancement take place in the lowest 1.5 km above the hills.

The patterns and processes of orographic precipitation over large mountains are different from those over small hills. In his extensive review on the influence of mountains on the atmosphere, Smith (1979) noted considerable scatter in the frequently assumed linear relationship between annual average precipitation and station elevation. He pointed out that the amount of scatter present results from factors including weather type, temperature, humidity, wind speed, wind direction, and size and shape of surrounding topography. He further suggested that on very high mountains the

rainfall may increase up to a certain height and then decrease.

One mountain range where this pattern occurs is the European Alps. The Alps constitute a long and tall mountain range over central Europe (Fig. 1.1). The Alpine barrier is 800 km long and between 200-300 km wide, with crest-line heights ranging between 3 and 5 km. The Maritime Alps constitute the southernmost segment of the barrier, located on the border between France and Italy. The Apennines extend along the Gulf of Genoa coast all the way down into southern Italy. The large plain between the Apennines and the Alps is known as the Po Basin or Po Valley. The Alpine region has two major moisture sources: the Adriatic and Ligurian Seas, located to the east and west of the Italian peninsula, respectively. The Dinaric Alps are located along the eastern coast of the Adriatic Sea. The Mediterranean Sea, extending across southern Europe constitutes the broader moisture source for the region.

Frei and Schär (1998) used daily rain-gauge data for 1971-1990 to construct a high-resolution precipitation climatology for the Alpine region. They found that the mean annual precipitation climatology includes maxima along the northern and southern rims of the Alps, local maxima over the Apennines and the Dinaric Alps and a minimum over the barrier crest (Fig. 1.2), as suggested by Smith (1979). This thesis focuses on the precipitation distribution over the southern rim of the Alps. This region has an autumn (September, October and November) maximum of precipitation. Frei and Schär's (1998) autumn climatology (Fig. 1.3) shows a reduced maximum on the northern rim of the Alps, which is generally in a rain shadow area during autumn storms, which have strong southerly to southeasterly flow at low levels ahead of baroclinic troughs. The maxima along the southern rim of the Alps are more pronounced, especially over the Lago Maggiore region and the region of Friuli (Fig. 1.1). The two precipitation maxima on the Mediterranean side of the Alps coincide with regions where the horizontal profile of the barrier has a concave shape (see the 800 m MSL

terrain contour in Fig. 1.3), suggesting that the orography is concentrating the flow and precipitation over those regions. Most of the material presented in this study focuses on the westernmost maximum on the southern slopes of the Alps: the Lago Maggiore region.

Disastrous floods are not uncommon over the southern rim of the Alps during the autumn season (e.g. Buzzi et al. 1995, Buzzi and Tartaglione 1995, Lionetti 1996). The need to understand and forecast these floods was the primary motivation for MAP. Particular attention has been paid to the "Piedmont Flood", which occurred in the region of that name (Fig. 1.1) in November 1994. This flood produced rain accumulations as high as 300 mm over a 36 h period at some stations (Buzzi et al. 1995) and extensive damage. The most recent devastating flood in this region occurred in October 2000, with one station accumulating ∼700 mm over 4 days (Gabella and Mantonvani, 2001). Some of the most important findings from past studies of Alpine floods are reviewed in the next section.

1.2 Alpine floods

Previous studies point out the meteorological and geographical factors that contribute to intense precipitation events and flooding over the Alps. These include the height of the terrain, the strength of the wind, and the thermodynamic properties of the upstream flow. The following three subsections are organized around these factors.

1.2.1 Orography

The nature of the orography has been recognized as an important factor in determining the behavior of the flow. A region's orography is specified by its height, width, shape and height gradients. The role that some of these parameters play in Alpine floods has been studied by conducting numerical simulations.

Model simulations of the Piedmont flood case have shown that a partial removal of the orography in an area of about 400 km radius around Piedmont, was sufficient to suppress almost all the precipitation in the region affected by flooding (Buzzi and Tartaglione 1995, Buzzi et al. 1998). When the Alps were almost completely removed (land surface set to a uniform height of 100 m), only modest amounts of precipitation accumulated upwind of where the Alps would be (Ferretti et al. 2000). These simulations quantified the obvious fact that the lifting of air over the barrier is of major importance during heavy precipitation events over the Alps.

By comparing model simulations done with two different horizontal resolutions, several studies have found that the high resolution grid is essential to produce a realistic amount and reasonable distribution of precipitation (Paccagnella et al. 1995 used grids with 40 and 20 km horizontal resolution. Ferretti et al. 2000 used 30 and 10 km grids). The predicted maximum value is particularly sensitive to the model resolution. These studies indicate that the orographic gradients play an important role in the accurate simulation of the precipitation. In this study, we will explore specific mechanisms to determine how the high resolution topography modifies the precipitation.

Since the highest rain accumulation during the 4-6 November 1994 flood occurred over Piedmont, i.e. the region where the Alps curve toward the south (Fig. 1.1), some model studies have been conducted to evaluate the role that the shape of the barrier plays in concentrating the flow (Schneidereit and Schär 2000, Rotunno and Ferretti, 2001). Both studies compared the results obtained with two different idealized mountain-range shapes: an elongated range, composed of a barrier-like obstacle with a straight east-west ridge line of constant height; and an L-shaped range, in which the east-west ridge line curved sharply toward the south on its west end. They

concluded that this southward bend of the L-shaped idealized Alps (compared with the east-west idealized ridge) induced little qualitative change in the flow or precipitation on the windward side. Rotunno and Ferretti (2001) suggested that an east-west moisture gradient was responsible for the observed flow and precipitation asymmetry (see section 1.2.3).

1.2.2 The wind field

The synoptic condition prevailing during the Piedmont flood, and during most of the intense precipitation events over the southern slopes of the Alps, consists of a narrow, deep and elongated upper-level trough extending north-south from the British Isles to northern Africa (Massacand et al. 1998, e.g. Fig. 4.1a from one of the case studies to follow). Connected with this trough at lower levels is strong southerly flow that advects moisture from the Ligurian Sea toward the Alps (Buzzi et al. 1998, Doswell et al. 1998, Lionetti 1996).

Early studies of the Piedmont flood (Binder and Rossa 1995 and Buzzi et al. 1995) noted that the precipitation was maximum where low-level (10 m) easterly flowing air over the Po Valley converged with low-level southerly airflow from the Ligurian Sea, where the air took on moisture. The explanation of Binder and Rossa (1995) and Buzzi et al. (1995) is partially correct. However, to fully understand the behavior of the low-level flow it is necessary to consider the thermodynamic character of the event.

1.2.3 Thermodynamic factors

In theory, flow is blocked by a 2-D obstacle when the Froude number of the upstream flow is less than 1 (see Durran 1990 or Ch. 12 of Houze 1993). The Froude (Fr) is calculated as:

$$Fr = \frac{U}{HN} \tag{1.1}$$

where U is the wind speed of the flow in the direction perpendicular to the barrier, H is the height of the barrier, and N is the Brunt-Väisälä frequency of the incoming flow. When the air is unsaturated, the Brunt-Väisälä frequency is given by:

$$N_d = \left[g \frac{dln\theta}{dz} \right]^{1/2} \tag{1.2}$$

where θ is the potential temperature, g is the gravitational acceleration, and z is height. According to Durran and Klemp (1982) when the atmosphere is saturated but the water is distributed in very small droplets which do not precipitate and do not exert inertial drag, the effective Brunt-Väisälä frequency (N_m) changes to:

$$N_m = \left[\frac{g}{T} (\frac{dT}{dz} + \Gamma_m)(1 + \frac{Lq_s}{RT}) - \frac{g}{1 + q_w} \frac{dq_w}{dz} \right]^{1/2} \tag{1.3}$$

where T is the Temperature, Γ_m is the saturated adiabatic lapse rate, q_s is the saturation mixing ratio, q_w is the total water mixing ratio ($q_w = q_s + q_l$, where q_l is the liquid water mixing ratio, since information about q_l is not standard in soundings, it was assumed to be zero). L is the latent heat of vaporization and R is the ideal gas constant for dry air. Since in a saturated atmosphere upward displacements produce condensation and latent heating that partially compensate the cooling produced by adiabatic expansion (and likewise, downward displacements produce evaporation and latent heat absorption that partially compensates the adiabatic heating), the effective Brunt-Väisälä frequency is lower when the atmosphere is saturated than when it is dry. Then by Eq. 1.1, a flow with wind speed U impinging over terrain of characteristic height H will have a higher Froude number if saturated than if dry.

Buzzi et al. (1998) studied the Piedmont flood focusing on the flow close to the surface. They were interested in the effects of the condensational latent heating on

the wind regime and precipitation accumulated during the storm. Their methodology consisted of comparing a control simulation with an experiment where the temperature tendencies due to condensation were eliminated. Their control experiment showed a low-level easterly flow over the Po Valley that rose over the Alpine terrain in the Piedmont region. Convergence was enhanced in this region, where the easterly flow met a strong southeasterly moist flow advancing from the Ligurian Sea. On the other hand, the simulation in which the temperature tendencies associated with condensation were eliminated, but the formation and fall of precipitation were allowed, produced a low-level easterly flow south of the western Alps. This flow turned northerly over Piedmont, so that it was not rising over the terrain. Hence, in the control experiment, there was a "flow over" regime in contrast to the case with no condensation where a "flow around" regime developed at low levels upstream of the mountains. Since moist southeasterly flow was still present in the experiment with no condensational heating, convergence was produced over the western Alps, where the southeasterly flow met the blocked northerly flow. Therefore, the precipitation maximum moved upstream of the position it held in the control experiment, and rainfall lowered to 30% of the reference value. The reduction of the precipitation was related to the flow not rising over the terrain. Buzzi et al. (1998) concluded that the latent heat of condensation on the upstream side of the orography favored flow over by decreasing the effective stability of the ascending flow. Later in this thesis, we will examine observational evidence of two intense precipitation events that resemble Buzzi et al.'s modeled "flow over" and "flow around" regimes.

Rotunno and Ferretti (2001) provided a thermodynamic explanation for the flow behavior described kinematically by Binder and Rossa (1995) and Buzzi et al. (1995). They proposed that the surface southeasterly moist flow described by Buzzi's et al. (1998) control case rose over the surface easterly flow over the western Alps. They argued that the easterly flow effectively modified the topography by extending the

effect of the Alps farther to the south and also by increasing the slope over which the southerly flow rose, which in turn produced higher precipitation rates. Rotunno and Ferretti (2001) showed that in the Piedmont flood case, the moist southerly air impinging on the Alps became progressively drier with distance eastward. Hence on the west side, the high values of the Froude number in the moist airstream allowed the flow to go over the barrier while the stronger stability air to the east produced stronger easterly flow perturbation, which converged with and ran under the moist southerly flow from the Ligurian Sea. The western moist saturated part of the airstream flowed over, while the eastern dry and stable part was deflected westward around the obstacle, and under the rising southerly flow, so convergence was produced between the airstreams over Piedmont, where the southerly flow rose over the easterly flow.

1.3 Precipitation mechanisms in orographic regimes

A flood like the one that occurred over Piedmont in November 1994, capable of producing abundant precipitation accumulations in a relatively short time (300 mm/36 h, Buzzi et al. 1995), is likely to have been produced by very efficient precipitation growth mechanisms. According to Rogers and Yau (1989), the precipitation efficiency describes how effectively a cloud converts either vapor or condensed material to precipitation. We will use the latter definition: efficiency equals observed rain over condensed water. Smith (1979) noted that the efficiency of precipitation release during orographic lifting by this definition depends both on the net vertical flux of air and on the microphysical processes leading to the formation of hydrometeors. Browning et al. (1975) found that storms with a large precipitation efficiency ($\sim$70%) were characterized by a strong, moist low-level jet directed against the mountain slope, by an incident airstream already near saturation and by some condensation occurring above the freezing level, which allowed ice-phase process to contribute to the precipi-

tation. On the other hand, the cases that Browing et al. found to have low efficiencies (<30%) were characterized by initially unsaturated air requiring some finite ascent before condensation began, and sometimes there was little or no condensation above the freezing level.

In an examination of winter precipitation in maritime airflow over the Cascade Mountains of Washington, Hobbs (1975) found that in post-frontal conditions, unstable cases were characterized by moderately or heavily rimed crystals and graupel, whereas unrimed to lightly rimed crystals predominated in stable conditions. Using aircraft measurements at 3 km altitude made during wind with a westerly component crossing a north-south barrier, Hobbs (1975) described cloud and precipitation particle types during winter precipitation on either side of the mountain range, which was perpendicular to the air flow. He noted that the liquid water content had a maximum on the western (upslope) side. He also found that during westerly flow, supercooled water droplets generally dominated over ice particles on the upslope side of the mountain range and that the reverse held on the lee side. Hobbs et al. (1973) used an orographic cloud model to show that in westerly wind regime, rimed particles were more likely to reach the ground on the upslope side while unrimed particles tended to be advected to the lee side before falling out.

1.4 Objectives of this study

The Special Observing Period (SOP) of MAP was held over the European Alps from 7 September to 15 November 1999. Whenever a major weather event was forecast, an Intense Observation Period (IOP) was declared, and a comprehensive set of data was obtained. Fourteen MAP Intense Observation Periods had systems or events producing large precipitation amounts over the Alpine region. The data collected during these events is used in this thesis to achieve the following objectives:

1. The first objective is to document the radar-derived three-dimensional structure of the precipitation and its accompanying airflow during the autumn season over the Lago Maggiore region. This thesis further analyzes how the characteristics of the upstream flow relate to the precipitation distribution and local airflow over the Lago Maggiore region. In particular, the effect of low and high Froude number flow (blocked and unblocked, respectively) on the precipitation and local airflow over the region of interest will be studied.

2. Buzzi et al.'s (1998) numerical simulations of Alpine storms suggest that the nature of the flow (blocked or unblocked) is critical in determining the precipitation accumulation and distribution. This thesis investigates to what extent blocked and unblocked flows occurred in the MAP storms and determined the type, amount, and efficiency of precipitation. Two particular IOPs prove to be instructive in documenting the main dynamic and precipitation processes active during unblocked and blocked regimes: IOP2b (1300 UTC 19 September to 0100 UTC 21 September 1999) and IOP8 (1200 UTC 20 October to 2200 UTC 21 October 1999). Each of these events was associated with the passage of a strong baroclinic wave, with low-level upstream flow ($\sim$850 hPa) generally from the southeast. Despite this basic large-scale similarity above the lowest kilometer of the atmosphere, the precipitation distribution differed markedly between the two cases, suggesting different flow regimes at the lowest levels (below $\sim$850 hPa): flow up and over (or unblocked) in the first case and flow around (or blocked) in the second case. The second objective is to document the low-level flow differences between these events, on the synoptic and large mesoscale.

3. This study extends downscale from the synoptic and mesoscale to examine the spatial (horizontal and vertical) structure of the airflow and hydrometeor fields on scales small enough to relate them to the detailed topography of individual peaks and

valleys on the windward slope of the Alpine terrain. As was discussed in section 1.3, the mechanisms by which precipitation typically grows should be an essential part of any flooding study, yet this has not been addressed for the Alps prior to MAP since high-resolution data are required, both for airflow and microphysics. This part of the study therefore relies primarily on data collected by several radars deployed over the area of interest during MAP. Radar is an ideal tool to study rain over topography since it samples the hydrometeor and airflow fields at exactly the same time and with the same coverage and high resolution in four dimensions. Since one of the radars used in MAP obtained radar measurements at both horizontal and vertical polarization, this study further is able to document the predominant types of hydrometeors producing the radar echo patterns. This study investigates the spatial distribution of the polarimetric-radar-identified hydrometeors with respect to the local terrain and airflow regime.

4. This thesis concludes by proposing conceptual models of orographic precipitation mechanisms active during Alpine autumn precipitation events. These conceptual models synthesize a new understanding of how the dynamics of the flow, the microphysical processes, and the detailed topography are interrelated in heavy orographic precipitation.

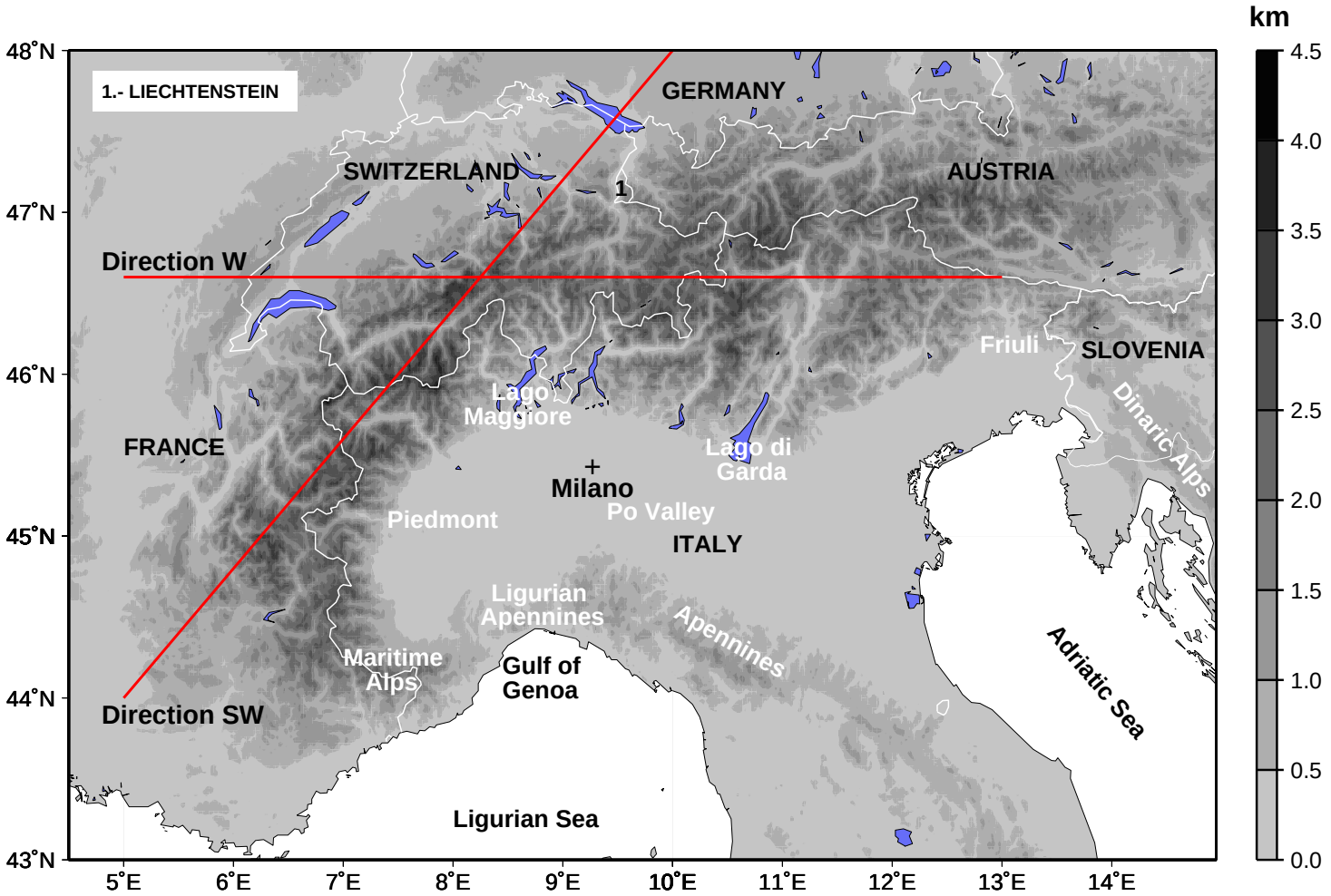

Figure 1.1: Topography and geographic features around the Alps. The chosen characteristic orientations of the Alps around Lago Maggiore used to construct the perpendicular wind profiles in Figs. 4.13 and 4.14 are also shown.

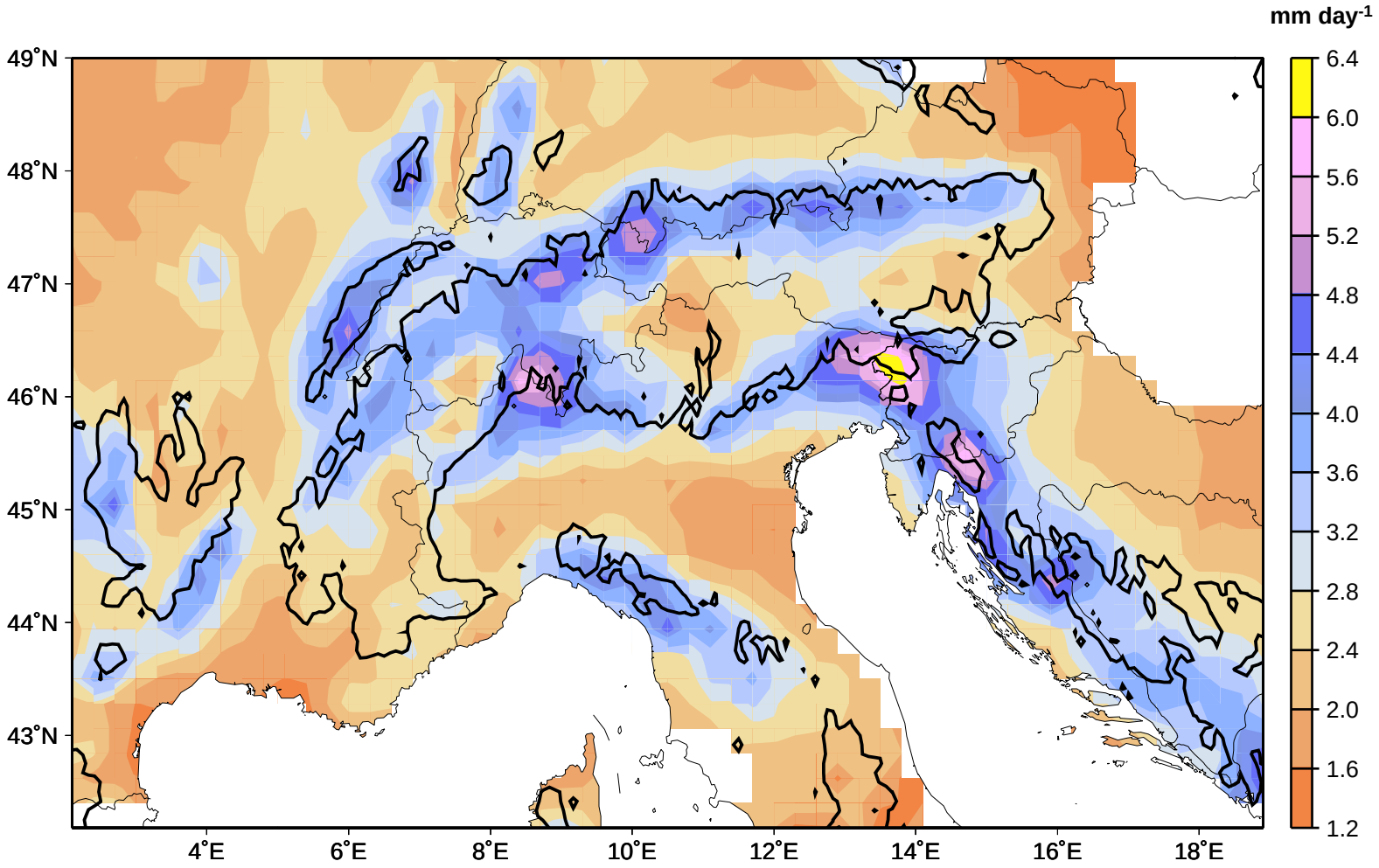

Figure 1.2: Annual precipitation climatology (after Frei and Schär, 1998).

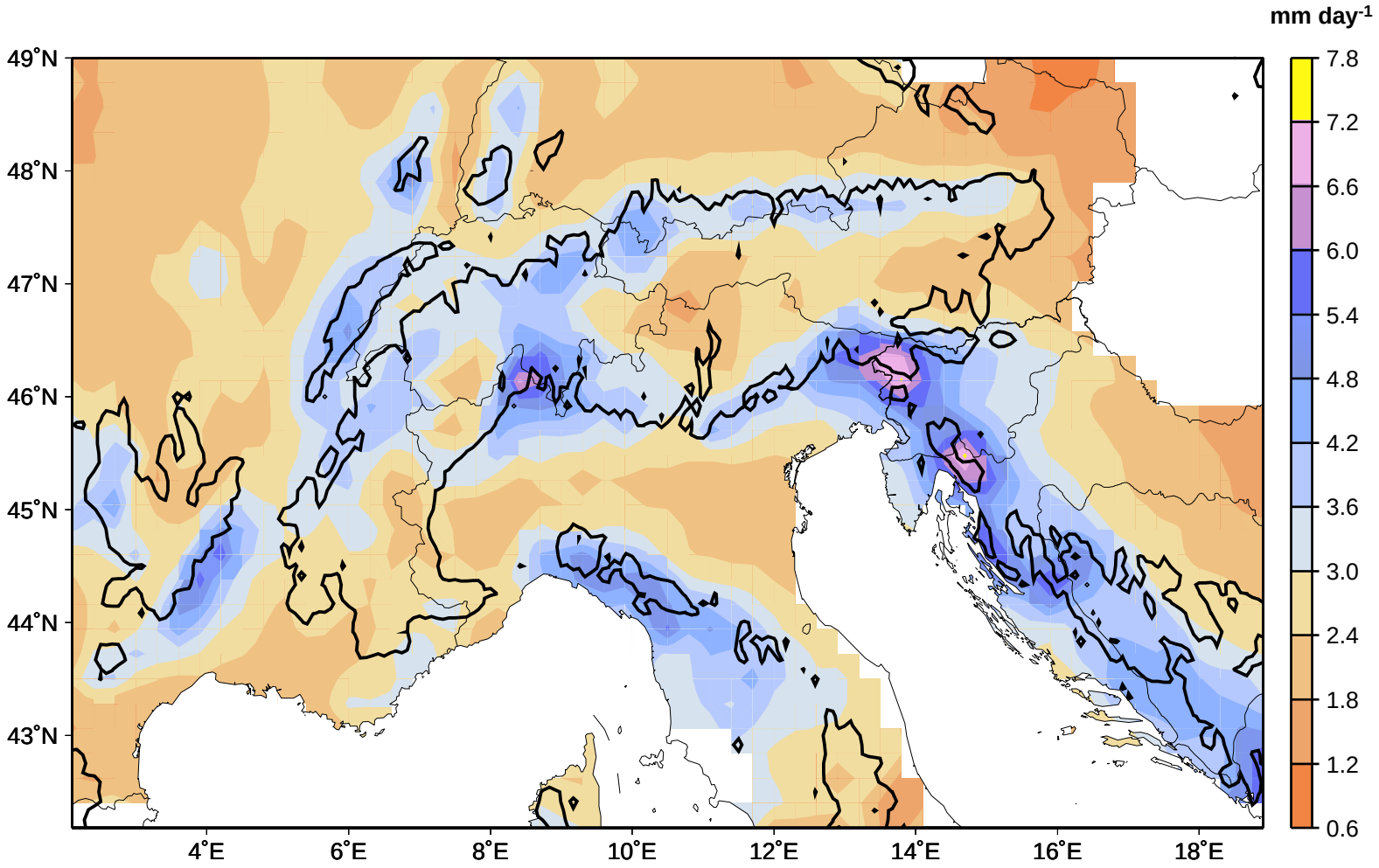

Figure 1.3: Autumn precipitation climatology (after Frei and Schär, 1998).

Chapter 2

DATA

This study emphasizes the use of radar data to determine the relationship of airflow and precipitation microphysics to the Alpine topography in the Lago Maggiore region. MAP employed seven ground-based radars and two airborne radars in a coordinated network. To establish the context of the radar data, the thesis refers to rain gauge data, sounding data, satellite imagery, and output from numerical forecast models. This chapter briefly describes these resources. Methods used to analyze the information derived from these resources will be discussed in later chapters.

2.1 Radar data

The primary data for this study are from three of the ground-based scanning Doppler radars deployed in MAP, the NCAR S-Pol radar, the Swiss Monte Lema radar, and the French RONSARD. Fig. 2.1 shows the area of focus of this study, the Lago Maggiore (LM) region. The location of the MAP radars in relation to the terrain is also shown in Fig. 2.1. Table 2.1 lists the principal characteristic of the radars. The S-Pol and RONSARD were installed especially for the MAP field phase, while the Monte Lema radar is a permanent facility of the Swiss Meteorological Institute. The Monte Lema radar antenna is located at an altitude of 1.63 km MSL, therefore the lowest scan is generally above 1.5 km. Hence the 2.0 km level is about the lowest available grid level that can be obtained after the polar-coordinate data have been interpolated to a Cartesian grid. The S-Pol radar was located at an altitude of 0.28 km MSL

and the RONSARD at 0.155 km MSL. Data from these two radars supplemented the Monte Lema radar by providing data at lower altitudes, by scanning farther south over the Po Valley than the Monte Lema radar (Fig. 2.1), and by providing the opportunity to construct dual-Doppler wind fields. The S-Pol is a dual-polarization radar, which provides information on particle type (Vivekanandan et al. 1999, Zeng et al. 2001).

Three-dimensional scans of radar data were recorded every 5 min for Monte Lema, every 15 min for RONSARD and at varying intervals for S-Pol. The Monte Lema and RONSARD radars scanned a full 360° cylindrical volume centered on the radar. S-Pol performed sector scans in the region of heaviest orographic precipitation, generally scanning sectors northwest-north of the radar, with azimuthal (PPI) scans alternating with elevation (RHI) scans. The PPI volumes have been bilinearly interpolated to a Cartesian grid with a resolution of 2 km x 2 km in the horizontal and 0.5 km in the vertical using NCAR's SPRINT software (Mohr and Vaughan 1979). The interpolation allows the data to be displayed in Mountain Zebra (James et al. 2000), which is a version of the NCAR display software Zebra (Corbet et al. 1994). In Mountain Zebra the data fields can be visualized, overlaid and interpreted relative to details of the topography. The RHI sectors by S-Pol provided sufficient vertical resolution to estimate microphysical fields from measured polarimetric radar parameters. The particle identification categories at each pixel in polar coordinates were assigned to a Cartesian bin to facilitate analysis of the microphysical processes in relation to the underlying topography.

Data obtained with the University of Washington Orographic Precipitation Radar (OPRA) is also discussed. OPRA is a vertically pointing Doppler radar that was deployed at Locarno-Monti (Fig. 2.1). Its main characteristics are listed in Table 2.1.

Table 2.1: MAP Radars Characteristics

Radar	MONTE LEMA	RONSARD	S–POL	OPRA
Wavelength(cm)	5.6	5.4	10	10
Peak Power (kW)	251	250	1000	60*, 35$^{\diamond}$
Beamwidth (°)	1.0	0.89	0.91	4.3
Unambiguous velocity interval (m s^{-1})	8.27-16.54*	9.8 or 19.6†	22.4	25

* Maximum

$^{\diamond}$ Minimum

* Changes with increasing elevation angle

† Depending on the chosen Pulse Repetition Frequency

2.1.1 Quality control of the radar data

Over a region with a topography like the one around the MAP radar network (Fig. 2.1), an effective ground clutter elimination procedure had to be applied to the radar data to obtain reliable reflectivity information. The Monte Lema radar went through a decision tree algorithm to determine whether each individual gate was precipitation or clutter. Firstly, if the radial velocity of the signal was outside a band around zero velocity the gate was classified as precipitation. If the radial velocity value was inside this range a statistical clutter-filter algorithm was applied. A signal probability distribution was used to determine the probability that the signal was precipitation. Finally, a gradient test was applied by checking the change in signal power from one elevation angle to the next. If the gradient was higher than a threshold, it was classified as a false signal, and the pixel was marked as clutter. As a last measure, for signals with zero velocity and statistics which could be precipitation, an adaptive clutter map was consulted. If the clutter map indicated that the gate in question had shown significant clutter in the recent past then the measurement was marked

as clutter, otherwise the measurement was accepted as precipitation. This technique successfully eliminated most of the ground clutter, however they were localized exceptions, as will be discussed later (Sec. 5.2).

The S-Pol data was subjected to a radial velocity test. If the radial velocity value of an individual pixel was inside a band around zero velocity and the spectrum width was narrow, the pixel was classified as ground clutter. The reflectivity data from RONSARD was strongly affected by ground clutter, therefore for this radar only radial velocity data is shown.

2.2 Satellite, raingauge and sounding data

Hourly infrared and water vapor satellite imagery were used to determine the extent and evolution of synoptic features and deep convective systems during major rain events over central Europe.

To determine the larger-scale context of the precipitation detected by the three radars in the Lago Maggiore region, this study uses rain gauge data from northern Italy and southern Switzerland to produce larger-scale maps of the rain accumulations in each IOP examined. The gauges were sparsely distributed and subject to local and other sampling problems. Nevertheless, they provide a general idea of the overall rain pattern in each storm.

To determine the characteristics of the flow upstream of the radar-observed precipitation, this study uses data from the sounding at Milano-Linate (Fig. 2.1). During the 1998 and 1999 autumn season four times per day soundings were obtained (0000, 0600, 1200, 1800 UTC).

2.3 Model output

During MAP, the atmospheric Mesoscale Compressible Community numerical forecast model (MC2, Benoit et al. 1997) was run in real time to aid scientists in scheduling aircraft missions, radar operations and other special measurement activities. Also, the evaluation of the behavior of such a high resolution model running over an area of complex terrain was an important objective of the experiment. The MC2 is a nonhydrostatic model and during MAP it was run with a horizontal resolution of 3 km and with 50 vertical levels. Mixing ratios of cloud water, rain water, ice crystals and graupel (Benoit et al. 1997, 2002; Kong and Yau 1997) were forecast along with all the standard meteorological variables. Hourly output are available from http://www.cmc.ec.gc.ca/rpn/modcom/index2.html. A detailed evaluation of the performance of the MC2 has begun and it is still underway (Benoit et al. 2002).

This study uses model output in three ways: (1) to determine the general synoptic context of each IOP; (2) to derive storm averaged fields of model variables to compare with storm averaged radar-derived fields of wind and microphysical quantities; (3) to calculate trajectories of air flowing into the region of radar observations.

To compare model airflow with radar observations, the wind components of the model simulations were used to construct model radial velocity fields that would have been seen by Monte Lema, RONSARD and S-Pol. The radial velocity V_R is given by:

$$V_R = (u\,sin\alpha_a + v\,cos\alpha_a)cos\alpha_e + (w - V_T)sin\alpha_e \tag{2.1}$$

where u, v, and w are the zonal, meridional and vertical components of the wind, α_a is the azimuth angle (measured clockwise from the north) toward which the radar beam is pointing, α_e is the elevation angle, and V_T is the fall speed of the particles (Houze 1993). Since there was no information about the latter, it was assumed to be

zero. This assumption is not critical to the calculation of horizontal wind components

To construct backward isobaric trajectories, the following procedure was used. Let:

$$\frac{d\mathbf{X}}{dt} = \mathbf{v}(\mathbf{X}(t)) \tag{2.2}$$

with t being time, $\mathbf{X}$ the position vector, and $\mathbf{v}$ the wind vector. The iterative scheme (Petterssen 1940) was then used:

$$\mathbf{X}_1 = \mathbf{X}_0 - \Delta t\ \mathbf{v}(\mathbf{X}_0, t) \tag{2.3}$$

$$\mathbf{X}_n = \mathbf{X}_0 - \frac{\Delta t}{2}[\mathbf{v}(\mathbf{X}_0, t) + \mathbf{v}(\mathbf{X}_{n-1}, t + \Delta t)] \tag{2.4}$$

where Δt is the integration time step (which in this study was 1 hour), $\mathbf{X}_0$ is the inital position vector and $\mathbf{X}_1$ and $\mathbf{X}_n$ are the position vectors at iterations 1 and n, respectively.

In addition, output from the European Centre for Medium-Range Weather Forecasts (ECMWF) model is presented to illustrate the larger-synoptic characteristics prevailing during heavy rain events.

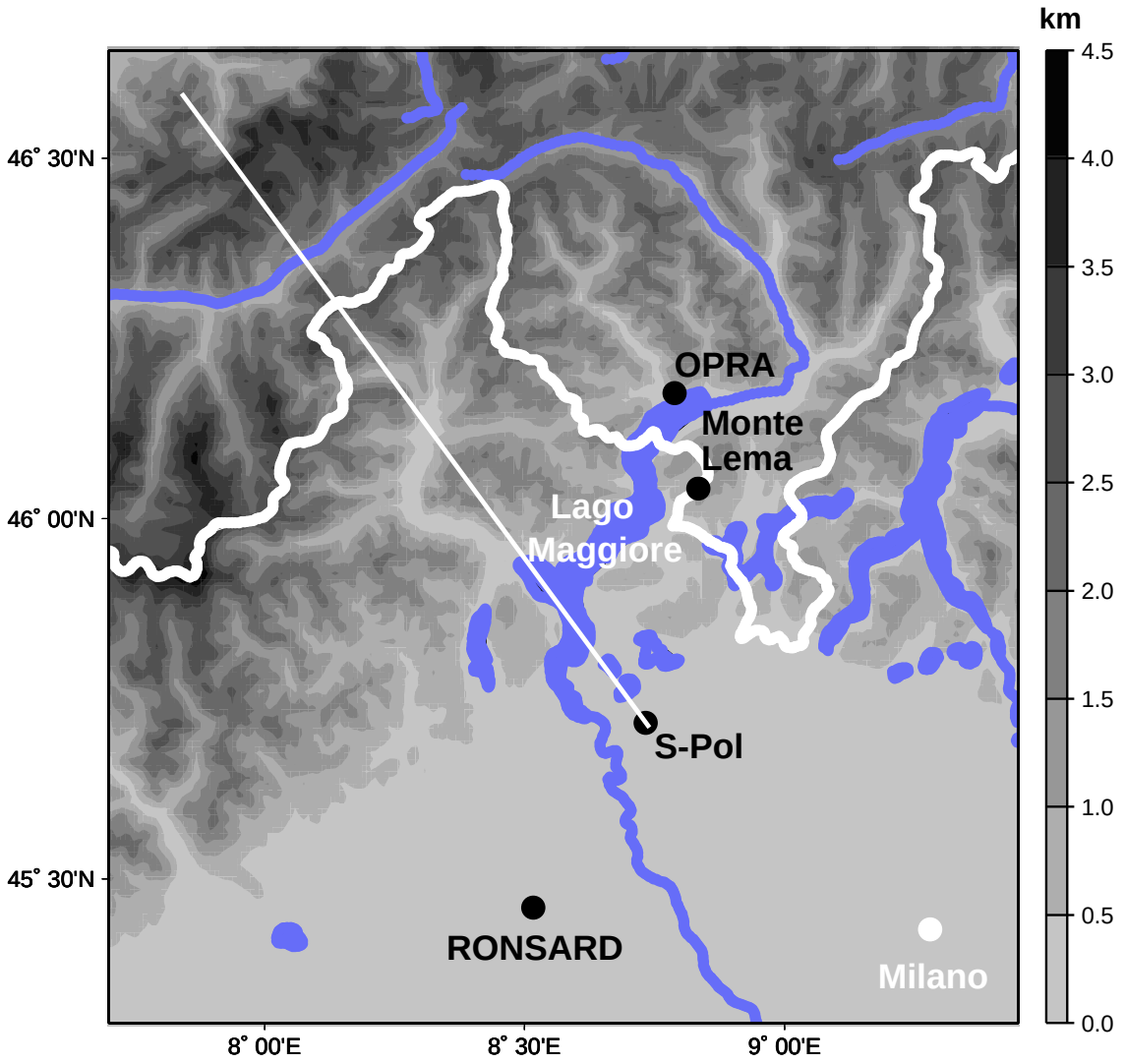

Figure 2.1: Topography around the Lago Maggiore region with bodies of water (in blue), radar locations (black dots), and sounding location (white dot). The white line shows the location of the cross section shown in Figs. 5.6, 5.8, 5.9, and 5.10.

Chapter 3

AUTUMN SEASON PRECIPITATION AND AIRFLOW CLIMATOLOGY OVER LAGO MAGGIORE AREA

Orographic precipitation mechanisms involve a combination of dynamical processes related to fluid flow over topography and microphysical processes of precipitation growth. These processes operate on a wide range of time and space scales. Individual peaks and valleys of the terrain modulate the precipitation forming processes. Release of atmospheric instability occurs on small spatial and time scale, while atmospheric stability promotes more widespread and persistent patterns. Since the topography remains constant, we expect certain aspects of the orographic precipitation processes and patterns to be repeatable from case to case. Accordingly we would expect the processes to have rather similar behavior from storm to storm and from year to year. To test this expectation, Houze et al. (2001) examined the average patterns of radar data collected in all the storms in the Lago Maggiore region in the fall seasons of both 1998 and 1999. The results summarized in this chapter provided the analysis of the 1999 season (the MAP field season) for Houze et at. (2001) study and contributed to the synthesis of the data from the two seasons.

3.1 Airflow and thermodynamic sounding climatology

The Milano-Linate sounding data for both 1998 and 1999 autumn seasons were used to create an upper air climatology of the thermodynamics and airflow that prevailed upstream of the Alps during the rain events of this season. The dew point depression

is used as a proxy of rain over the Lago Maggiore region. From inspection of the 1999 MAP season data, it is clear that whenever there was an IOP declared, the averaged dew point depression of the 925-700 hPa layer was $< 6°C$, therefore this value was adopted for both seasons as an indicator of precipitation occurring over the Lago Maggiore area. According to the Milano sounding, the mean autumn atmosphere during rain events had a temperature profile characterized by a moist adiabat from the surface to 700 hPa (except in a 925-850 hPa layer, where the atmosphere was conditionally unstable), which implies neutral stability for a saturated atmosphere and a stable situation for an unsaturated case (Fig. 3.1). The atmosphere was absolutely stable from 700 to 400 hPa. The surface temperature and mixing ratio were $\sim$15°C and $\sim$8.5 g kg^{-1}, respectively. The 1000 hPa wind data were available for selected soundings only, which provided a biased mean so they are not plotted. At 925 hPa the winds were weak and from the southeast. They veered with height to become weak southerlies around 850 hPa. Southwesterlies prevailed at 700 hPa and at higher levels the winds kept slightly veering, and increasing in magnitude.

3.2 Calculation of seasonal mean patterns of MAP radar data

Seasonal mean fields of reflectivity, rainfall rate and radial velocity were constructed for all precipitation events occurring during autumn 1999. To obtain the seasonal means, hourly values of the radar-derived variables were averaged. The mean radar fields for 1998 were available only for the Monte Lema radar.

The rainfall rate was estimated from the radar data by using the Marshall-Palmer (1948) Z-R relation:

$$Z = 200R^{1.6} \tag{3.1}$$

Table 3.1: Number of radar volumes included in seasonal mean patterns

	MONTE LEMA	S–POL	RONSARD
Autumn 1998	554	—	—
Autumn 1999	598	320	213

where Z is the equivalent reflectivity in $\mathrm{mm}^6\ \mathrm{m}^{-3}$ and R is the rainfall rate in mm h^{-1}. The rain rate and radial velocity calculations treated missing echoes differently. Missing reflectivity is interpreted to mean that no precipitation was occurring. The same assumption could not be made with missing radial velocity gates. Therefore, the mean rainrate $\overline{R}$ and radial velocity $\overline{v}$ were computed as:

$$\overline{R} = \frac{\sum_{i=1}^{N} R_i}{N} \tag{3.2}$$

$$\overline{v} = \frac{\sum_{j=1}^{n} R_j}{n} \tag{3.3}$$

where N is the total number of volumes, and $n(\leq N)$ is the number of volumes with non-missing radial velocity values at the grid point in question. From Eq. 3.2, it is evident that maxima in the spatial field of mean rainrate indicated regions where the precipitation was either more frequent, more intense or both. To remove some of this ambiguity, a third field called the precipitation frequency was calculated and defined as the percentage of the total volumes in which reflectivity $\geq 13\,dBZ$ ($\sim$ 0.16 mm h^{-1}) was observed at each grid point. The number of volumes used in each season and for each radar is shown in Table 3.1. These procedures for processing the radar data were initially developed for the Houze et al. (2001) study by Curtis James.

3.3 Mean radar reflectivity pattern

The lowest altitude at which the Monte Lema radar can measure reflectivity over a broad area is about 2.0 km MSL (Fig. 3.2). The climatological precipitation rate implied by the Monte Lema radar data for the 2.0 km MSL level for the periods of September to November 1998 and 1999 according to Eqs. 3.1–3.2 is shown in Fig. 3.3a and b. The fields are generally consistent with the rain-gauge based climatology of Frei and Schär (1998) (Fig. 1.3) but provide local detail plus three dimensionality. The rainfall fields for both years have a maximum over the lower slopes ∼20 km northwest of the radar. The spot of abnormally high reflectivity ∼19 km northwest of the radar during the 1999 autumn season was produced by anomalous propagation due to the strong stability of the atmosphere during one of the events (IOP8). The major differences between the two years are the broader area of high values to the northwest of the radar in the autumn 1999 climatology and an area of higher reflectivities to the east of the radar in autumn 1998. A vertical cross-section lying in a plane approximately parallel to the 2.0 km flow (red line in Fig. 3.3a) shows the mean reflectivity field for the 1998 season (Fig. 3.3c). This section agrees with Frei and Schär (1998) by showing maximum reflectivity over the windward slopes of the Alpine range, well below the crest of the barrier. The vertical cross-section of precipitation frequency (Fig. 3.3d), defined as the percentage of volumes in which the reflectivity equaled or exceeded 13 dBZ (Sec. 3.2), also showed a maximum on the lower windward slopes, where the average reflectivity was maximum, indicating this was not a transient feature but a robust characteristic throughout the season.

During the MAP 1999 season, the additional radars located over the Po Valley provided data extending down to the floor of the plain. In the same vertical cross section (red line in Fig. 3.3a), the S-Pol reflectivity (Fig. 3.3e) and precipitation frequency (Fig. 3.3f) confirm the structures seen in 1998 (Figs. 3.3c and d). Since the

S-Pol radar's beam was not blocked at low levels as much as the Monte Lema radar, these patterns show the structure of reflectivity below the 2 km level. The height of the maximum reflectivity (slightly above 2 km) is the same in both years. However in the 1999 S-Pol data, the maximum is shifted ∼10 km to the south-southeast, a feature that was also seen in the 1999 Monte Lema data (not shown). The precipitation frequency (Fig. 3.3f) as seen from S-Pol in 1999 was also consistent with that seen in the 1998 Monte Lema observations, and also shifted to the south-southeast.

The vertical cross sections of reflectivity (Fig. 3.3c and e) indicate that the maximum reflectivity consistently occurred at low altitudes, below ∼ 4 km MSL. This result differs from the pattern observed over lower hills (Bergeron 1965, Hill et al. 1981), where the precipitation increases with height to reach its maximum at the top of the terrain. Over a high mountain range, the typical decrease in saturation mixing ratio with altitude leads to a precipitation maximum on the upslope side. Since 4 km is approximately the altitude of the highest Alpine terrain downstream of the radar, the persistent maximum of the echo intensity below this level indicates that the precipitation particles form, grow, and fallout quickly and efficiently over the lower slopes of the Alpine barrier.

3.4 Mean radial velocity pattern

The 2.0 km mean radial velocity field for both 1998 and 1999 autumn seasons is shown in Fig. 3.4a and b. The wind direction was perpendicular to the zero line, directed from green to yellow in the figure. The mean radial velocity field for the 1998 season (Fig. 3.4a) indicates that the prevailing wind direction at 2.0 km MSL at Monte Lema was south-southeasterly, and its magnitude was 4-6 m s^{-1}. The 1999 season mean radial velocity (Fig. 3.4b) was slightly more intense (6-8 m s^{-1}) and had a somewhat stronger easterly component but overall was quite similar to 1998. The mean radial

velocity observed by the RONSARD radar during autumn 1999 at an altitude of 2.0 km (Fig. 3.4c) was similar to that of Monte Lema at the same level. Because it was situated at lower levels, the RONSARD radar was able to detect the wind below the 2.0 km MSL level. The wind direction shifted to east-southeasterly at 1.0 km (Fig. 3.4d) and became easterly at the lowest available level (0.5 km, Fig. 3.4e). The 0.5, 1.0 and 2.0 km RONSARD radial velocity data, as well as higher-level Monte Lema and RONSARD radial velocity data consistently show that the wind veered with height during precipitation events in the Lago Maggiore region, becoming southwesterly at 5.0 km MSL (not shown).

3.5 Wind direction and Froude number epoch analysis

Since the autumn 1998 and 1999 climatologies generally agree, they have been combined to calculate epoch patterns according to 1) wind direction and 2) Froude number. The different epochs are defined by the upstream flow. The flow into the region of precipitation observed by radar was sampled every six hours by radiosonde measurements at the Milano-Linate Airport (Fig. 2.1). The wind direction, wind speed, stability, and Froude number that characterized the environment immediately upstream of the radar-observed area was calculated from these soundings. The values of these variables delineated data subsets used in superposed epoch analysis. Each variable was represented by its average value within the 925-700 hPa layer (corresponding roughly in altitude to 0.75-3.0 km MSL) in the sounding. If no sounding was available within 3 h of the beginning of a radar volume scan, the volume was not used for those superposed epoch analyses that required sounding information. Sounding information was available for 480 of the 554 radar volumes for the 1998 MAP season, for 549 of the 598 Monte Lema volumes and for 190 of the 213 RONSARD radar volumes for the 1999 season. To indicate statistical significance this study follows a procedure devised by Curtis James in which a Student's difference-of-means test was

carried out at each grid point. An a priori confidence level of 95% rejected the null hypothesis that the mean rainfall rate at a given grid point did not differ significantly from the seasonal mean. Two-sided difference of means tests uses the expression:

$$t = \frac{\overline{x_1} - \overline{x_2}}{\sqrt{\left(\frac{1}{N_1} + \frac{1}{N_2}\right)\left(\frac{N_1 {s_1}^2 + N_2 {s_2}^2}{N_1 + N_2 - 2}\right)}} \tag{3.4}$$

where $\overline{x_1}$, s_1 and N_1 are the mean, standard deviation and number of volumes in the sample, and $\overline{x_2}$, s_2 and N_2 are the seasonal mean, standard deviation and total number of volumes in the archive. The null hypothesis was rejected in regions where $\mid t \mid > 1.96$, corresponding to a 95% confidence level.

3.5.1 Rain distribution as a function of direction of impinging flow

As was mention in the Introduction, the terrain curves inward over the Lago Maggiore region. Figure 3.5 indicates the influence of the concave shape of the topography on the precipitation in relation to the upstream wind direction. The individual panels of this figure present data for autumn 1998 and 1999 according to the average wind direction in the 925-700 hPa layer, as computed from the Milano soundings. For each wind-direction category (east, southeast, south, and southwest), the panels on the left show the distribution of radar-derived rain rate while the panels on the right show the t-statistic of the rain pattern. Each panel also shows the 800-m MSL terrain-height contour. This contour indicates both the fine-scale pattern of ridges and valleys in the lower portion of the Alps and the broader outline of the mesoscale concave indentation of the Alps surrounding the Lago Maggiore region. The contour lies generally east, north, and west of the Monte Lema radar, with the lowland region of the Po Valley lying to the south. Thus, winds over this region from the east, southeast, south, and southwest each encounter rising terrain. Figure 3.5a shows the rain rate field at 2 km for the easterly flow cases (wind direction between 67.5° and 112.5°), which favor upslope enhancement of precipitation over the western slopes of the mountains surrounding the area covered by the radar. The statistical significance of this result is

shown by the field of the t-statistic of the rain rate at the 2-km level (Fig. 3.5b). The red areas, where t>1.96, indicate where the sample mean is significantly above the seasonal mean. Blue areas (t<-1.96) indicate where the sample mean is significantly below the seasonal mean. Over most of the domain, the precipitation rate was not significantly different from the seasonal climatology in the easterly flow case. Rates were significantly above the seasonal mean over some regions to the west, where the flow was upslope, and significantly below over a few slopes on the eastern side of the domain, where the flow was downslope. The composite for southeasterly flow (112.5°-157.7°, Fig. 3.5c) shows intense precipitation over most of the domain with a statistically significant precipitation increase over the western slopes and over the Po Valley (Fig. 3.5d). The cases with southerly flow (157.5°-202.5°, Fig. 3.5e and f) had intense, significantly increased precipitation over all the lower slopes of the Lago Maggiore region. Comparison of panels c and e in Fig. 3.5 indicates that both southeasterly and southerly flow produced large orographic enhancement of rainfall on the lower slopes of the Alps, with the latter providing the stronger upslope component. In southwesterly flow (202.5°-247.5°), precipitation was below the seasonal mean, especially in the western portion of the radar domain, evidently because of downslope flow (Fig. 3.5g and h).

3.5.2 Rain and flow distribution as a function of Froude number

It is evident that the southeasterly and southerly cases are associated with the most intense orographically enhanced precipitation. Therefore, we will restrict the Froude number analysis to cases within these two epochs. The Froude number was calculated using Eq. 1.1. The terrain height used was H=2.5 km MSL, since this elevation characterizes the elevation of mountain passes along the north side of the Lago Maggiore region. The Brunt-Väisälä frequency was computed using finite differences over the 927-700 hPa layer. We will use the moist Brunt-Väisälä frequency given by Eq. 1.3

(Durran and Klemp 1982). This choice is consistent with the fact that we are considering only cases of precipitation seen by radar. We assume that even if the upstream flow over Milano was less than saturated the air was saturated by the time it was producing rainfall over the Alps. Experiments assuming dry or moist Brunt-Väisälä frequency based on a humidity threshold led to erratic results.

Figure 3.6 shows the fields of rain rate and t-statistics at the 2-km level for the Froude number composite analyses. These patterns contain all radar data obtained when the flow into the Lago Maggiore region, as measured by the Milano sounding, was southeasterly or southerly and not blocked ($F>1$, Fig. 3.6a and b) and blocked ($F<1$, Fig. 3.6c and d). The t-statistic calculations show that when the Froude number was high, the precipitation rates over the foothills, lower slopes and western Po Valley were significantly stronger. When the Froude number was low, the precipitation rates were very close to climatology, with a suggestion of blocking far upstream, near the southeast corner of the radar domain at a range of about 80 km from the radar.

The Monte Lema radial velocity at the lowest level available (2 km MSL) had a similar direction for both Froude number epochs, however the high Froude number cases had a stronger southerly component (Fig. 3.7a) than the low Froude number cases, which were dominated by southeasterly flow (Fig. 3.7b). This directional difference would be consistent with the impinging flow at lower Froude number turning cyclonically as it approached the barrier, as would be expected in a blocking scenario. However, it is only a slight directional difference. Also, the strength of the flow is comparable for the two cases. The effect of blocking was apparently felt more strongly at levels below 2 km. The RONSARD radar was able to observe the radial velocity at lower altitudes than Monte Lema because of its location in the lowlands of the Po Valley. The 1999 data from RONSARD show that the flow turned sharply cy-

clonically from east-southeast at high Froude number (Fig. 3.7c) to northeasterly at low Froude number (Fig. 3.7d). Again, this behavior is consistent with the blocking implied by the precipitation patterns in Fig. 3.6.

The sounding data was also composited according with the same parameters. Southeasterly and southerly cases with dew point depression $< 6°C$ were separated by Froude number. Fig. 3.8 shows the mean sounding when $F > 1$. From the surface to 925 hPa, the atmosphere was moist neutral. The layer from 925 to 700 hPa was conditionally unstable and above that the atmosphere was absolutely stable. The surface temperature and mixing ratio were 18°C and 10 g/kg, respectively, with both values larger that those of the climatology (Fig. 3.1). The wind structure was very similar to the climatology, except at the 850 hPa level where the high Froude number cases show south-southeasterlies as opposed to weak southerlies (Fig. 3.1). Even though the altitudes are not exactly the same, the wind vector at 850 hPa was consistent with the radial velocity depicted by the Monte Lema radar at 2 km (Fig. 3.7a). The 925 hPa wind vector was also consistent with the radial velocity given by the RONSARD radar at 0.5 km (Fig. 3.7c). Fig. 3.9 shows the mean sounding when $F < 1$. Both the temperature and the wind structure above 700 hPa were very similar for both high and low Froude number soundings. However, below this level the differences were very significant: the atmosphere was considerably cooler and it had less moisture for the $F<1$ composite sounding. The vertical profile of the stability also differed: from the surface to 925 hPa the $F<1$ composite sounding was conditionally unstable and absolutely stable from then on. The wind vectors at 850 and 925 hPa are consistent with the radial velocity observations at 2.0 and 0.5 km (Fig. 3.7b and d), although at low levels in the sounding there was no evidence of a northerly component to the flow.

SUMMARY:

Seasonal climatology of Doppler radar data for the autumn seasons of 1998 and 1999 document detailed three-dimensional characteristics of the precipitation structure and accompanying airflow. Radar reflectivity and Doppler radial velocity patterns observed in the two seasons are in close agreement with each other, suggesting that the MAP season was generally representative of autumn rainfall on the Mediterranean side of the Alps. The radar reflectivity was strongest over the lower windward slopes and decreased toward higher terrain. Vertical cross-sections of mean reflectivity patterns for both years show that precipitation generally developed at low altitudes, with most of the precipitation growth occurring at altitudes below the Alpine crest. During rain events, the mean radial velocity at the 0.5 km level was easterly, veered with height and became south-southeasterly at the 2 km level, with magnitudes between 4-8 m s^{-1}.

Superposed epoch analyses of the Doppler radar data collected in the Lago Maggiore region during autumn 1998 and 1999 indicate that there is a clear relationship between the upstream flow direction and the intensity of precipitation over the Lago Maggiore region. These analyses show the role of the perpendicularity between the local topography and the airstream. Over the Lago Maggiore region the precipitation was significantly greater when the wind direction around the 2 km level was southerly or southeasterly. The rainfall over the lower slopes rapidly dropped off when the flow became either easterly or southwesterly. However it should be pointed out that the easterly flow was characterized by a colder and less moist atmosphere than the other directions, which obviously also contributed to the decreased precipitation. When the southerly and southeasterly flow had a high Froude number, the flow proceeded directly up and over the terrain, and the precipitation was greatly enhanced over the lower windward slopes and over the portions of the Po Valley just upstream of the mountains. With low Froude number southerly and southeasterly flows were strongly blocked below the 2 km level. However at higher altitudes the airstream rose over the

terrain fairly easily. Thus, when the Froude number was small the enhancement of precipitation directly over the lower mountain slopes did not have the participation of the air in the lowest 2 km, which turned eastward in response to blocking. Apparently the lifting of the low-level air was shifted upstream, as precipitation enhancement was suggested upstream of the barrier crest in the blocked cases. The soundings corresponding to the Froude number epoch analysis exhibited flow structure consistent with the observed radar radial velocity patterns. They also documented a colder and more stable atmosphere during blocked ($F < 1$) cases. The blocked and unblocked regimes will be examined in detail in the next chapters by focusing our attention on case studies that represented each type of regime.

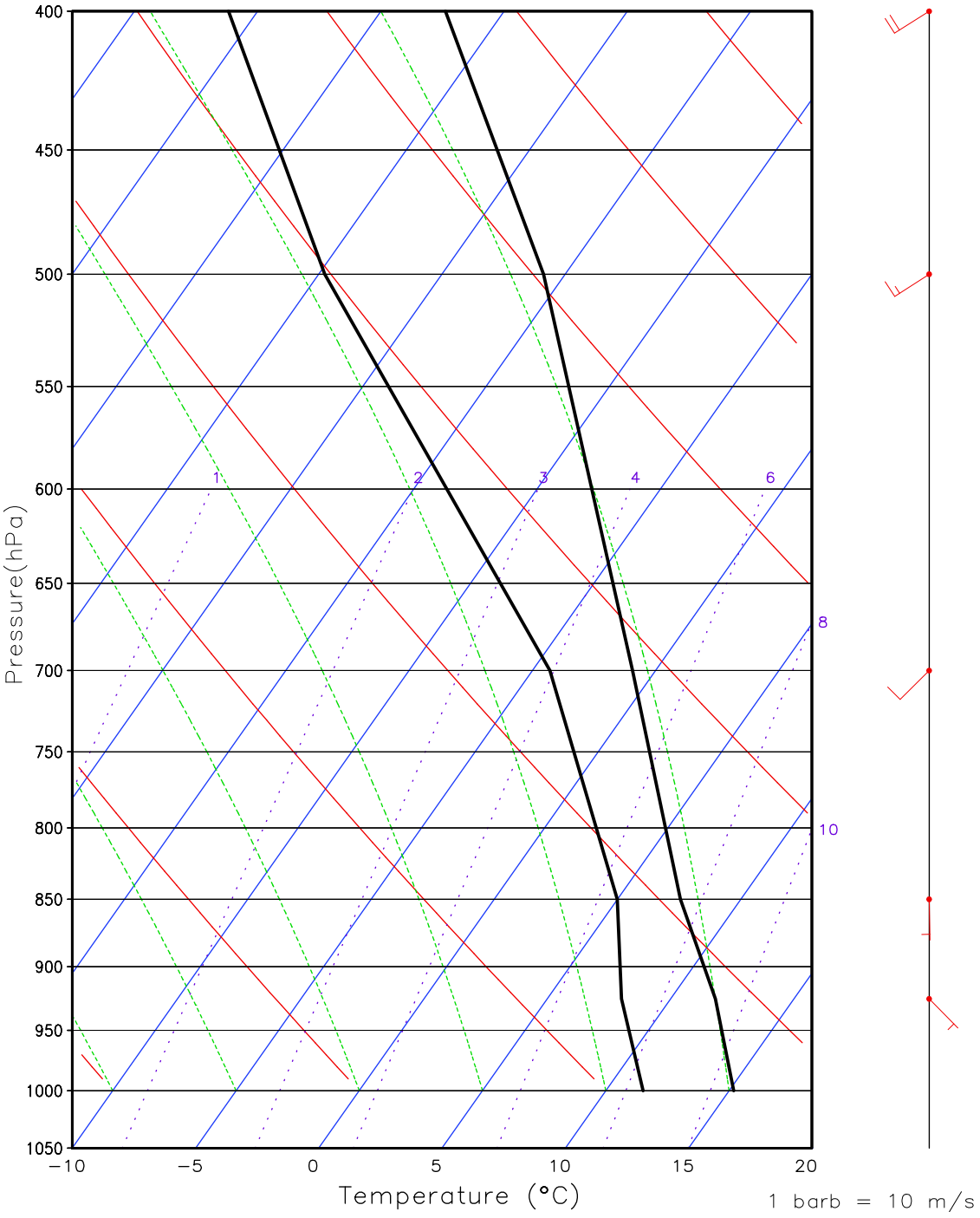

Figure 3.1: Skew-T log p diagram of the mean autumn Milano sounding during rain events during 1998 and 1999.

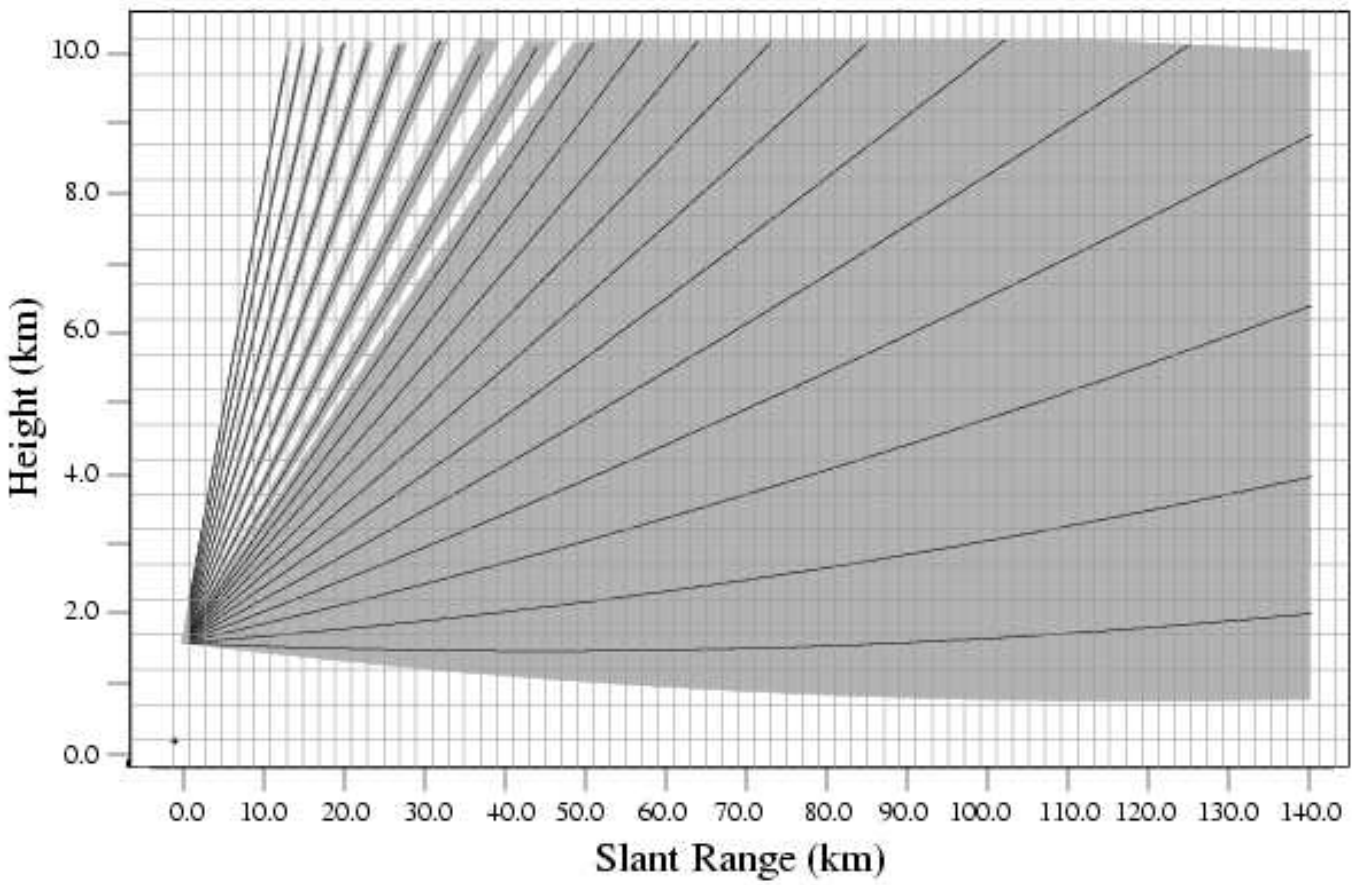

Figure 3.2: Vertical cross-section plot of the Cartesian interpolation grid. The grid points are located midway between the intersection of the horizontal and vertical lines. The Monte Lema radar is located at 0 km range and 1.63 km MSL. The cross-sectional area covered by each radar volume under standard atmospheric conditions is shaded. The shaded area is determined by the beamwidth of each tilt elevation angle (elevation angles= -0.3, 0.5, 1.5, 2.5, 3.5, 4.5, 5.5, 6.5, 7.5, 8.5, 9.5, 11.0, 13.0, 15.5, 18.3, 21.6, 25.3, 29.6, 34.5 and 40.0°).

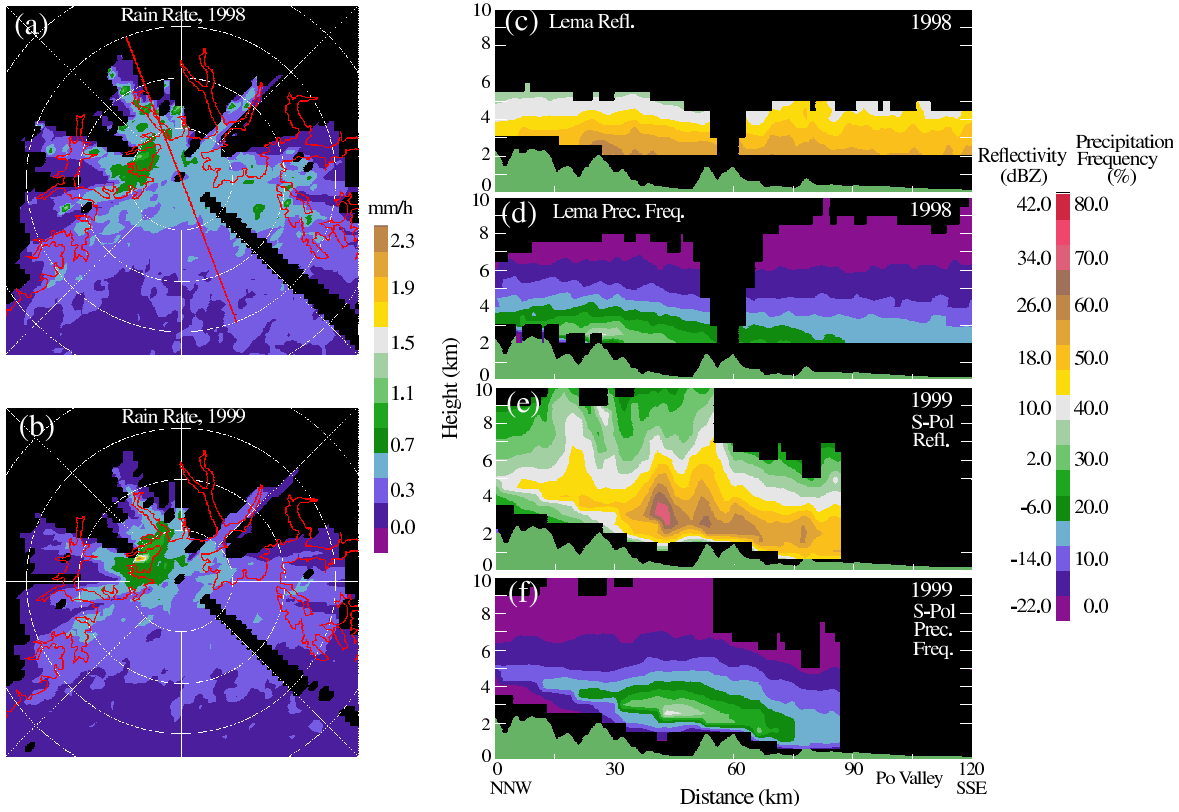

Figure 3.3: Constant altitude plots at 2 km MSL containing the mean radar-derived rainfall rate observed by the Monte Lema radar during all precipitation events during (a) 1998 and (b) 1999 MAP seasons. Range-ring spacing is 20 km. Vertical cross-section along the red line in (a) depicts (c) radar-derived reflectivity and (d) precipitation frequency during the 1998 MAP season as observed by the Monte Lema radar. Vertical cross-section along the red line in (a) depicts (e) radar-derived reflectivity and (f) precipitation frequency during the 1999 MAP season as observed by the S-Pol radar. The red contour in (a)-(b) indicates the 800 m MSL terrain contour. The green shading in (c)-(f) represents the terrain profile (after Houze et al. 2001).

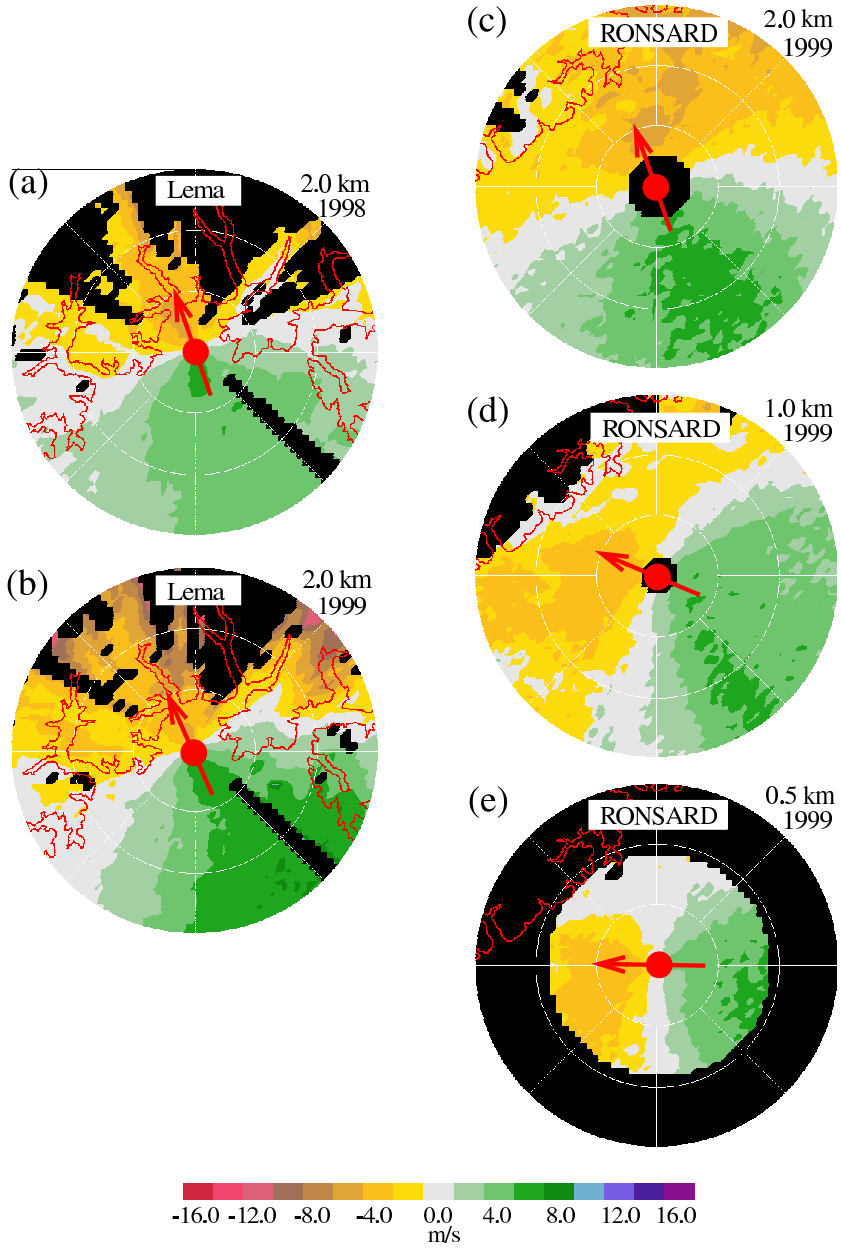

Figure 3.4: Constant altitude plots containing the mean radial velocity during all precipitation events observed during two MAP seasons by Monte Lema radar at 2 km MSL for (a) 1998 and (b) 1999 MAP seasons. Constant altitude plots containing the mean radial velocity observed by the RONSARD radar during all precipitation events during the 1999 MAP season at (c) 2 km MSL, (d) 1 km MSL and (e) 0.5 km MSL. The red contour indicates the 800 m MSL terrain contour (after Houze et al. 2001).

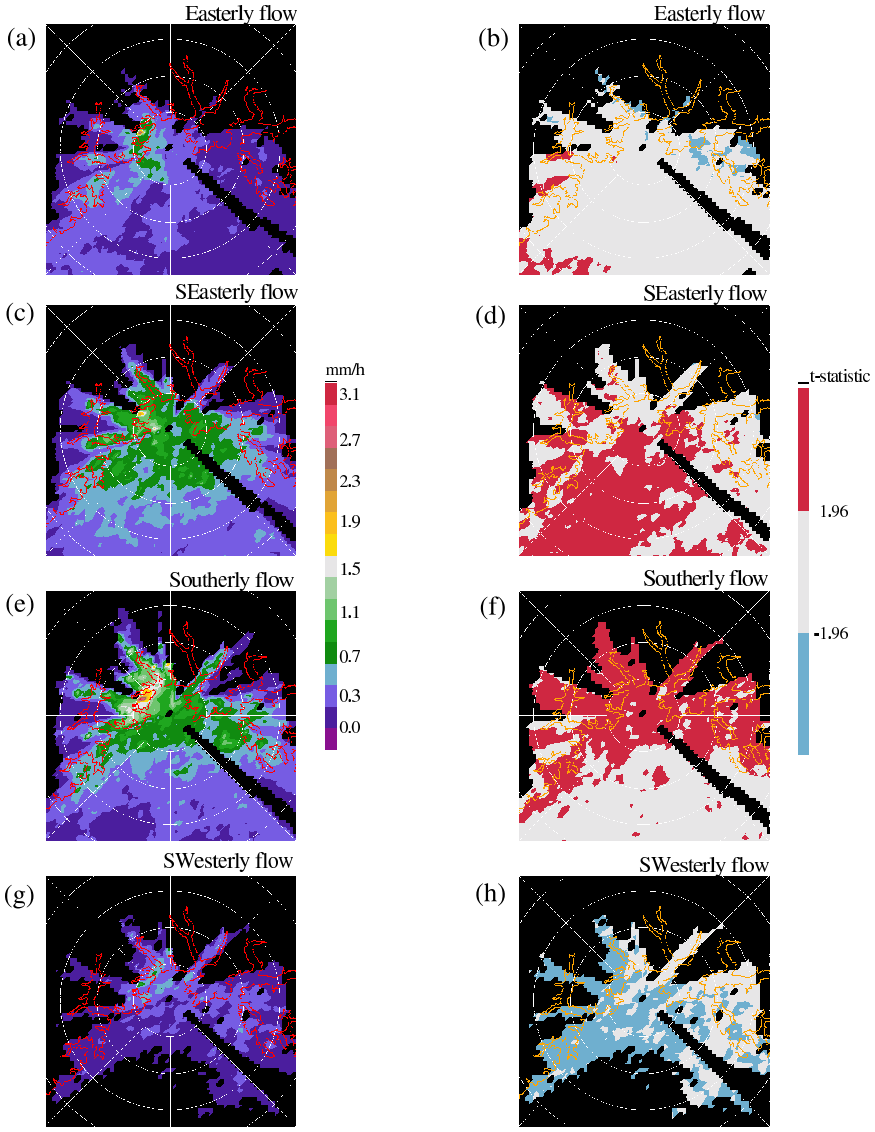

Figure 3.5: Constant altitude plots of mean rainfall rates and t-statistic of rain rate (first and second column, respectively) at 2 km MSL for all precipitation events in which the layer-averaged 925-700 hPa wind in the Milano-Linate sounding indicated flow from (a) and (b) 67.5–112.5°; (c) and (d) 112.5–157.5°; (e) and (f) 157.5–202.5°; (g) and (h) 202.5–247.5° during the 1998 and 1999 MAP seasons, along with the 800 m MSL terrain contour. The range ring spacing is 20 km. Red (blue) contours indicate regions where the t-statistic is greater than 1.96 (less than -1.96) and the null hypothesis can be rejected with a 95% confidence level (after Houze et al. 2001).

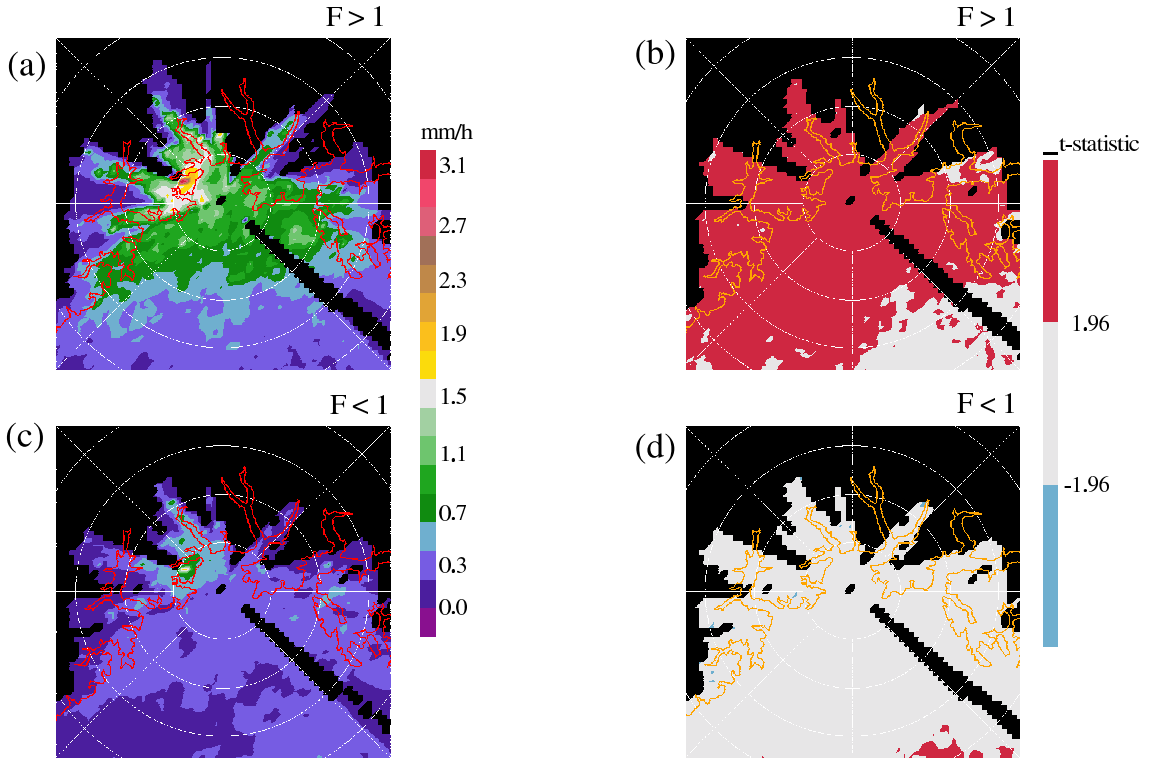

Figure 3.6: Mean 2 km fields observed by the Monte Lema radar when the layer-averaged 925-700 hPa wind in the Milano-Linate sounding indicated flow between 112.5–202.5° and the Froude number was > 1 (a) rainfall rate and (b) t-statistic and the Froude number was < 1 (c) rainfall rate and (d) t-statistic during the 1998 and 1999 MAP seasons, along with the 800 m MSL terrain contour. The range ring spacing is 20 km. Red (blue) contours indicate regions where the t-statistic is greater than 1.96 (less than -1.96) and the null hypothesis can be rejected with a 95% confidence level (after Houze et al. 2001).

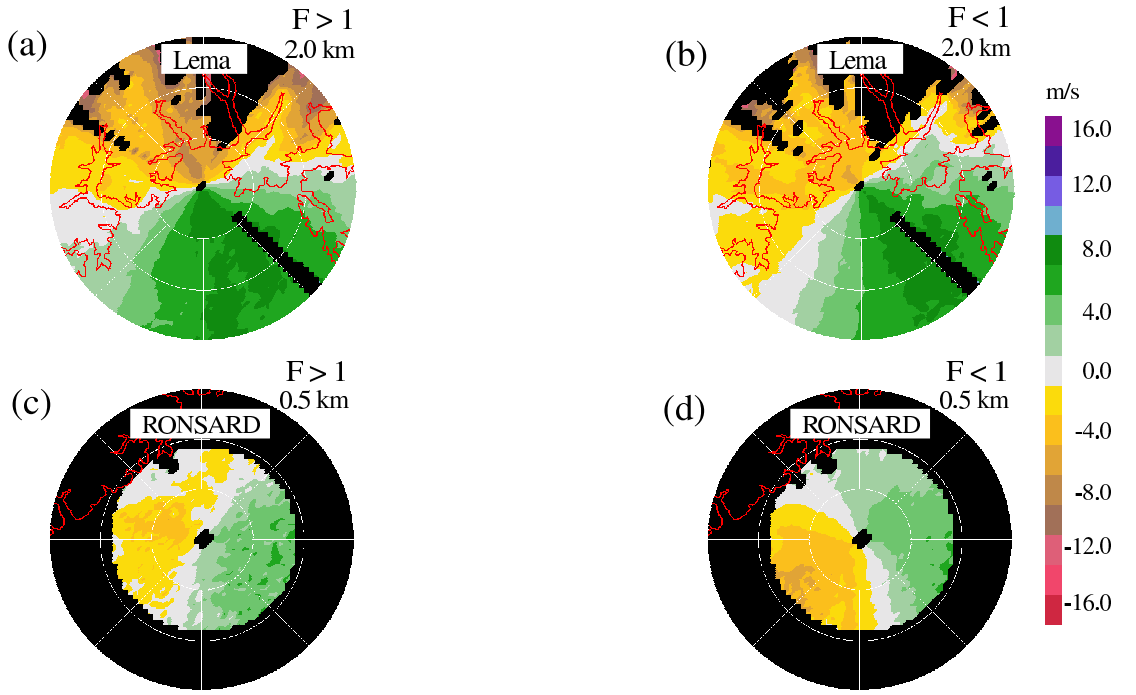

Figure 3.7: Mean radial velocity for all precipitation events in which the layer-averaged 925-700 hPa wind in the Milano-Linate sounding indicated flow between 112.5–202.5° and the Froude number was (a) > 1 as observed by the Monte Lema radar at 2 km MSL and (b) < 1 as observed by the Monte Lema radar at 2 km MSL. Froude number (c) > 1 as observed by the RONSARD radar at 0.5 km MSL, Froude number (d) < 1 as observed by the RONSARD radar at 0.5 km MSL during the 1998 and 1999 MAP seasons, along with the 800 m MSL terrain contour. The range ring spacing is 20 km. Negative (positive) radial velocities denote outbound (inbound) flow (after Houze et al. 2001).

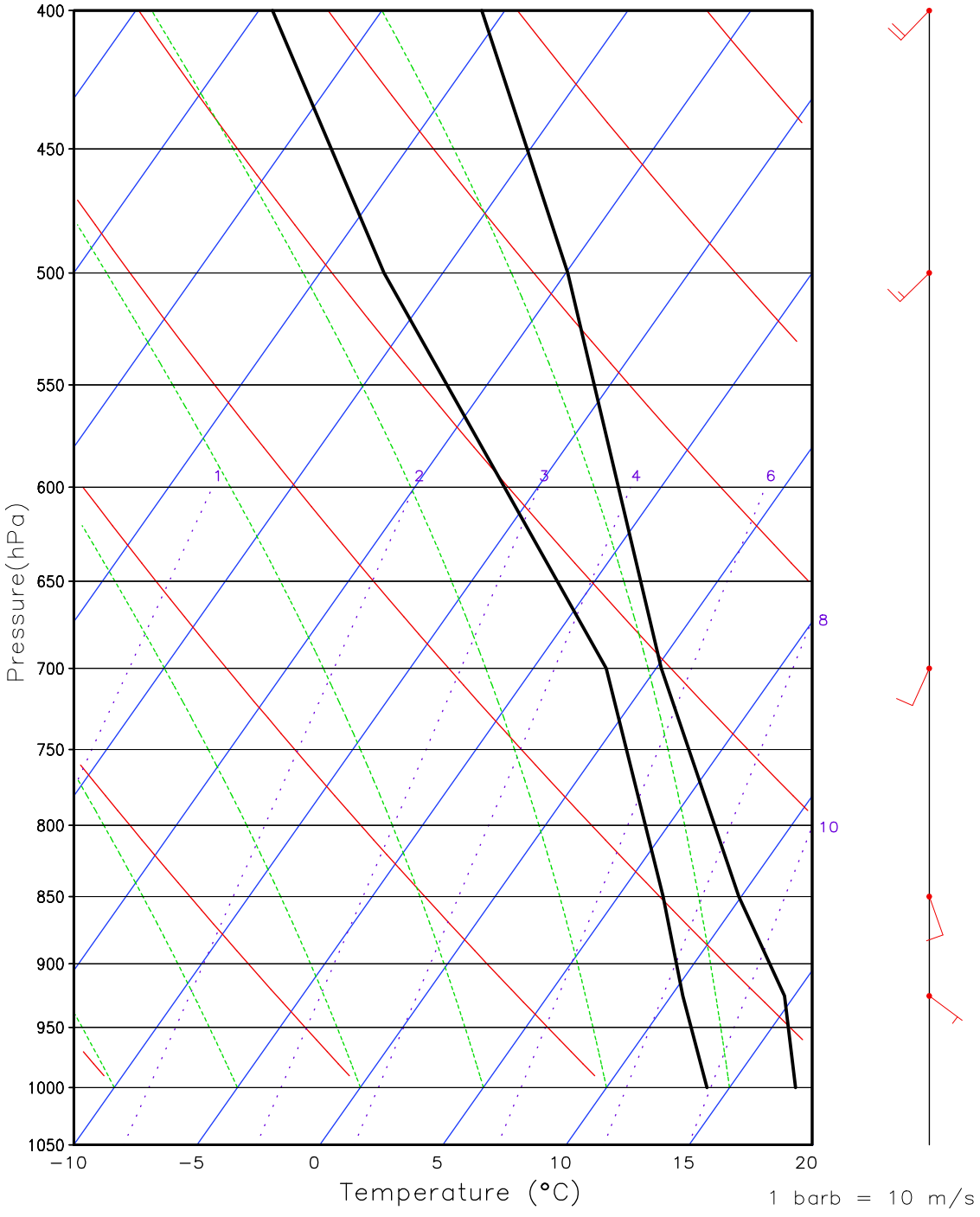

Figure 3.8: Mean Milano-Linate skew-T log p diagram for all precipitation events in which the layer-averaged 925-700 hPa wind indicated flow between 112.5°-202.5° and the Froude number was > 1 during the 1998 and 1999 MAP seasons.

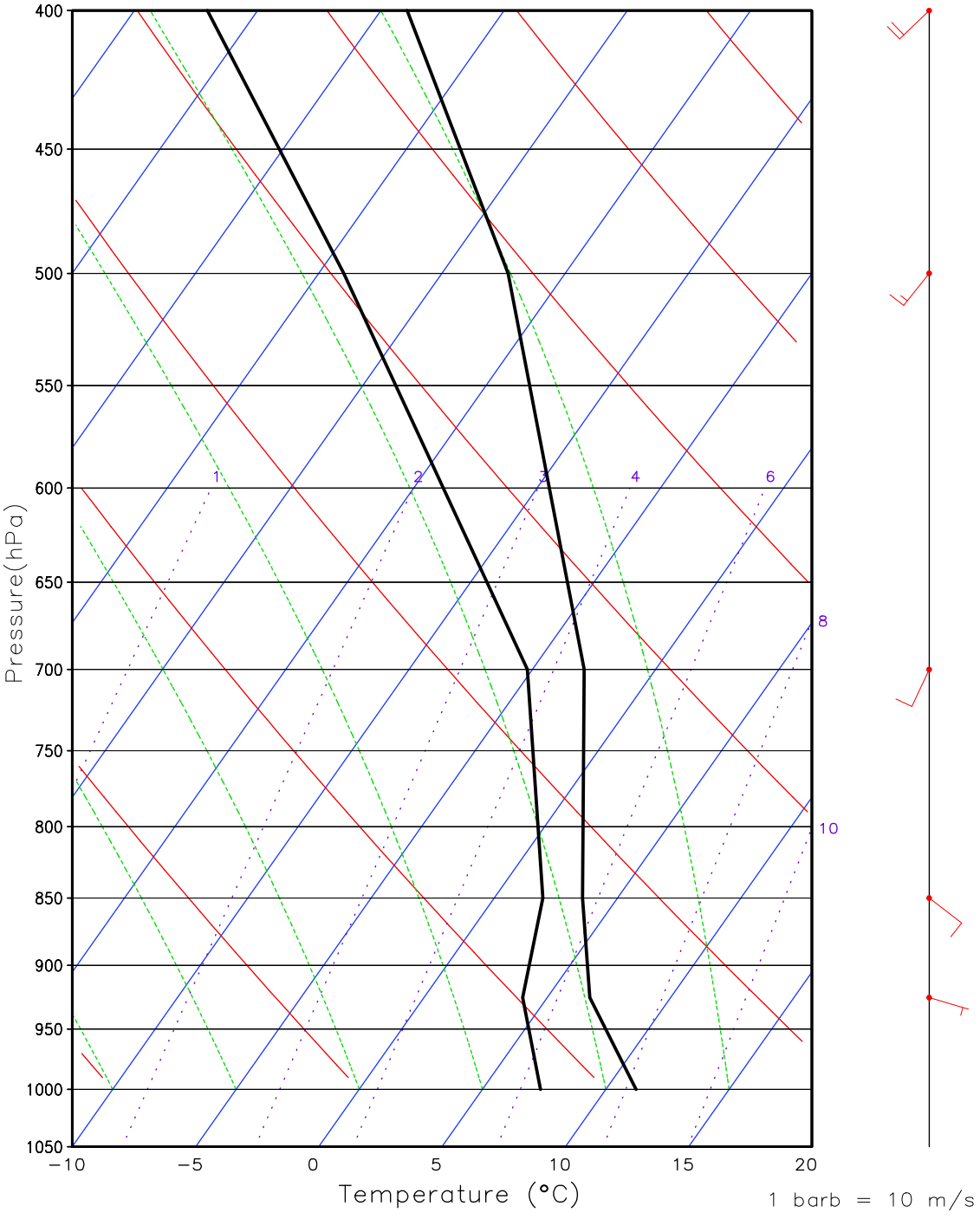

Figure 3.9: Mean Milano-Linate skew-T log p diagram for all precipitation events in which the layer-averaged 925-700 hPa wind indicated flow between 112.5°-202.5° and the Froude number was < 1 during the 1998 and 1999 MAP seasons.

Chapter 4

AIRFLOW AND THERMODYNAMICS IN TWO MAJOR ALPINE RAIN EVENTS

In this chapter, two major MAP rain events representative of the flow regimes studied in Chapter 3 will be compared and documented in detail. IOP2b (1300 UTC 19 September to 0100 UTC 21 September 1999) represented the high Froude number regime identified in the climatology while IOP8 (1200 UTC 20 October to 2200 UTC 21 October 1999) represented the low Froude number regime. It will be shown that while at levels above 850 hPa the events had common characteristics, the low-level flow and thermodynamics differed markedly, resulting in strikingly different precipitation amounts. Model output will also be presented. The model results provide a detailed picture of the broader meteorological setting of the two IOPs of interest. A comparison between the MC2 model output and the observations will be presented to evaluate whether the model accurately represented the orographic precipitation enhancement.

4.1 Upper-level conditions

During 19-21 September 1999 (IOP2b) a 500 hPa trough moved over northern Italy and produced heavy precipitation in several regions. The model forecast of the ECMWF for 1200 UTC 20 September 1999 indicated a deep trough at 500 hPa extending southward into northern Africa, with southerly flow reaching the Lago Maggiore region and crossing the Alps (Fig. 4.1a). As was mentioned in the Introduction, a deep upper-level (500 hPa) trough with southerly (as opposed to southwesterly) moist flow over the Alps has been identified as one of the important aspects of heavy floods

over northern Italy (e.g. Massacand et al. 1998). Therefore, the upper-level flow pattern suggested that this event would produce intense rainfall over the southern flank of the Alps. The MC2 winds during IOP2b exhibited wind directions that were in general constant with time, therefore to investigate the modeled flow on the scale of the whole Alpine barrier, storm means of the MC2 output are presented. The MC2 840 hPa mean wind during IOP2b (Fig. 4.1b) showed south-southwesterly flow over the Ligurian Sea, turning southerly over the Po Valley and south-southeasterly over the Lago Maggiore region.

During 20-21 October 1999 (IOP8), another major trough located over western Europe produced intense precipitation in northern Italy. The ECMWF model forecast a 500 hPa geopotential height field with a low pressure system located over the Mediterranean Sea off the southeast coast of France. At 1200 UTC 21 October 1999 the flow was again southerly towards the Alps over the Lago Maggiore region (Fig. 4.2a). This is the same upper-level pattern described above, which again suggested an intense precipitation event on the southern side of the Alps. As for IOP2b, the MC2 representation of the winds during IOP8 showed wind directions that were very uniform in time throughout the event, therefore storm means are presented. The MC2 840 hPa storm mean wind field depicted southerlies well upstream of the Alps and southeasterlies over Lago Maggiore (Fig 4.2b).

It is evident that the flow patterns at 500 hPa (Figs. 4.1a and 4.2a) and 840 hPa (Figs. 4.1b and 4.2b) were very similar in the region south of the Alps during both events. As it will be shown in the next section, these similarities did not carry over to the lower levels.

4.2 Low-level winds

To investigate the modeled flow at low levels, storm means wind fields for IOP2b and IOP8 are presented. During IOP2b, the MC2 indicated southerly flow at 940 hPa upstream of the Alps (Fig. 4.3a). This southerly flow advected moisture from the Ligurian Sea and turned toward the northwest as it got closer to and went over the mountains in the vicinity of the Lago Maggiore area. Note how that the wind vectors were perpendicular to the northwest slopes of the LM region. According to the MC2 output, a west-east specific humidity gradient, as hypothesized by Rotunno and Ferretti (2001), was not present inside the Po Valley. However, there was some indication of that gradient farther upstream (Fig. 4.3a). The surface (10 m) winds (Fig. 4.3b) indicated that the southeasterly flow over the Adriatic Sea turned to easterly when it entered the Po Valley and converged with a southerly airstream from the Ligurian Sea. This pattern is reminiscent of the surface winds during the Piedmont flood (Buzzi et al. 1995).

Using Penn State/National Center for Atmospheric Research model (MM5) numerical simulations, Rotunno and Ferretti (2002) have found that the easterly flow during IOP8 was deeper than during IOP2b, which is also depicted by the MC2. During IOP8, the MC2 940 hPa winds had a strong easterly component over the Po Valley. This flow decelerated south of the Lago Maggiore region as it turned toward the south to exit the Po Valley through the gap between the Maritime Alps and the Apennines (Fig. 4.4a). The moist southeasterly surface airflow from the Ligurian Sea never reached Lago Maggiore in this case. This figure suggest that the Apennines played a crucial role during this storm by preventing the southerly flow from reaching the Po Valley thus easterly winds were favored over this Valley. It also suggests that the vertical extent of the easterly flow may be related to the height of the Apennines (B. Smull, 2000 personal communication). The specific humidity field suggests that

the moisture over the Po Valley was being advected from the Adriatic Sea by the easterly flow, therefore the specific humidity values were higher at the eastern end of the Po Valley, with a east-west gradient in the opposite direction as in Rotunno and Ferretti's (2001) explanation of the Piedmont flood. Note that the gradient reversed farther upstream. The surface winds (Fig. 4.4b) show essentially the same features as the 940 hPa wind field, except the blocking effect was stronger and air was escaping from the Po Valley through the gap between the Maritime Alps and the Apennines. These characteristics of IOP8 are very similar to the experiment conducted with no latent heating by Buzzi et al. (1998) in the sense that the easterly flow over the Po Valley turned northerly and escaped through the nearest gap. Therefore, the MC2 storm mean patterns show that the low-level flow to the windward side of the LM was blocked during IOP8 (Fig. 4.4b, F<1 regime), whereas it went up and over the terrain during IOP2b (Fig. 4.3b, F>1 regime).

4.3 Accumulated precipitation

To give an overview of the location of the precipitation systems during these storms, we present infrared and water vapor satellite data during a time when heavy precipitation was falling over the LM region. The infrared satellite images show in cyan clouds with the coldest tops. According to the infrared image for 0500 UTC 20 September 1999 (Fig. 4.5a), during IOP2b most of the cold clouds were found in a comma-shaped feature extending from the British Isles to the central Mediterranean Sea. The cold tops were mesoscale features suggestive of convective cells in northern Italy and the Ligurian Sea. The water vapor satellite image shows in green (brown) regions of high (low) water vapor content. In the water vapor channel for the same time (0500 UTC 20 September 1999, Fig. 4.5b), these convective elements are also identified. The mass of dry air to the east of the Mediterranean coast of Spain clearly shows that at this time the intense precipitation over the LM region was pre-frontal,

in fact the front did not reach the region until very later in the event (around 1700 UTC 20 September 1999). For IOP8, the infrared satellite image for 0800 UTC 21 October 1999 (Fig. 4.6a) depicted deep convective cells over northern Italy and to the east of Corsica and Sardinia. The lack of clouds to the lee of the Alps (arch-shaped narrow band to the north of the deep convective cells) reveals the strong subsidence (Foehn phenomenon) observed here during this event. The water vapor image at this same time confirms the features seen in the infrared and shows that once again the intense precipitation was ahead of the front (Fig. 4.6b).

The impact that the different flow regimes had on the accumulated precipitation amounts during these storms is evident from the patterns of rain gauge data. Fig. 4.7a shows the rain accumulated in gauges during IOP2b. Accumulations of over 100 mm of rain were measured at sites on the western slopes of the Lago Maggiore region, with one site recording 265 mm of rain. Note that the precipitation maximum is located where the east-southeasterly flow over the Po Valley and the southerly flow over the Ligurian Sea converge (Fig. 4.3b). To the southwest of the Lago Maggiore, there was also enhancement of the rainfall at the foot of the mountains. This enhancement formed the northern segment of a northeast-southwest oriented line of high values that extended as far south as 45°N. High accumulations were also seen upslope of the western side of the Friuli region, where the MC2, as in LM, also depicted low-level winds perpendicular to the terrain (Fig. 4.3a).

In IOP8, accumulations in excess of 100 mm occurred at few locations around the Lago di Garda (Fig. 4.7b). However, the amounts of precipitation accumulated over the Lago Maggiore region were below 100 mm, no higher over the lower slopes than over the Po Valley. The precipitation patterns of the two events were thus strikingly different and consistent with the hypothesis that the flow corresponded to different regimes: flow up and over the mountains during IOP2b and flow around or blocked

during IOP8, i.e. the two Froude number regimes identified in the radar climatology (Chapter 3). The association of these rain patterns with high and low Froude number regimes will be explored in this and following chapters.

During IOP2b, the MC2 model successfully predicted the precipitation around the Lago Maggiore region. There is a northeast-southwest oriented area extending along the foothills of this region with accumulations exceeding 200 mm in some localized spots, in agreement with the measured values (Fig. 4.8a vs Fig. 4.7a). Additionally, there are two other regions of high accumulations: Friuli with accumulations around 100 mm, below the observed values and the Maritime Alps where the precipitation compares well with the observations. This accumulated precipitation field is very similar to the 24 h accumulation MM5 simulation conducted by Rotunno and Ferretti (2002) for the rainiest day of this event (not shown).

During IOP8 (Fig. 4.8b) the model does not duplicate the observed precipitation pattern (compare with Fig. 4.7b). The accumulations of more than 100 mm of rain over the Lago Maggiore region and over the gap between the Maritime Alps and the Apennines were not present in the observations. The model also missed the accumulations above 100 mm in both sides of Lago di Garda and the northwest-southeast oriented segment of accumulations greater than 50 mm seen in the observation across the Po Valley (Fig. 4.7b). The comparison with the 24 h precipitation accumulation MM5 simulation during the rainiest day from Rotunno and Ferretti (2002) has the same problems as the MC2 simulation, except that the MM5 simulation produces a more realistic description around Lago di Garda (not shown). Hypotheses regarding the missed precipitation forecast of the MC2 during IOP8 are will be discussed in Secs. 4.5 and 4.6.

4.4 Trajectory analysis

To estimate the origin of air parcels arriving at the Lago Maggiore region at a time of heavy rainfall, backward isobaric trajectories were constructed using the MC2 model data and Eqs. 2.2–2.4. During IOP2b, a parcel that started at the 840 hPa level (∼1.5 km) at 0000 UTC 20 September 1999 from a position over the sea south of the Gulf of Genoa moved northeastward and then northward the reach the south end of Lago Maggiore at 1300 UTC 20 September 1999 (blue line in Fig. 4.9a). A parcel at a lower level (940 hPa roughly 0.6 km) that reached Lago Maggiore at the same time flowed northward and then northwestward from a position on the north side of the Apennines (red line in Fig. 4.9a). A surface (10 m) parcel located over the Po Valley at 0000 UTC 20 September 1999 flowed westward then northwestward before reaching Lago Maggiore at 1300 UTC 20 September 1999 (yellow line in Fig. 4.9a).

During IOP8, a parcel that started at the 840 hPa level at 0700 UTC 21 October 1999 over the Ligurian Sea flowed northward and then northwestward to reach Lago Maggiore at 1000 UTC 21 October 1999 (blue line in Fig. 4.9b). A parcel at the 940 hPa level that reached the region of interest at the same time started close to the northwest Adriatic Sea coast (red line in Fig. 4.9b). It flowed northward, markedly turning to the left as it approached the Alps. A surface (10 m) parcel that started over the Friuli region at 2300 UTC 20 October 1999 had a southward then westward trajectory before reaching Lago Maggiore at 1000 UTC 21 October 1999 (yellow line in Fig. 4.9b). The trajectories for IOP8 had a stronger easterly component than for IOP2b. It appears that during IOP8 the 840 hPa flow (blue line in Fig. 4.9b) released some instability by going over the Apennines. During this event, convective precipitation was observed by aircraft radar over the Gulf of Genoa (Bousquet and Smull, 2002), whereas the precipitation over the Lago Maggiore region was completely stable and stratiform (next chapter). In contrast, the 840 hPa southerly flow

that reached Lago Maggiore in IOP2b passed through the gap between the Apennines and the Maritime Alps (blue line in Fig. 4.9a), hence it still had all its original instability when it reached the steep topography surrounding the Lago Maggiore area.

4.5 Temperature and stability upstream of the Alps

We recall from the Introduction that the Froude number (Eq. 1.1) gives a theoretical measure of how likely a flow is to be blocked by a certain obstacle. To gain a better physical understanding of the dynamics of the flow, we will look at the individual components that contribute to the ratio (which are the stability and the speed of the flow perpendicular to the terrain, since the height remains constant). These factors indicate the likelihood of each case to produce upslope enhancement or blocking.

The low-level mean upstream sounding from Milano were constructed for each event (Fig. 4.10). During IOP2b the atmosphere was unsaturated and conditionally unstable above 900 hPa and below 950 hPa. The 900-950 hPa layer was potentially unstable and behaving as a weak capping inversion. The environment during IOP8 was very close to saturation and stable everywhere except in a small layer below 975 hPa (Fig. 4.10). Figure 4.11 compares the temperature, mixing ratio, relative humidity, and stability of the two cases. Close to the surface IOP2b (red profile) was warmer than IOP8 (blue profile) by more than 10°C (Fig. 4.11a) and had twice as much moisture close to the surface (Fig. 4.11b). The upstream flow in IOP8 was saturated except at the surface (Fig. 4.11c). However, because it was colder than IOP2b, the absolute amount of moisture was much less. To indicate stability quantitatively, we calculated the dry (N_d) and moist (N_m) Brunt-Väisälä frequencies according to Eqs. 1.2 and 1.3, respectively. Figure 4.11d compares the stability calculated from Milano mean sounding. IOP8 was absolutely stable, with both ${N_d}^2$, ${N_m}^2 > 0$. IOP2b

was slightly unstable in terms of ${N_m}^2$, which was slightly negative. This slight instability apparently was extremely important and it had two effects. Firstly, the low static stability indicates that the air easily ascended the mountain slopes and that orographic lifting and condensation were easily achieved. Secondly, the lower stability accounted for the occurrence of embedded convective cells over local peaks and ridges in the terrain, which further enhanced the rainfall in IOP2b (Sec. 5.3). This marginally unstable condition is one factor that made IOP2b similar to the Piedmont flood case (Buzzi et al. 1998, Doswell et al. 1998). In addition, the sounding information collected at Milano during the Piedmont flood (Frontero et al. 1995) indicates surface values of temperature and mixing ratio very similar to those observed during IOP2b. In contrast, the stable conditions in IOP8 made it difficult for the low-level flow to ascend over the barrier and impossible for embedded cellular convection to occur (Sec. 5.3). These factors combined with cooler conditions (implying lower saturation mixing ratios) in IOP8 evidently led to the lower precipitation amounts in the Lago Maggiore region during this event.

Mean MC2 temperature and moisture profiles over Milano were calculated to compare with observed IOP2b and IOP8 soundings. The model temperature for Milano during IOP2b (red line in Fig. 4.12a) was slightly warmer ($\sim$1°C) than the observed value (red line in Fig. 4.11a). The mixing ratio is below the observed values for the layer below 900 hPa (red lines in Figs. 4.12b and 4.11b). The lack of moisture produced an environment that was in general further from saturation than in the actual atmosphere (red lines in Figs. 4.12c and 4.11c). The stability of the atmosphere was reduced as a result of the slightly warmer model atmosphere (red lines in Figs. 4.12d and 4.11d). Nevertheless, as in the observations ${N_d}^2 > 0$, ${N_m}^2 < 0$.

During IOP8, the model's Milano sounding showed a $\sim$ 2°C warmer and $\sim$1 g/kg moister environment than the observations (blue lines in Figs. 4.12a,b and 4.11a,b).

Hence, the model atmosphere was less stable than the actual atmosphere (blue lines in Figs. 4.12d and 4.11d). However, in agreement with the observations ${N_d}^2$, ${N_m}^2 > 0$, denoting absolute stability.

4.6 Wind structure relative to Alpine barrier

To determine the potential for blocking as opposed to unimpeded rise of the upstream flow over the terrain, the magnitude of the wind in the direction perpendicular to the barrier must be taken into account in addition to the stability. As was discussed earlier, these two parameters determine the Froude number once the height of the barrier is fixed. Over the Lago Maggiore region it would be rather difficult to choose one orientation as representative of the whole barrier. We therefore examine two distinct directions (Fig. 1.1). To identify them easily, we refer to the zonal direction as "Direction W" and to the slanted one as "Direction SW". According to the Milano sounding, the profiles of the wind component perpendicular to both orientations of the barrier were much stronger at low levels (below 900 hPa) in IOP2b (Fig. 4.13). Only above 900 hPa and only perpendicular to Direction SW did IOP8 have a stronger cross-barrier flow than IOP2b (Fig. 4.13b). Note also that IOP8 had components directed away from the mountain below 925 hPa (i.e. while the low-level flow during IOP2b rose over the terrain, during IOP8 it evidently did not). According to Eq. 1.1, the weak flow (sometimes negative) normal to the barrier at low levels in IOP8, together with its stronger stability, promoted a blocked flow. Conversely, IOP2b more likely produced upslope enhancement of precipitation by lifting the lowest layer of the atmosphere, where the moisture content was greatest. Thus both the low-level wind and stability contributed to the easier lifting of the lower layer of air in IOP2b and the blocking of this same layer in IOP8.

The mean MC2 profiles of wind components perpendicular to the previously defined orientations of the barrier (Fig. 1.1) from the Milano sounding are shown in Fig. 4.14. For IOP2b (red lines) the component perpendicular to "Direction W" is somewhat overestimated, while cross-barrier flow for "Direction SW" is depicted accurately. For IOP8 (blue lines in Fig. 4.14) the model did not calculate any downslope (i.e. negative) cross-barrier components. In fact, throughout the layer shown, the wind component perpendicular to "Direction SW" was as strong or even stronger than the corresponding value for IOP2b, which was not observed in the actual atmosphere until above 900 hPa (Fig. 4.13b).

Even though the MC2 model depicted a blocked flow during IOP8 (Fig 4.4b), it seems that it was not strong enough to reproduce the flow away from the mountain, as seen in the observations (Fig. 4.13 vs Fig. 4.14). The model also forecast a less-stable-than-observed atmosphere. It appears that the reduced stability (compare to the observed) was enough to force the flow over the terrain, producing precipitation on the foothills. Since the surface flow (Fig. 4.4b) evidently did not rise over the terrain, the precipitation had to be released by a layer above.

SUMMARY:

Two intense storms representative of the blocked and unblocked regimes described in Chapter 3 have been examined in this chapter. They were used as case studies to document the dynamics and thermodynamics prevailing during different regimes. Both storms occurred ahead of a deep baroclinic trough. According to the mesoscale numerical model output, their flow at 500 and 840 hPa was strikingly similar in the region south of the Alps. However at lower levels the winds revealed a fundamental difference: flow over the mountains during IOP2b and flow around during IOP8. The difference in flow regime between IOP2b and IOP8 consequently affected the precipi-

tation distribution, producing higher accumulations upslope of the barrier in the first storm. The backward trajectory analysis from MC2 data revealed an important difference between the storms: during IOP8 the 840 hPa flow released some instability by going over the Apennines. On the other hand, the 840 hPa southerly flow that reached LM during IOP2b passed through the gap between the Apennines and the Maritime Alps. The sounding observations at Milano showed that low stability and weak cross-barrier flow prevented the air from rising over the terrain during IOP8, while for IOP2b the potentially/conditionally unstable atmosphere had a strong flow along the barrier, with the whole lower layer rising over the terrain.

The Piedmont flood is probably one of the most studied Alpine storms, hence it is instructive to compare it and contrast it with the case studies described in this thesis. Both IOP2 and Piedmont corresponded to unblocked cases. IOP2 had surface temperature and mixing ratio values comparable with those observed during the Piedmont flood; therefore, they had a similar stability structure that allowed the flow to be easily lifted over the terrain. A subtle but important difference between these two storms was the behavior of the flow over the Po Valley. While during Piedmont this flow was solely easterly, during IOP2b it had a southerly component. In the first case, the easterly flow became perpendicular to the terrain over Piedmont, therefore this was the region that registered the highest precipitation amounts. During IOP2b, the south-southeasterly low-level flow became perpendicular to the terrain over the northwest slopes of LM, producing the precipitation maximum in this region. The Piedmont flood and IOP8 had in common the depth and definition of the easterly flow over the Po Valley. The main difference between these storms was that while during the Piedmont flood the flow rose over the terrain (unblocked conditions), during IOP8 the flow was blocked, it had to turn south and leave the Po Valley through the gap between the Apennines and the Maritime Alps.

A comparison between the modeled sounding and precipitation patterns with the observations was also carried on. The stability forecast had the right sign; however, for both IOP2b and IOP8 the modeled stability was underestimated. The cross-barrier winds were better depicted during IOP2b. The description of IOP8 did not capture the downslope flow, hence the extend of the blocking was underestimated. During IOP8, the combination of a less-stable-than-observed-atmosphere and stronger-than-observed-winds, probably forced a low-level layer of air over the northwest slopes of LM, producing precipitation maxima that were not actually observed. On the other hand, during IOP2b the precipitation forecast matched the observations over the LM region.

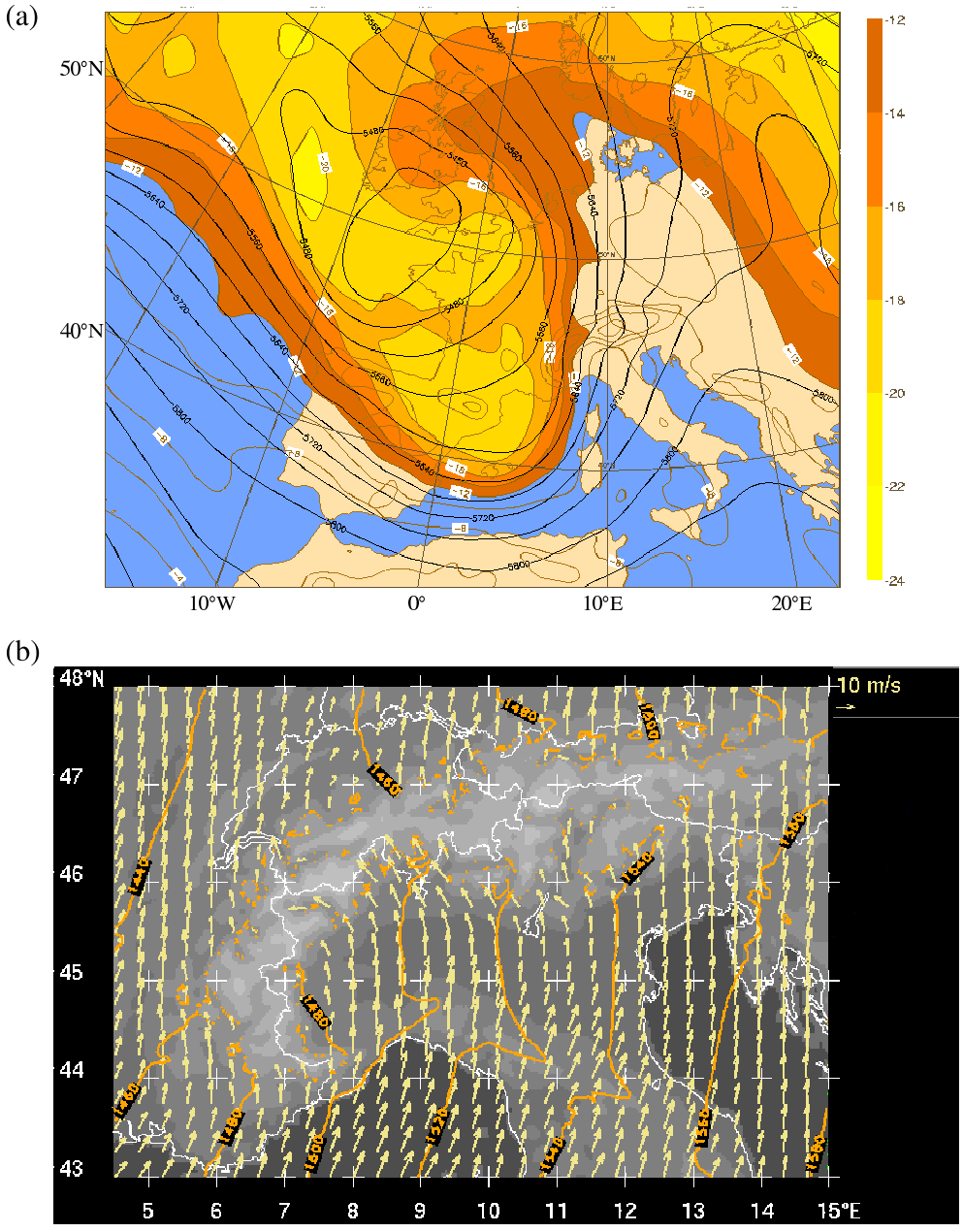

Figure 4.1: (a) ECMWF 500 hPa geopotential height (m, black lines) and air temperature (°C, color shading) over Europe for 1200 UTC 20 September 1999. (b) MC2 storm mean 840 hPa wind field and geopotential height (m, orange lines) during IOP2b along with the MC2 topography around the Alps.

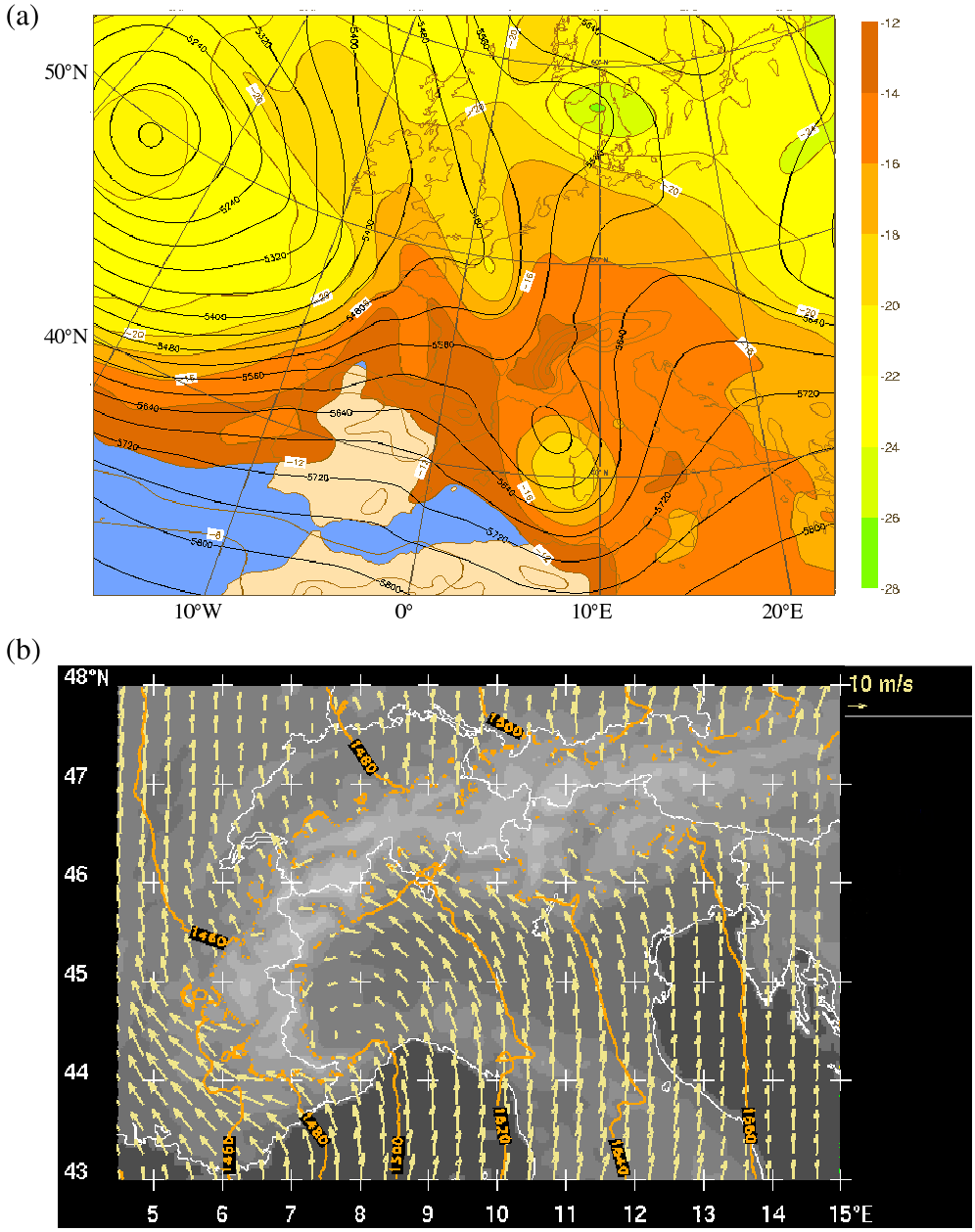

Figure 4.2: (a) ECMWF 500 hPa geopotential height (m, black lines) and air temperature (°C, color shading) over Europe for 1200 UTC 21 October 1999. (b) MC2 storm mean 840 hPa wind field and geopotential height (m, orange lines) during IOP8 along with the MC2 topography around the Alps.

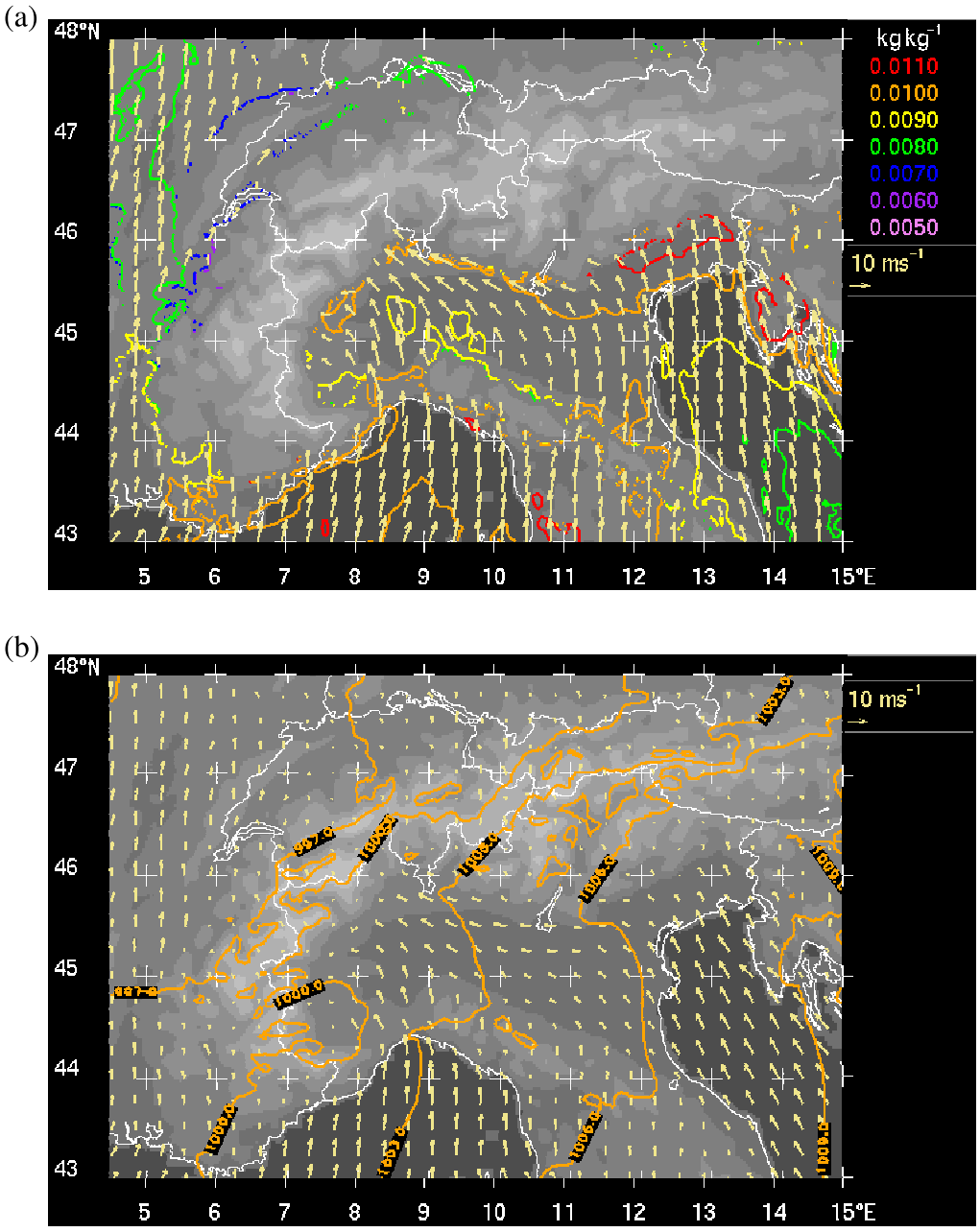

Figure 4.3: MC2 storm mean fields during IOP2b of (a) 940 hPa winds and specific humidity (kg kg^{-1}) and (b) 10 m winds and msl pressure (hPa, orange lines) along with the MC2 topography.

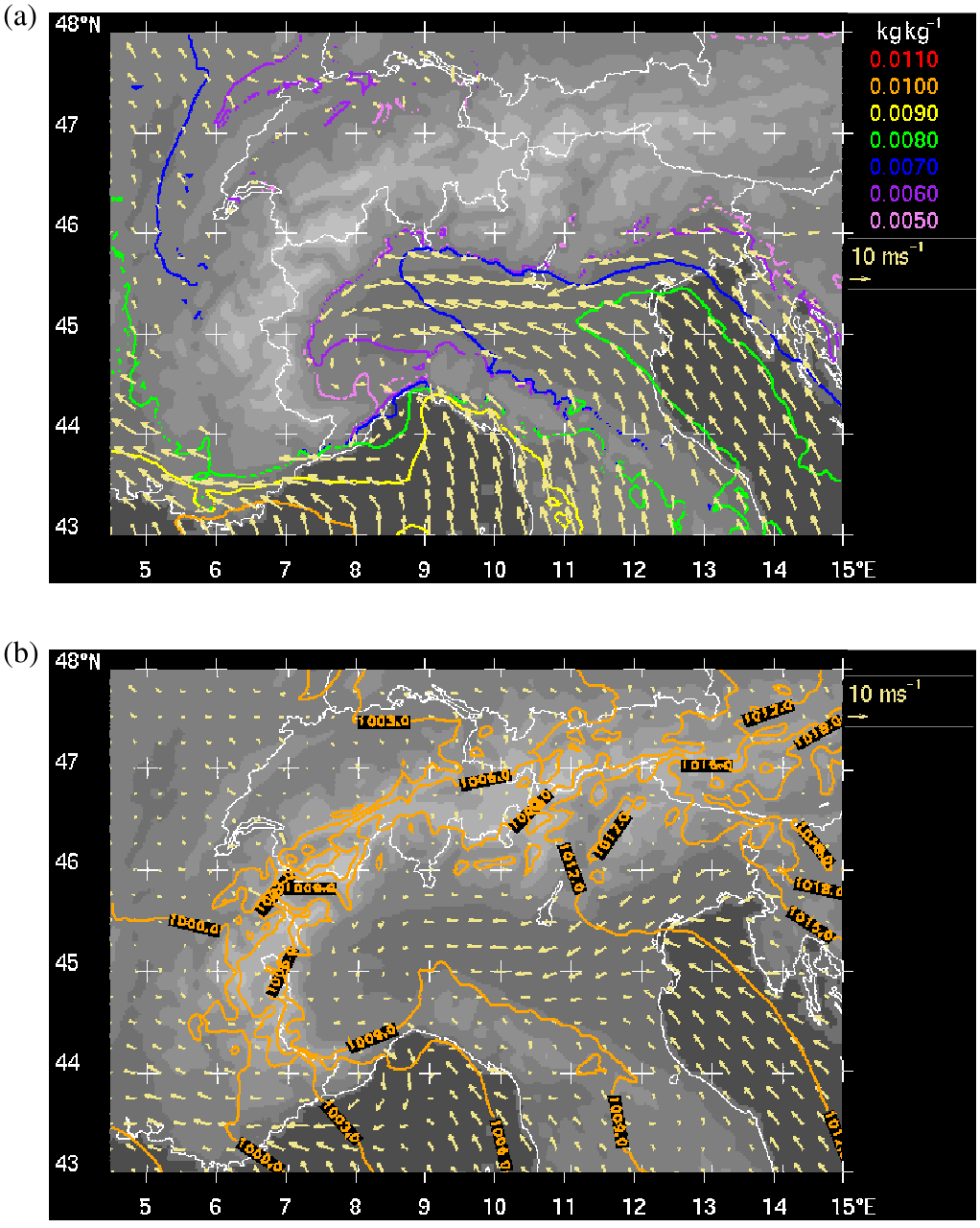

Figure 4.4: MC2 storm mean fields during IOP8 of (a) 940 hPa winds and specific humidity (kg kg^{-1}) and (b) 10 m winds and msl pressure (hPa, orange lines) along with the MC2 topography.

(a)

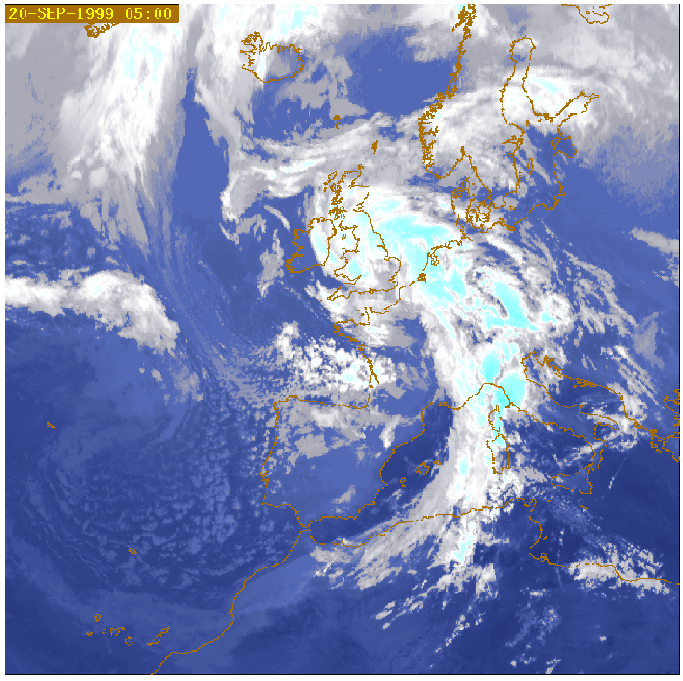

(b)

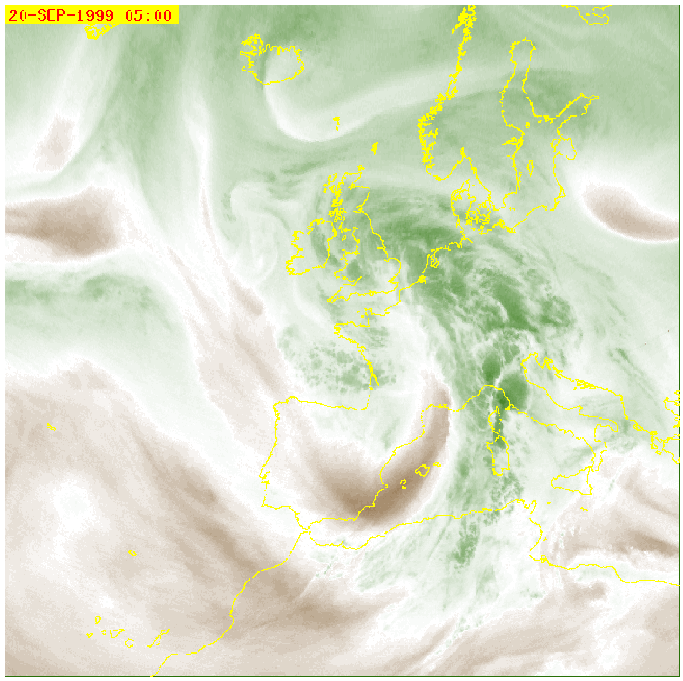

Figure 4.5: Satellite images for 0500 UTC 20 September 1999 (during a heavy precipitation spell of IOP2b) from (a) Infrared and (b) Water vapor channels.

(a)

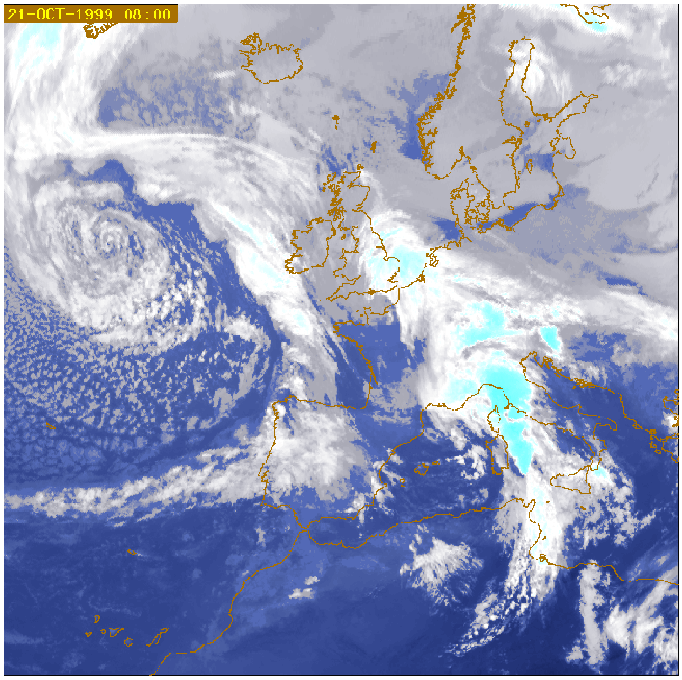

(b)

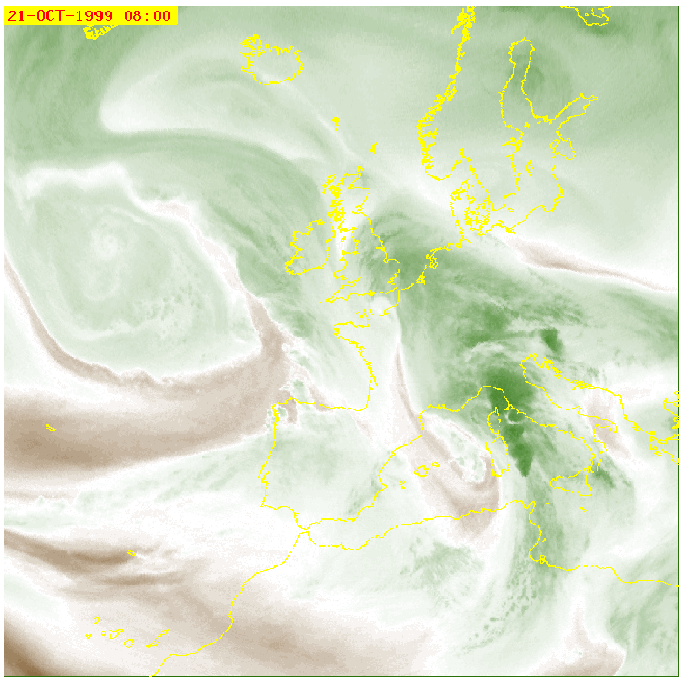

Figure 4.6: Satellite images for 0800 UTC 21 October 1999 (during a heavy precipitation spell of IOP8) from (a) Infrared and (b) Water vapor channels.

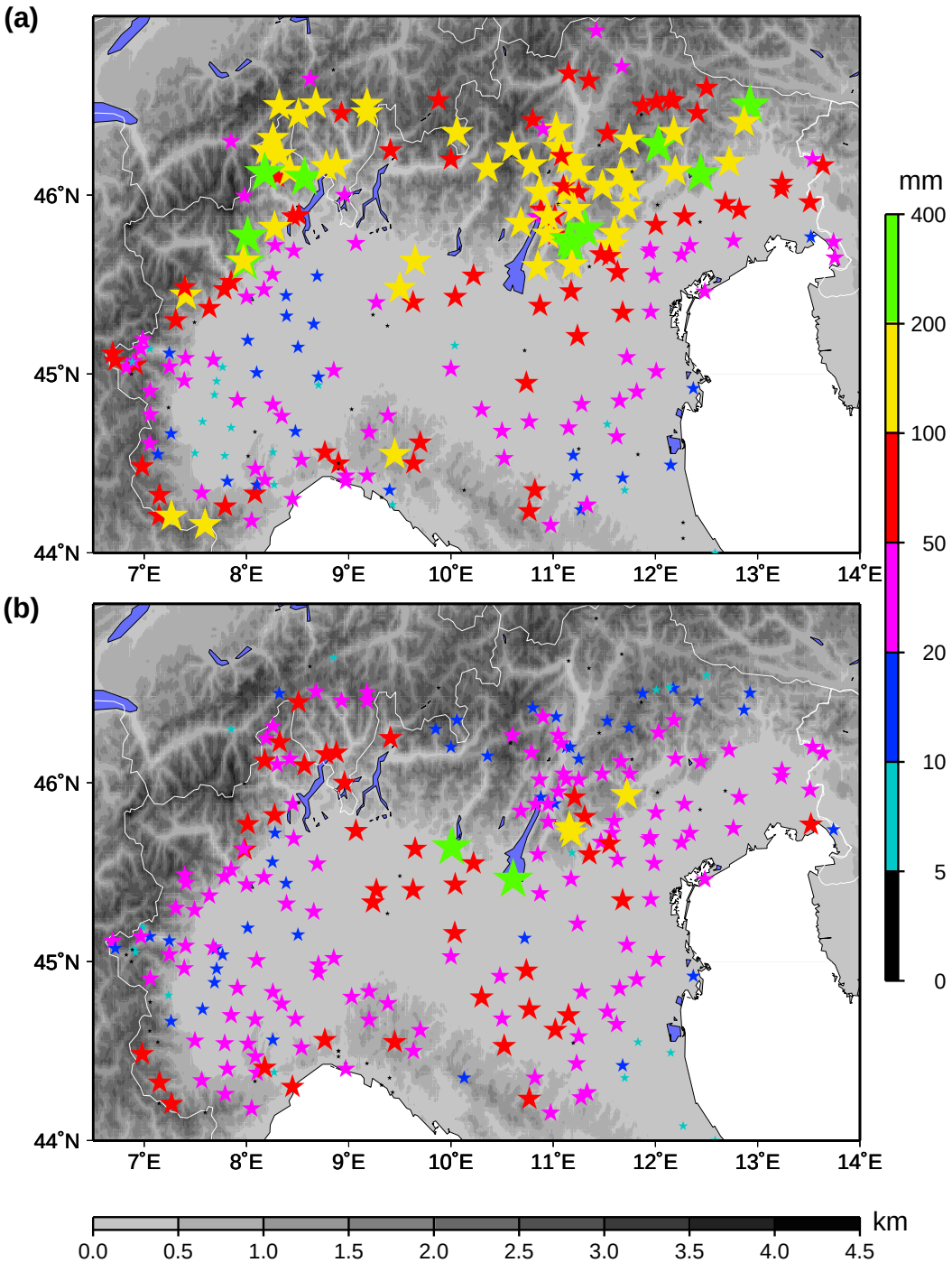

Figure 4.7: Accumulated precipitation during (a) IOP2b (1300 UTC 19 – 0100 UTC 21 September 1999) and (b) IOP8 (1200 UTC 20 – 2200 UTC 21 October 1999) from northern Italy and southern Switzerland rain gauges.

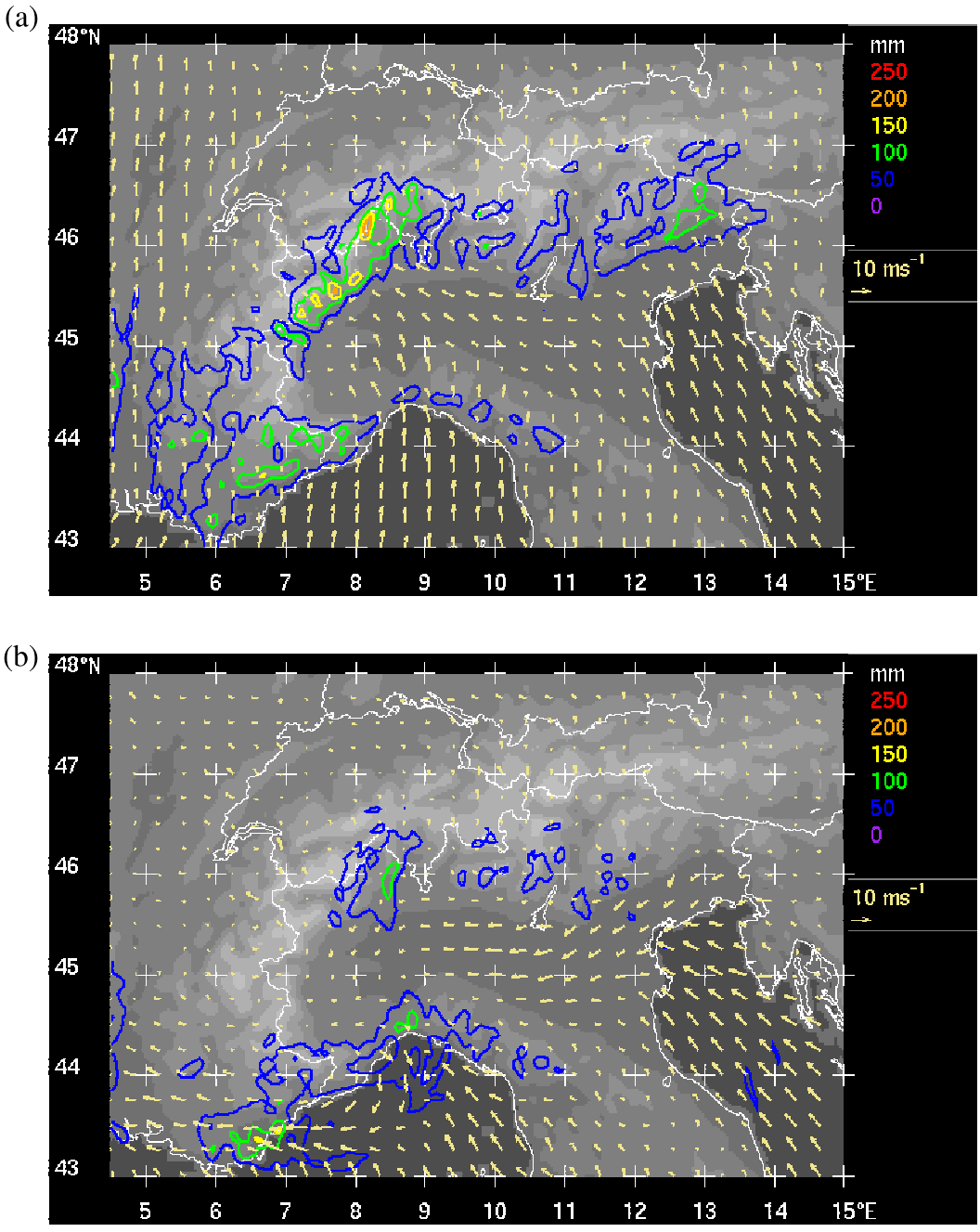

Figure 4.8: MC2 storm mean 10 m winds and accumulated precipitation during (a) IOP2b and (b) IOP8 along with the MC2 topography.

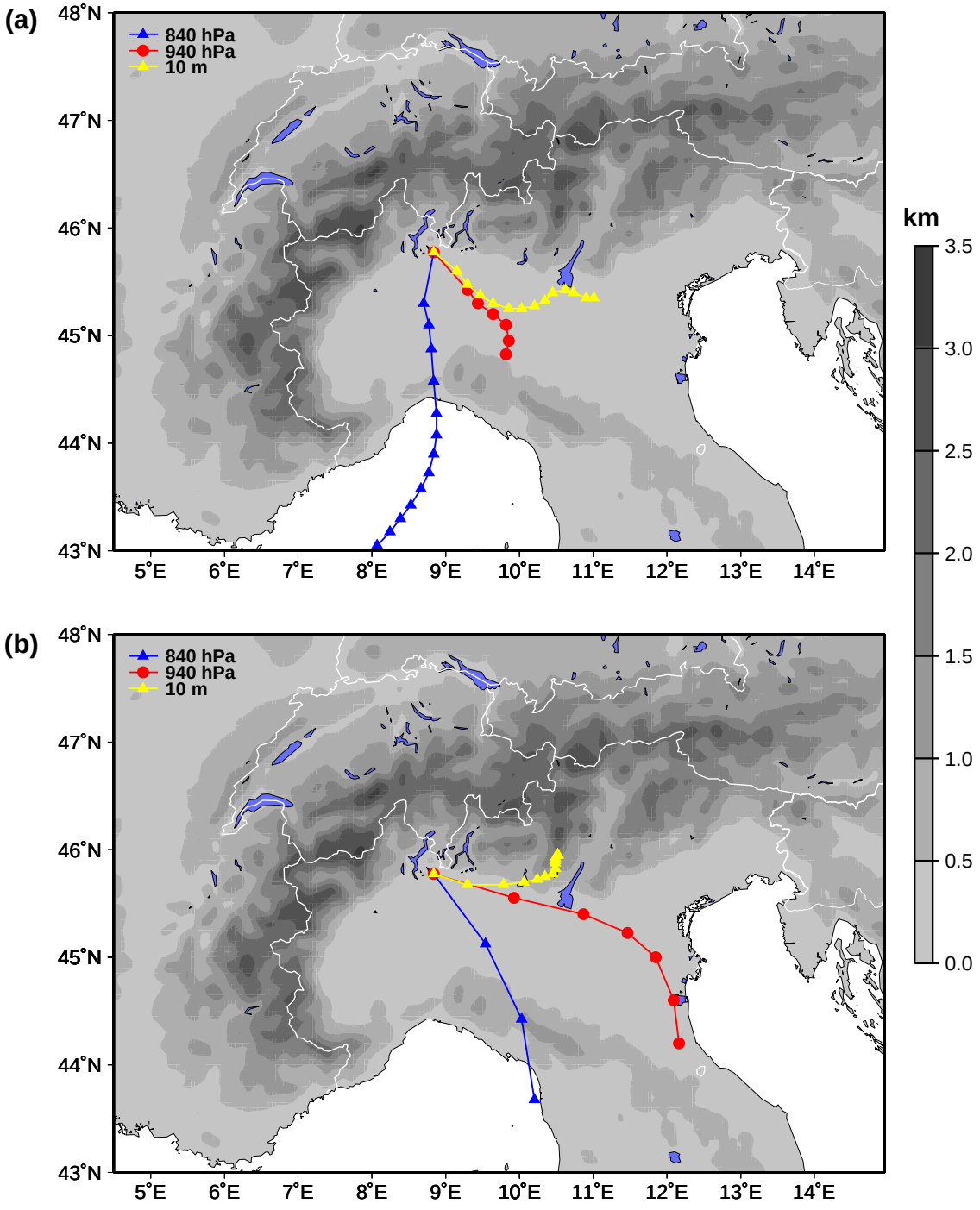

Figure 4.9: MC2 backward trajectories (at hourly intervals) for a parcel located in the Lago Maggiore region during a time of heavy precipitation during (a) IOP2b (1300 UTC 20 September 1999) and (b) IOP8 (1000 UTC 21 October 1999). The MC2 topography is also shown.

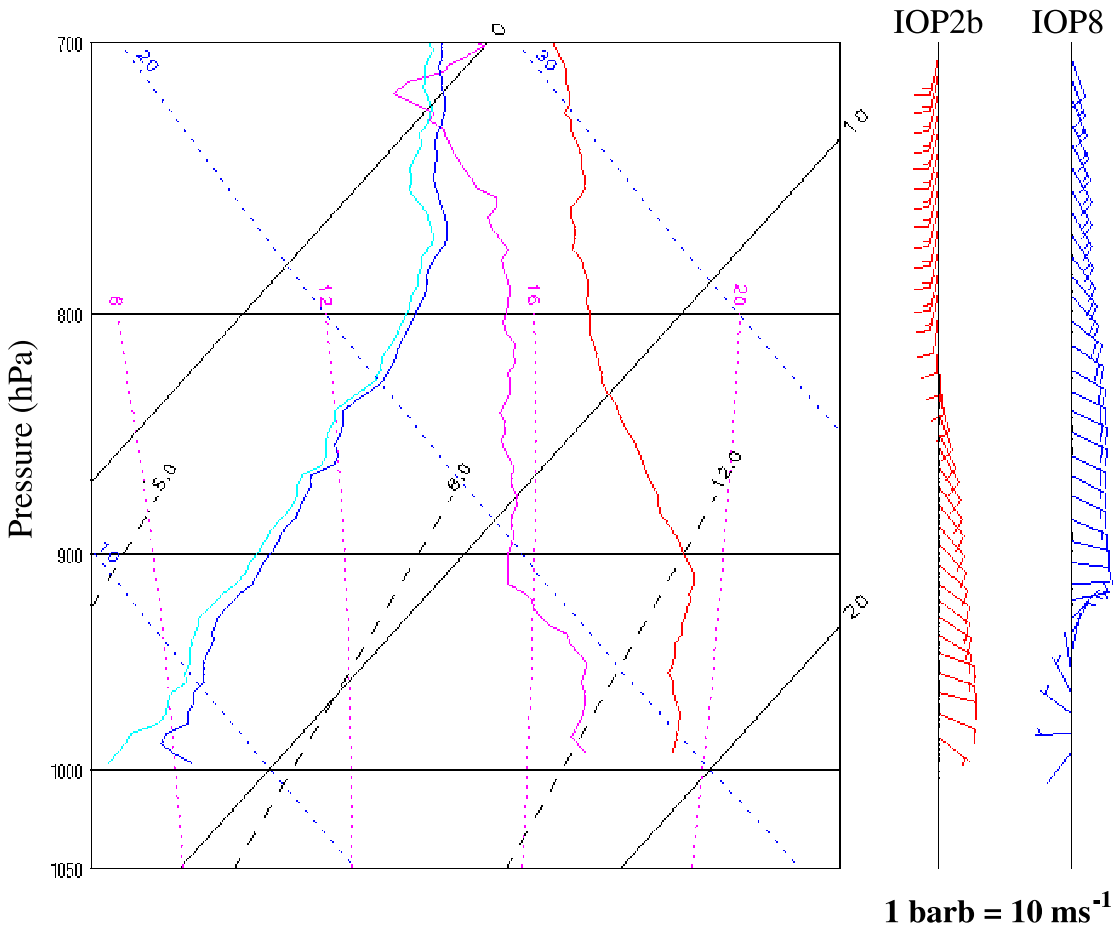

Figure 4.10: Skew-T log p diagram of mean sounding for IOP2b (red) and IOP8 (blue) taken at Milano-Linate. Solid sloping lines are isotherms in °C . Sloping short dashed blue lines are dry adiabats labeled in °C . Black long dashed lines are saturation mixing ratio lines in g kg^{-1}. Pink short dashed lines are moist adiabats labeled in wet-bulb potential temperature in °C .

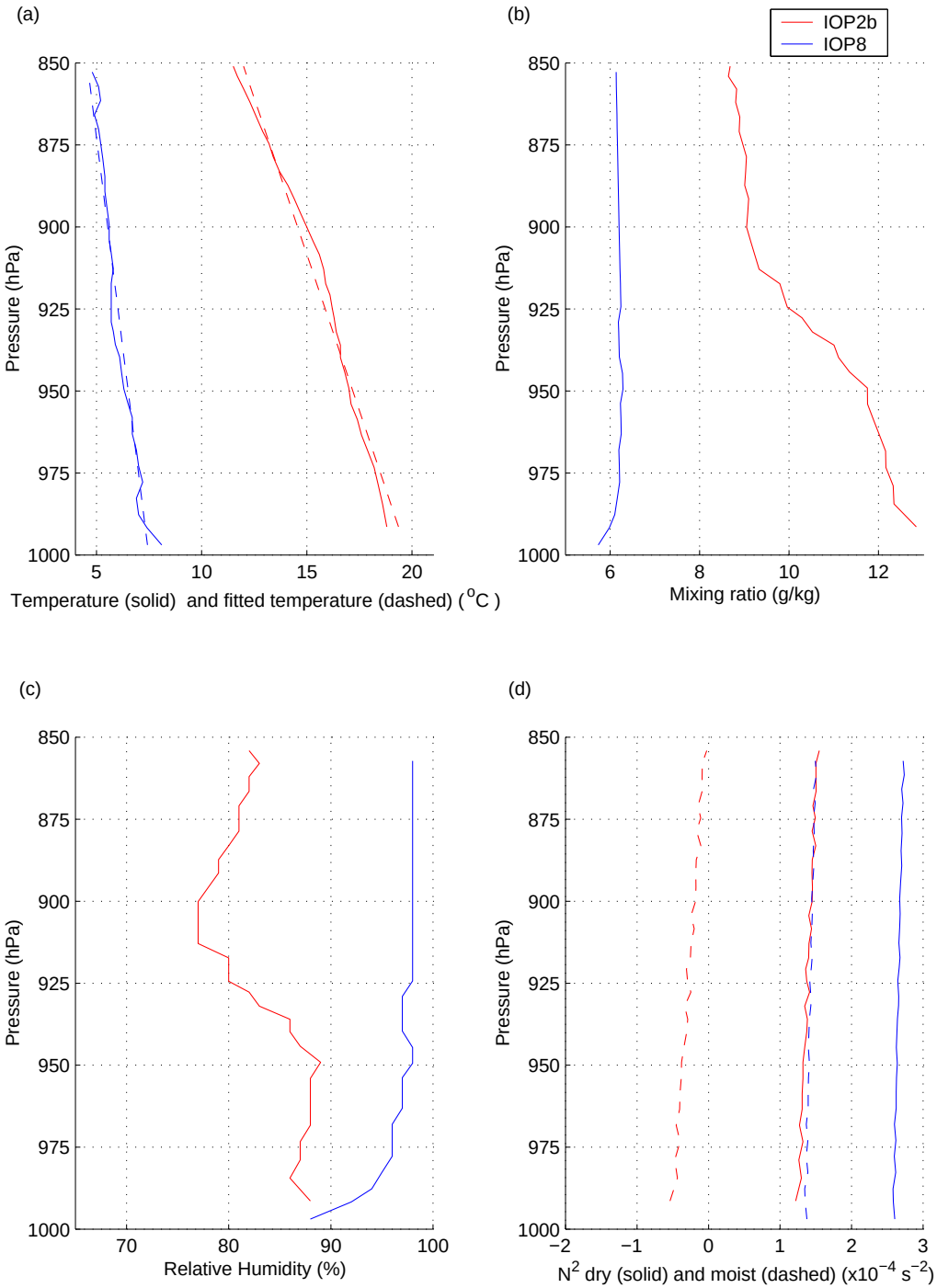

Figure 4.11: Storm mean profiles at Milano-Linate for IOP2b (red) and IOP8 (blue) of (a) temperature, (b) mixing ratio, (c) relative humidity, and (d) squared Brunt-Väisälä frequency (dry calculation shown in solid line, moist in dashed line).

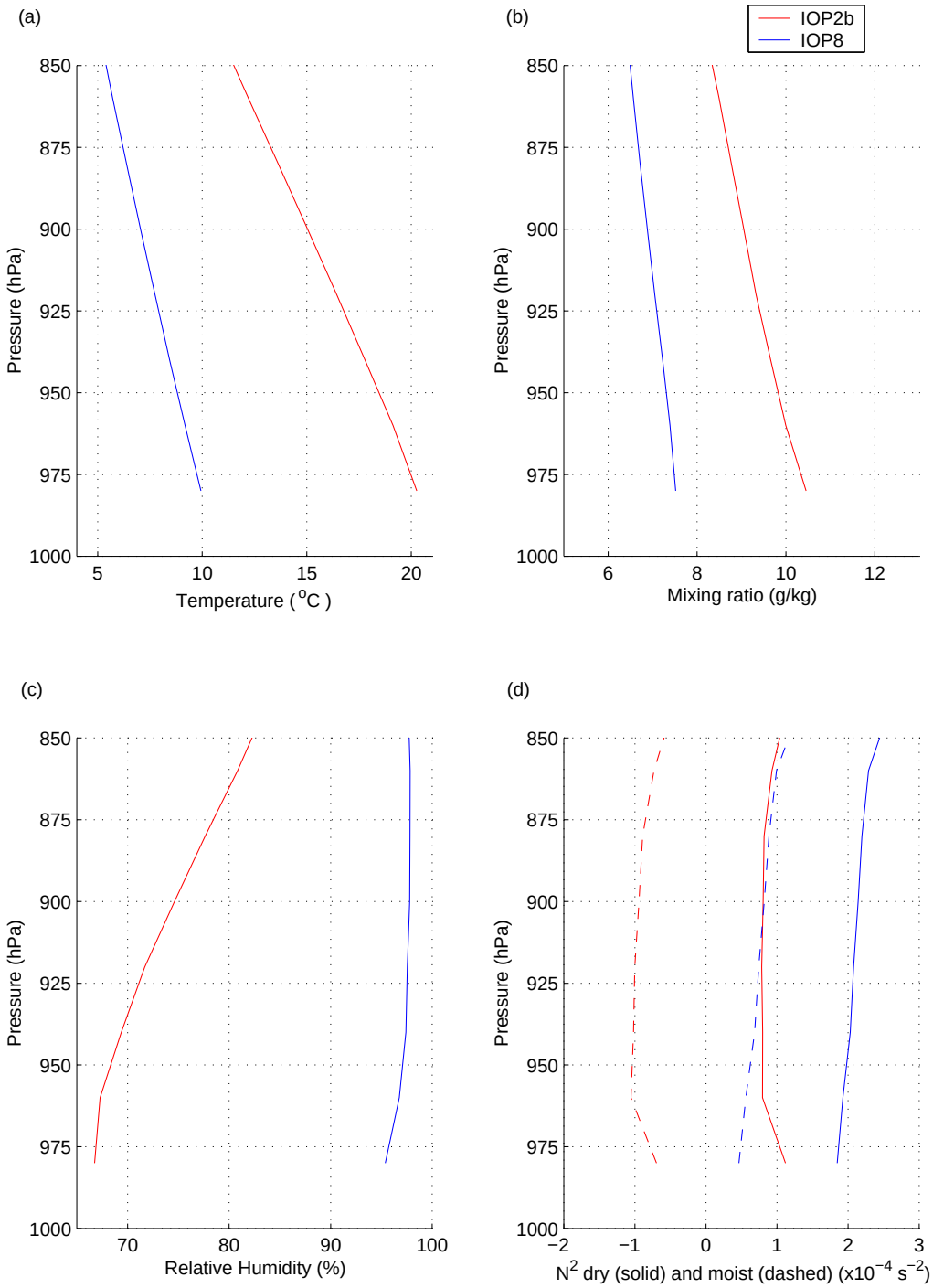

Figure 4.12: MC2 storm mean profiles at Milano-Linate for IOP2b (red) and IOP8 (blue) of (a) temperature, (b) mixing ratio, (c) relative humidity, and (d) squared Brunt-Väisälä frequency (dry calculation shown in solid line, moist in dashed line).

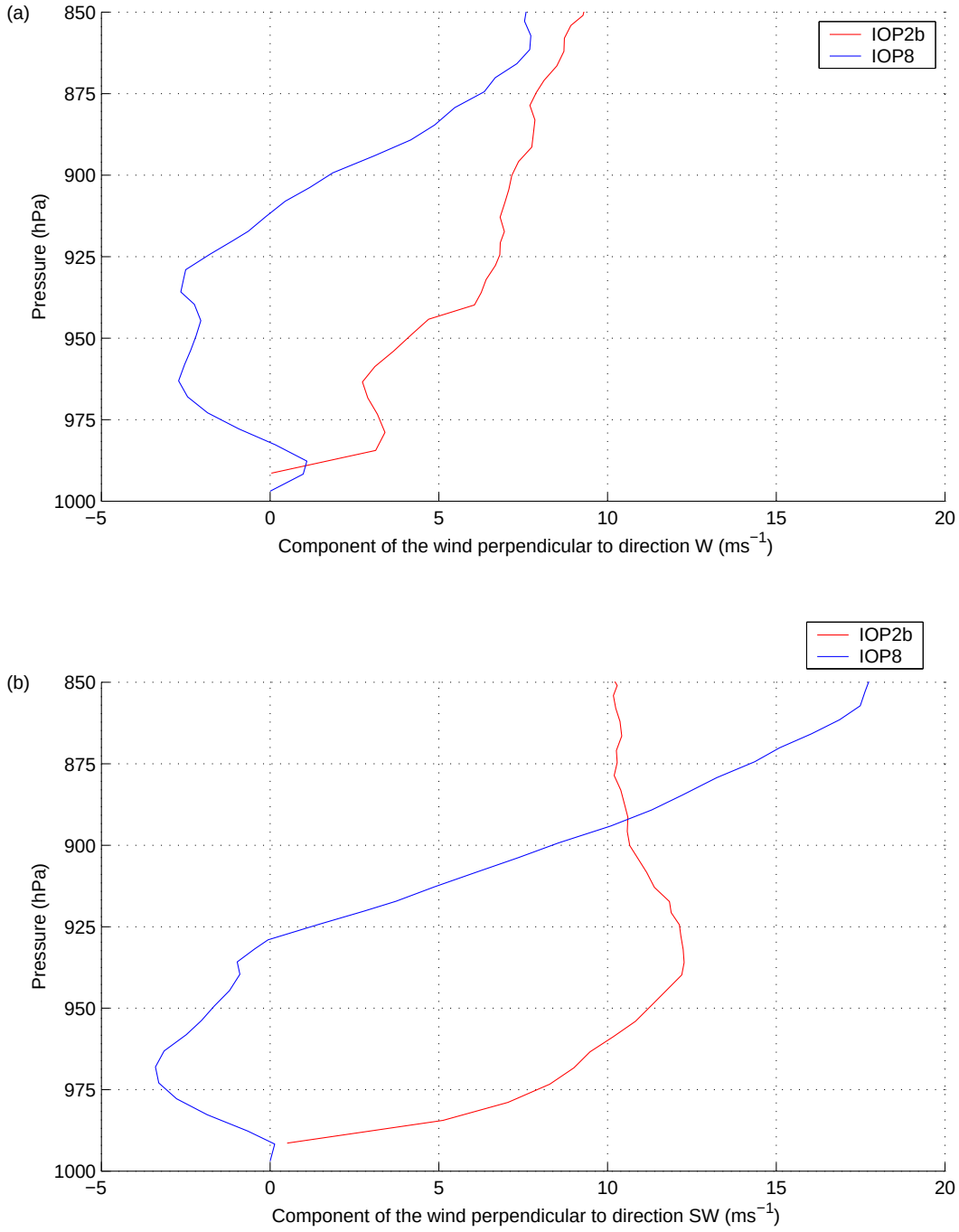

Figure 4.13: Storm mean profiles at Milano-Linate for IOP2b (red) and IOP8 (blue) of the wind speed perpendicular to the orientation of the Alps denoted by (a) W line and (b) SW line in Fig. 1.1.

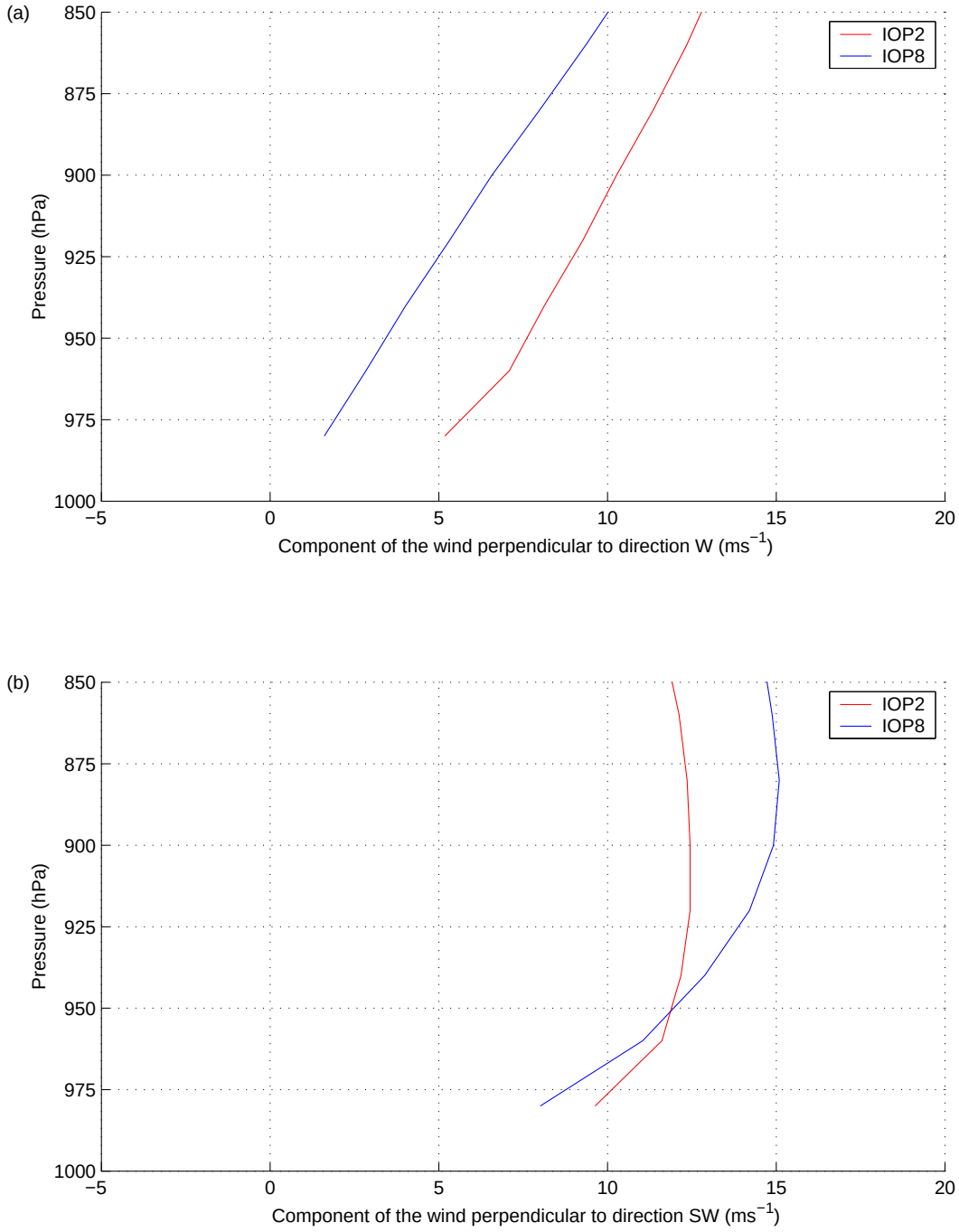

Figure 4.14: MC2 storm mean profiles at Milano-Linate for IOP2b (red) and IOP8 (blue) of the wind speed perpendicular to the orientation of the Alps denoted by (a) W line and (b) SW line in Fig. 1.1 as depicted by the MC2.

Chapter 5

PRECIPITATION PROCESSES RELATED TO FINE-SCALE TOPOGRAPHY

Above ∼850 hPa, the two rain events described in Chapter 4 (IOP2b and 8) shared many characteristics. However, their wind patterns and stability at lower levels differed significantly and the precipitation patterns on the windward slopes of the Alps were much different as well. In this chapter we seek insights into how the precipitation-producing mechanisms differed between two cases by examining radar observations in relation to details of the topography of the windward side of the Alps. The reflectivity and radial velocity patterns document the detailed structure of the radar echoes and wind patterns in the two events. The hydrometeor types indicated by polarimetric radar observations obtained during each event will be examined relative to peaks and valleys of the terrain and will be compared with MC2 output.

5.1 Wind patterns over Lago Maggiore

The airflow close to the terrain was indicated by the MAP radars. In this study, we used the method described in Sec. 3.2 to calculate mean radar patterns for the individual precipitation events or IOPs. For each IOP, the averaged reflectivity, rainrate, and radial velocity fields were computed from all the available volumes within the window of time in which the events occurred. In contrast with the seasonal means, for the individual IOPs the time resolution was not decreased and all the available volumes were included (Table 5.1).

Table 5.1: Number of radar volumes included in each IOP mean pattern

	MONTE LEMA	S–POL	RONSARD
IOP2b	309	191	52
IOP8	390	207	95

The mean patterns of radial velocity detected by radar clearly confirm that different flow conditions prevailed during each event. Figs. 5.1-5.4 show the radial velocity at different levels along with the 800 m MSL terrain contour. In panels (a)-(b) data from the Monte Lema radar show the storm mean radial velocity patterns at 4 km and 2 km MSL. Panel (c) shows storm mean radial velocity data from the RONSARD radar at 0.5 km. During IOP2b, the Monte Lema 4 km MSL flow was southerly with a speed $\sim$20 m s $^{-1}$ (Fig. 5.1a). At 2 km MSL the flow was south-southeasterly toward the convex indentation of the terrain (Fig. 5.1b). At 0.5 km MSL RONSARD exhibited southeasterly flow, i.e. flow toward the barrier, becoming perpendicular to the local orography (Fig. 5.1c). The flow pattern observed during IOP2b (Fig. 5.1) was very similar to the high Froude number climatology described in Chapter 3 (Fig. 3.7a,c). Figure 5.1 indicates that during IOP2b the entire lower layer moved toward and over the terrain, thus producing large local precipitation amounts in the LM region (Fig. 4.7).

To evaluate the MC2's version of the mesoscale structure of the flow in LM, radial velocity fields have been constructed from the three-dimensional model airflow, according to Eq. 2.1. Figure 5.2 shows the model winds during IOP2b for several levels. The model depicts the wind direction remarkably well. At and above 2 km the model slightly overestimated (underestimated) the wind speed north (south) of Monte Lema, whereas at 0.5 km it underestimated the wind speed north of RONSARD.

During IOP8, the flow at the 4 km MSL had a southerly direction with a magnitude of some 8 ms^{-1} lower than that of IOP2b (Figs. 5.3a and 5.1a). The flow at 2 km MSL had a southeasterly direction (Fig. 5.3b), in contrast to the south-southeasterly flow in IOP2b (Fig. 5.1b). At 0.5 km MSL, the wind direction varied across the region covered by the RONSARD radar. To the south of the radar, the flow was from the east, while north of the radar it was from the northeast, i.e. parallel to the local terrain (Fig. 5.3c). The flow pattern observed during this event (Fig. 5.3) resembles the low Froude number climatology (Fig. 3.7b,d). IOP8 showed a clear separation between the 0.5 km MSL level flow going away from the mountains (i.e. blocked) and the flow at 1.5 km MSL (not shown) and above flowing toward the barrier. The radial velocity fields are consistent with the sounding-derived wind profiles, which show wind direction away from the barrier below 925 hPa in IOP8 (Fig. 4.10). These results suggest that the type of flow regime (blocked or unblocked) is most apparent at the very lowest levels (0.5 km and below). The 4 km MSL radial velocity fields for IOP2b and 8 are quite similar (Figs. 5.1a and 5.3a) further suggesting that the blocked flow regime was constrained to the very lowest level.

For IOP8, the model's winds compare well with the observations at higher levels (Fig. 5.4a). However at 2 km MSL (Fig. 5.4b) the model overestimated the wind speed (compare with Fig. 5.3b). At 0.5 km (Fig. 5.4c) the model depicted an easterly flow to the south of the radar, however its intensity was overestimated and it had no northerly components as was seen on the observations (Fig. 5.3c). Airborne Doppler radar observations (Smull and Bousquet, 2001) have also shown that the intensity, extent and depth of the blocked flow inside the Po Valley were not correctly depicted by the MC2. The fact that the model gives a accurate description at all levels but the very lowest strongly suggests that these levels are key in making an accurate precipitation forecast.

5.2 Reflectivity patterns over Lago Maggiore

The mean reflectivity field for the Monte Lema radar at the 2 km MSL level for IOP2b (Fig. 5.5a) had maximum values over the lower slopes, strongest directly to the northwest (i.e. downstream) of the radar, in a similar way as the high Froude number climatology pattern (Fig. 3.6a). The pattern seen in Fig. 5.5a is mirrored in the frequency of occurrence of precipitation at the same altitude (not shown), which demonstrates that this pattern was representative of the whole storm. The 0.5 km flow (shown in Fig. 5.1c along with the 800 m MSL contour) was perpendicular to the terrain located to the west of the radars. Hence the flow at the very lowest levels impinged on the slopes to the northwest of Lago Maggiore and produced large amounts of precipitation there (Fig. 5.5a).

In IOP8 (Fig. 5.5b), the echos were in general weaker than in IOP2b and much more uniform (except for the ground-clutter echo ∼19 km northwest of the radar, which was produced by anomalous propagation due to the strong stability of the atmosphere during this event). The enhancement of precipitation over the windward slopes in this case was apparently the result of forced ascent of the layer above 1.5 km over the highly stable, blocked and easterly (or northeasterly) flowing air near the surface (Sec. 5.3). The reflectivity pattern for IOP8 (Fig. 5.5b) resembles the low Froude number climatology precipitation pattern (Fig. 3.6c). The less extreme precipitation amounts in IOP8, compared to IOP2b, were partly the result of the lower layer of air not participating in the orographic uplift and partly the result of the lifted air being cooler and more stable in IOP8. In the next section, some of the microphysical mechanisms that further account for the precipitation differences between the two storms will be described.

5.3 Precipitation mechanisms inferred from polarimetric radar observations

During the MAP-SOP, polarimetric radar data were collected by the S-Pol radar, which is a linear polarimetric radar, transmitting and receiving both horizontally and vertically polarized radiation. The linear polarimetric observables depend (and hence also give information) on the physical characteristics of the hydrometeors, such as particle size, shape, thermodynamic phase and spatial orientation. Algorithms developed by Vivekanandan et al. (1999) and by Zeng et al. (2001) were applied to the polarimetric measurements to identify the types of hydrometeors produced by the radar echoes. These algorithms are based primarily on four polarimetric radar variables: reflectivity (dBZ), differential reflectivity (ZDR), linear depolarization ratio (LDR), and specific differential propagation phase (K_{DP}). These variables are defined in Appendix A (Eqs. A.1–A.4). By considering all the variables at once, a more specific indication emerges for certain types of precipitation particles. An overview of how this is done is also given in Appendix A. The algorithms used to classify particle type either set specific thresholds (Zeng et al. 2001) or use a fuzzy logic method approach (Vivekanandan et al. 1999). This thesis will present the results from both algorithms, referring to the first one as the UW algorithm and to the second as the NCAR algorithm. Mean patterns of frequency of occurrence of hydrometeor types were constructed by keeping track of the number of times that a particular hydrometeor type appeared in a three-dimensional pixel 2.0 km x 2.0 km in the horizontal, 0.5 km in the vertical for the duration of the storm and dividing by the total number of volumes considered. The data were further normalized to account for the fact that closer to the radar the number of beams comprised in each pixel is larger than at a farther range.

We will examine data in a cross section along the white line in Fig. 2.1. This

section approximately parallels the flow at the 2 km level. During IOP2b, the storm mean reflectivity field (Figure 5.6a) showed a convective echo structure over the first peak of the mountain range, where the horizontal gradient of elevation first becomes very large. Smaller and weaker convective echo maxima appeared just upwind of the major cell over the first peak in the terrain. Apparently, convective cells embedded in the generally widespread precipitation were randomly scattered over the Po Valley but tended to be anchored systematically to the first major peak of the terrain after the airflow entered the mountainous region. The evolution of the storm consisted of scattered cells over the Po Valley. The cells were generally moving with a southerly component and advancing toward the higher elevation terrain, where they merged into cells anchored to the terrain. The maximum of reflectivity in the primary convective core tied to the first major mountain peak was below the 0°C level (3 km). Coalescence of drops may have been important in the orographic enhancement of the convective precipitation forming over the peak of the terrain. Caracena et al. (1979) proposed this idea to explain the low-altitude echo maximum in the orographic convective storm that produced the Big Thompson flood in the Rocky Mountains in 1976. This process is evidently important in the seasonal rainfall over the Alps, since the structure seen in Fig. 5.6a dominates the radar climatology of the entire fall season over the Alps (Fig. 3.3c and e).

The storm mean radial velocity cross-section (Fig. 5.6b) shows that during IOP2b a low-level jet that rose abruptly as the airflow encountered the first large peak of the topography. Such a dynamical mechanisms, made possible by the high Froude number conditions (Secs. 4.5 and 4.6), efficiently transported low-level moisture at higher levels. Figure 5.6c shows the most frequent hydrometeor types in this cross-section during IOP2b according the NCAR algorithm (similar results were obtained with the UW algorithm). The contours surround the regions of maximum occurrence of three types of ice particles: graupel, wet snow and dry snow. The red contour indicates

that graupel occurred preferentially above the first major mountain peak, directly above the reflectivity maximum (Fig. 5.6a) and also at the downwind location where the radial velocity jet reached its maximum altitude directly over the top of the first large peak of the terrain (Fig. 5.6b). The smaller graupel contour over the first peak at the ground level is an artifact produced by ground clutter and should be ignored. The upper graupel indicates a real maximum and was embedded in broad layer of persistent dry snow (cyan contour), which was melting and falling into a layer of wet snow (orange contour). Note that the frequency of occurrence of graupel was an order of magnitude smaller that for the snow, suggesting that graupel occurred intermittently. The maximum of graupel occurrence directly over the precipitation maximum seen in the reflectivity suggests that riming of ice particles just above the 0°C level, and their subsequent fallout and melting may have been another major factor besides coalescence contributing to the reflectivity maximum at lower levels. The low-level jet transported moisture above the 0°C level, efficiently saturating and condensing cloud liquid water, which was both collected by raindrops below the 0°C level and accreted by ice particles above the 0°C level. The accretion by ice particles of supercooled cloud liquid water, condensed and transported by the jet up the terrain, led to the maximum of graupel occurrence. Smith (1979) suggested that the precipitation efficiency during orographic lifting depends both on the net vertical flux of air and on the microphysical processes leading to the formation of hydrometers. Our analysis indicates that these two factors are not completely independent of each other: under situations close to saturation, the vertical flux of air may determine the microphysical processes that are activated. The microphysical and dynamical description of IOP2b is consistent with the cases that Browning et al. (1975) found to have large precipitation efficiency in that it has a moist low-level jet directed against the mountain slope.

Yuter and Houze (2002) investigated the relative roles of riming and coalescence during IOP2b. Using the vertically pointing radar OPRA situated in the Lago Mag-

giore region and making assumptions about the raindrop size distribution, they were able to obtain estimates of the vertical air velocity. In snow regions, they estimated a lower bound on the maximum updraft value. These vertical velocity estimates were used in conjunction with a 1-D microphysical parametrization Kessler model to calculate the mixing ratios of four water species: water vapor (q_v), cloud water (q_c), rain (q_r) and ice (q_i); and also precipitation process rates: condensation of cloud water (C_c), autoconversion (A_c, defined as the rate at which cloud water content decreases as a result of growth of precipitation by coalescence of cloud drops), collection of cloud water by raindrops (K_c), collection of cloud water by graupel above the 0°C level (K_{ci}), glaciation of rain into ice (G_l), fallout of raindrops form the air parcel (F_f), and fallout of ice particles (F_l). Figure 5.7 shows the results obtained Yuter and Houze (2002). They found that at the weak to moderate (2–5 m s^{-1}) vertical velocities observed during IOP2b, a layer of 2 km thickness above the freezing level was characterized by local maxima of ice mixing ratio (q_i) and collection of cloud water by graupel (K_{ci}). The model also indicated that both coalescence and riming were active and as important during this storm. This results are in agreement with the S-Pol observations. Both results point to the same precipitation growth mechanisms.

The MC2 microphysical parametrization predicted four cloud hydrometeor types: cloud water, rain water, ice crystals and graupel (Benoit et al. 1997, 2002; Kong and Yau 1997). Figure 5.8 shows model output for the same vertical cross section as Fig. 5.6, but with the MC2 topography instead. The model storm mean radial velocity field (Fig. 5.8a) shows a low-level jet sloping up the terrain, reminiscent of the upslope radial velocity jet seen in the radar data (Fig. 5.6b). However, the model's version of the jet does not rise as abruptly as the real radial velocity jet and it is stronger. The microphysical particles predicted by the model over a time interval extending throughout IOP2b are shown in Fig. 5.8b. The storm mean rain mixing ratio for this IOP was maximum over the middle mountain peak. The graupel

and ice crystal mixing ratios were also greatest over the same peak, hence the model shows the most robust orographic precipitation process over the middle peak. This predicted behavior differs from the actual rainfall, for which the radar data showed the maximum reflectivity and maximum graupel over the first (rightmost) mountain peak encountered by the windward flow (Figs. 5.6a and c). The maximum occurrence of graupel upwind of the first peak in Fig. 5.8b was associated with the mobile convective cells that were not anchored to the topography and produced the weaker cells just upwind of the terrain in Fig. 5.6a. The model topography has a 3-km resolution and an additional filter that smoothes the gradients on the terrain. The heights of the three major peaks in the model cross section (Fig. 5.8) are therefore much lower than the real topography (e.g. Fig. 5.6). The radial velocity jet did not rise above the 0°C level (∼3 km) in the model until the second peak (Fig. 5.8a), whereas in the real atmosphere the radial jet must rise above 3 km when it encounters the first major peak (Fig. 5.6b). Hence the production of graupel and rain are not triggered in the model until the flow reaches the second peak, suggesting that the smoothing of the topography can lead to prediction of heavy rain over the wrong peak. The more highly coherent and stronger maxima of microphysical variables over the middle peak were associated with the persistent flow over the topography throughout the IOP.

Fig. 5.9 shows the same cross-section shown in Fig. 5.6 during IOP8. In contrast with the IOP2b, the storm mean reflectivity field shows that during IOP8 the precipitation had a stratiform structure with a distinct bright band at the 2 km level (Fig 5.9a). The storm mean radial velocity structure in IOP8 contained an elevated jet around 3.5 km (Fig. 5.9b); however, it did not slope upward noticeably and thus did not indicate any vertical motion at low levels, as was the case in IOP2b (Fig. 5.6b). At low levels the radial component of the flow was toward the radar during IOP8, indicating blocked flow over the Po Valley. Contrasting with IOP2b, the particle identification during IOP8 exhibited a horizontal layered structure, characterized

by wet snow in the melting layer with dry snow above (Fig. 5.9c). The S-Pol radar detected no evidence of graupel whatsoever in this case. This observation is consistent with the results obtained by Hobbs (1975) where particles with little or no riming predominated in more stable situations. The radial velocity calculated from the MC2 output for IOP8 (Fig. 5.10a) does predict an approximately horizontal jet at 3.5 km. However, it does not capture the return flow at low levels. The MC2 storm mean microphysical fields over the whole period of IOP8 are shown in Fig. 5.10b. The model departs strongly from the observations by predicting the occurrence of graupel over the windward slope of the lowest peak of the terrain. As noted above, no graupel was indicated by the polarimetric radar data during this storm. With the prediction of graupel during this storm is not surprising that the model overestimated the precipitation in the upslope region. Both the lack of blocking at low levels and the prediction of graupel are probably the result of the MC2 not predicting the strong stability at low levels over the LM region, as occurred in IOP8.

To determine whether the characteristic growth mechanisms seen in the two cases analyzed here apply throughout the autumn season, we averaged the microphysical data types from the S-Pol radar over the whole area covered by the S-Pol and over the whole time period of the MAP-SOP, the results for both the NCAR (Fig. 5.11) and UW (Fig. 5.12) algorithms are presented. To construct these vertical profiles, only data from lower elevation angles (less than 20°) and pixels only out to a range of 60 km were considered. The performance of the particle identification algorithms degrades outside these ranges. The results are subdivided into blocked (Froude number < 1) and unblocked (Froude number > 1) conditions. Blocked cases had a simple stratiform structure, with a layer of dry snow, occurring most often at 3-5 km MSL, overriding a layer of wet snow and light rain (Fig. 5.11c). The top of the snow layer was at about 7 km MSL. The polarimetric data indicated practically no moderate rain or graupel in the blocked cases (Fig. 5.11d). The unblocked cases had a deeper

layer of precipitation, with dry snow extending up to about 9 km MSL (Fig. 5.11a). In unblocked cases, a layer of dry snow dominated the upper levels from 3-8 km MSL, peaking in frequency at the 4 km level. There was a layer of wet snow peaking at 2.5 km and a layer of light rain peaking at 1.5-2 km. The unblocked cases differed most notably from the blocked cases by the intermittent occurrence of moderate rain and graupel. The moderate rain peaked at the 2 km level. Graupel occurred at levels between 2.5 and 6.5 km, with a maximum frequency at about 4 km (Fig. 5.11b). Note that the horizontal scale in panel (b) in Fig. 5.11 is an order of magnitude smaller that that of panel (a) because graupel and moderate rain occurred only intermittently. The results from the UW algorithm (Fig. 5.12) are similar to those in Fig. 5.11. Note that while the NCAR algorithm subdivides the rain according to its size, the UW algorithm has only one rain category. By comparing Figs. 5.11 and 5.12, it is apparent that the combined light and moderate rain categories in the NCAR algorithm have the same signature as the rain category in the UW algorithm.

5.4 Conceptual model of orographic precipitation

Figure 5.13 proposes conceptual models of orographic precipitation mechanisms active in blocked and unblocked flows. In the blocked flow case (Fig. 5.13a, based on IOP8), the low-level flow did not rise over the terrain. The flow above about the 1.5 km level (∼850 hPa) rose over the windward slope; however, since this air was stable, no convective cells formed. The resulting precipitation was stratiform. Ice particles formed in the ascending flow, drifted downward, grew by vapor diffusion, aggregated to form snowflakes, melted, and fell to the ground as stratiform rain. The dominant particle growth mechanisms in this scenario was vapor diffusion onto ice particles (aggregation does not increase the mass of precipitation). The lifting was too gentle to produce enough liquid water for riming.

The unblocked case IOP2b (Fig. 5.13b) contrasted sharply with the case described above. There was a general background of stratiform cloud and precipitation, similar to that in the blacked case. However, since the stability of the upstream flow was low, the entire layer of air, including the surface layer, rose easily up the terrain. The inclusion of the moist low-level air in the airmass ascending over the windward slope of the range made the liquid water content over the first peak of the terrain higher than in the blocked case. In addition, when the potentially unstable upstream air became saturated, convective cells were triggered in the upslope airstream. These cells, embedded in the background stratiform cloud and precipitation, produced especially high concentrations of cloud liquid water. As a result, raindrops grew rapidly by coalescence at low-levels. Above the 0°C level, the cloud liquid water was supercooled, and ice particles in the upper parts of the cells grew by riming. The coalescence-grown raindrops and rimed ice particles fell out quickly over the peak of the terrain over which cells tended to be triggered. This cellularity embedded in the background stratiform precipitation led to an efficient fallout of precipitation on the windward slopes.

SUMMARY:

The radar-derived fields for IOP2b and IOP8 are presented in this chapter. The storm mean radial velocity pattern for IOP2b shows that during this event, in which the Froude number was high, the flow at low-levels (along with the air above) rose above the topography around the LM and produced intense precipitation over the windward slopes to the northwest of the lake. When the flow reached the steepest topography, it rose abruptly, which efficiently transported low-level moisture to higher elevations where condensation easily occurred. This produced liquid water that promoted the growth of rain by coalescence below the 0°C level and the growth of graupel

by riming above this level over the first main peak of the terrain.

On the other hand, during IOP8, the low-level air did not have enough energy to rise over the terrain. Since this flow was blocked, it did not directly participate in producing precipitation. The layer of air above 1.5 km was forced over both the blocked air and the terrain, producing large accumulations of stratiform precipitation to the northwest of the lake during this prolonged event. This case did not present evidence of graupel. Vapor diffusion was evidently the main mechanism of precipitation growth.

When the microphysical data for the whole MAP season are divided according to Froude number, it is found that low Froude number cases had a stratiform structure with dry snow aloft, wet snow in the melting level and rain below, as in IOP8. The high Froude number cases were like IOP2b in that they too had the stratiform background, but in addition intermittent graupel (surely produced when the flow climbed abover the terrain) appeared. These results indicate that the precipitation processes in IOP2b and IOP8 are prototypical of the high and low Froude number cases, respectively.

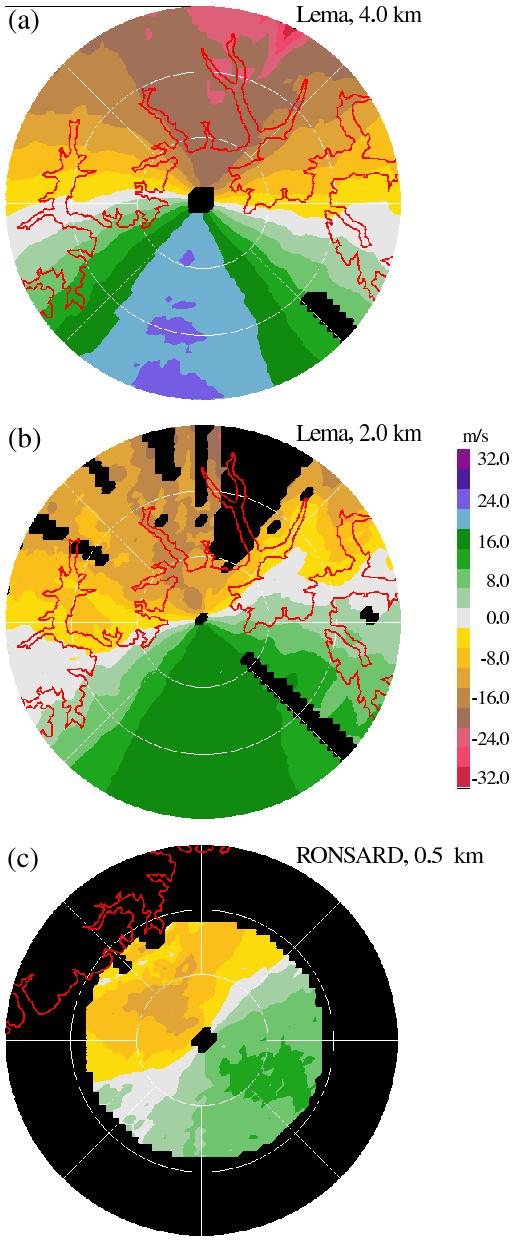

Figure 5.1: Constant altitude plots of storm mean radial velocity during IOP2b observed by (a) Monte Lema radar at 4 km MSL, (b) Monte Lema radar at 2 km MSL, and (c) RONSARD radar at 0.5 km MSL, along with the 800 m MSL terrain contour. Range ring spacing is 20 km. Note that by Swiss convention negative (positive) radial velocities denote outbound (inbound) flow.

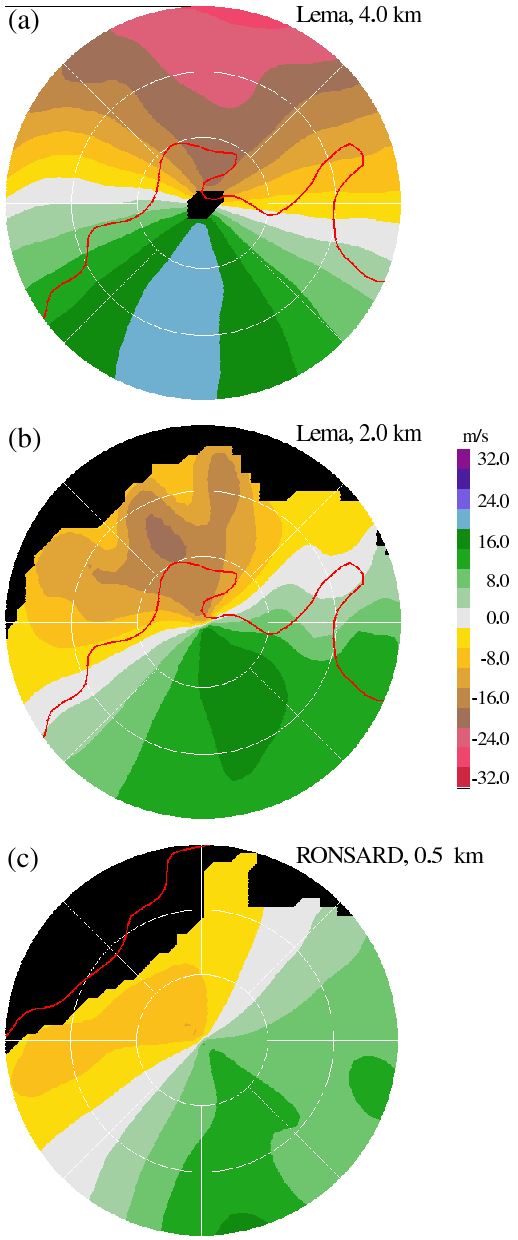

Figure 5.2: MC2 constant altitude plots of storm mean radial velocity during IOP2b observed by (a) Monte Lema radar at 4 km MSL, (b) Monte Lema radar at 2 km MSL, and (c) RONSARD radar at 0.5 km MSL, along with the model 800 m MSL terrain contour. Range ring spacing is 20 km. Note that by Swiss convention negative (positive) radial velocities denote outbound (inbound) flow.

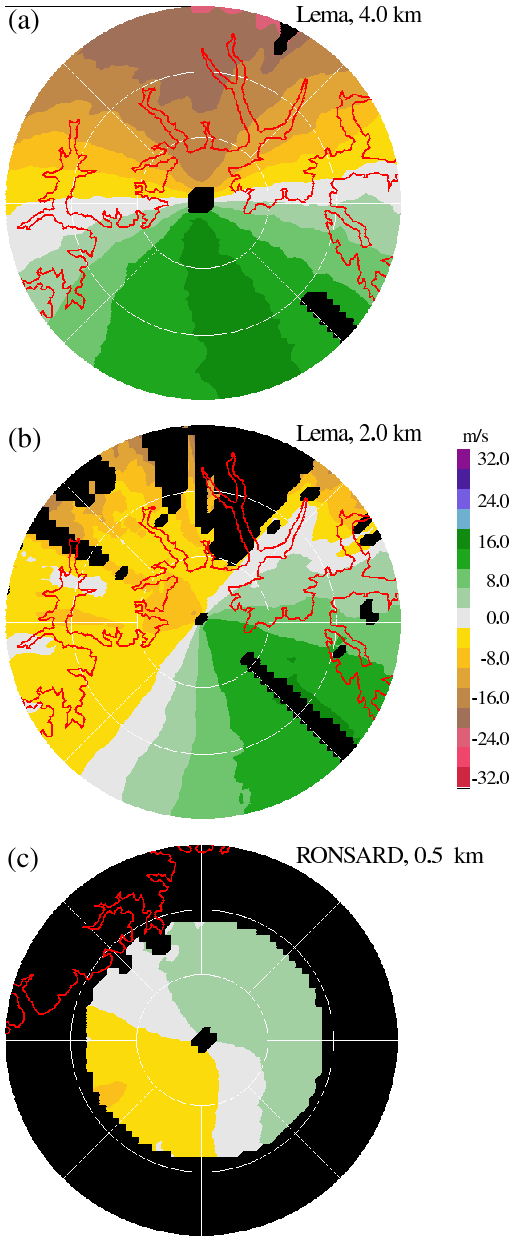

Figure 5.3: Constant altitude plots of storm mean radial velocity during IOP8 observed by (a) Monte Lema radar at 4 km MSL, (b) Monte Lema radar at 2 km MSL, and (c) RONSARD radar at 0.5 km MSL, along with the 800 m MSL terrain contour. Range ring spacing is 20 km. Note that by Swiss convention negative (positive) radial velocities denote outbound (inbound) flow.

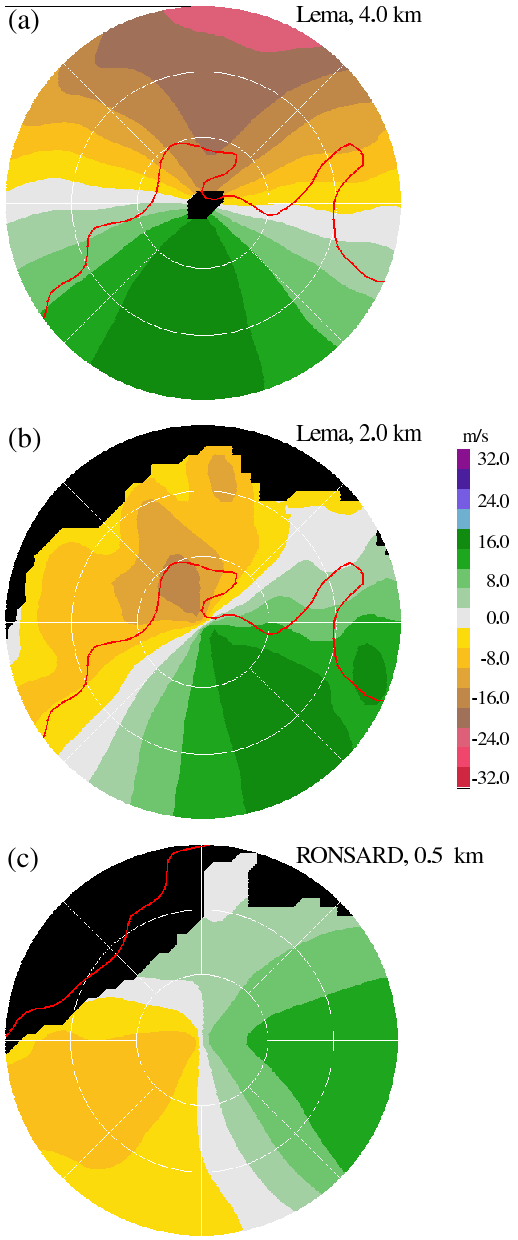

Figure 5.4: MC2 constant altitude plots of storm mean radial velocity during IOP8 observed by (a) Monte Lema radar at 4 km MSL, (b) Monte Lema radar at 2 km MSL, and (c) RONSARD radar at 0.5 km MSL, along with the model 800 m MSL terrain contour. Range ring spacing is 20 km. Note that by Swiss convention negative (positive) radial velocities denote outbound (inbound) flow.

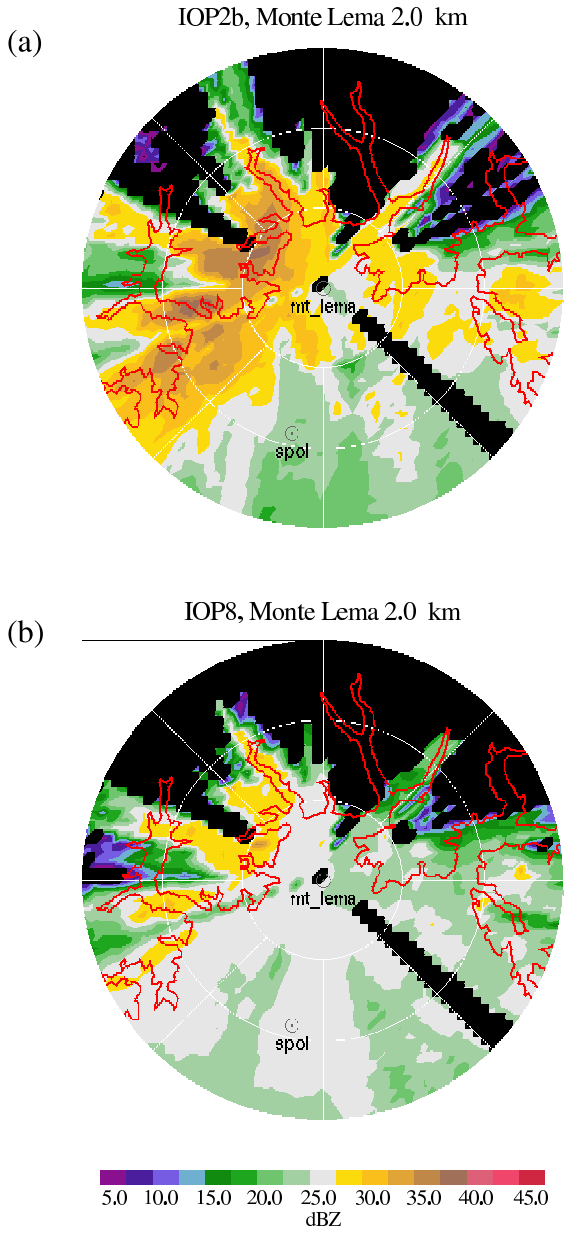

Figure 5.5: Constant altitude plots at 2 km MSL containing the storm mean reflectivity observed by the Monte Lema radar for (a) IOP2b and (b) IOP8. The 800 m MSL terrain contour is shown in red. Range ring spacing is 20 km.

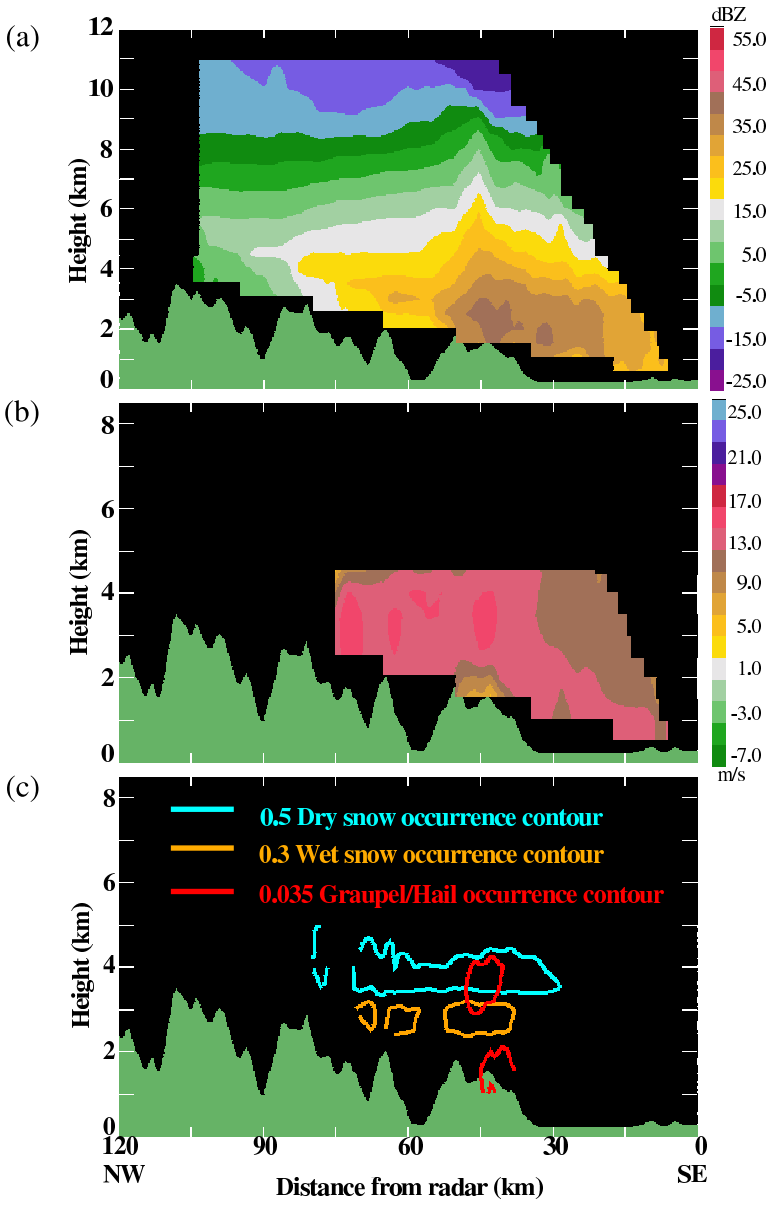

Figure 5.6: Southeast-northwest S-Pol vertical cross section along the white line shown in Fig. 2.1 during IOP2b of (a) storm mean reflectivity, (b) storm mean radial velocity and (c) frequency of occurrence of particle types identified by polarimetric radar algorithms. Contours enclose regions of most frequent occurrence of dry snow (cyan contour), wet snow (orange contour), and graupel/hail (red contour).

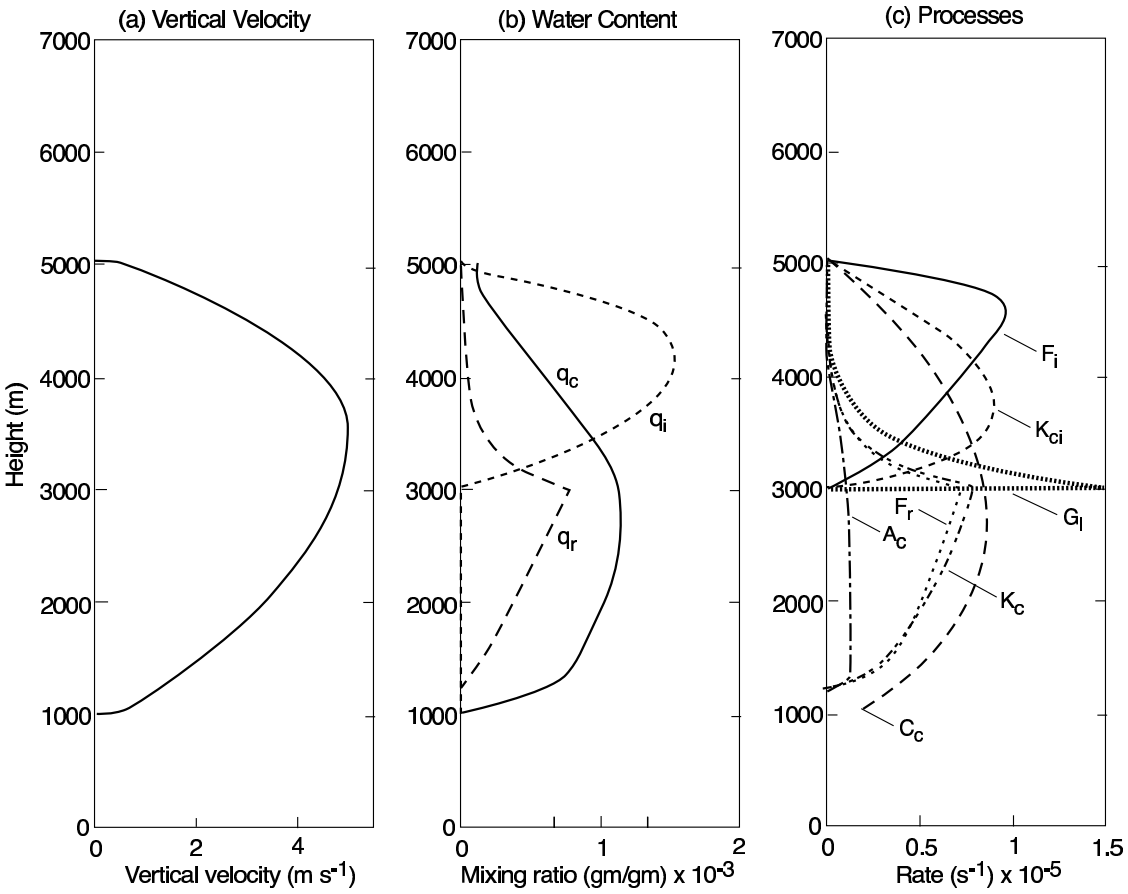

Figure 5.7: (a) Vertical velocity profile with max w = 5 ms^{-1} and updraft top of 5 km used as input to Kessler 1-D model. Vertical profiles of model output in terms of (b) mixing ratios and (c) precipitation process rates (from Yuter and Houze, 2002).

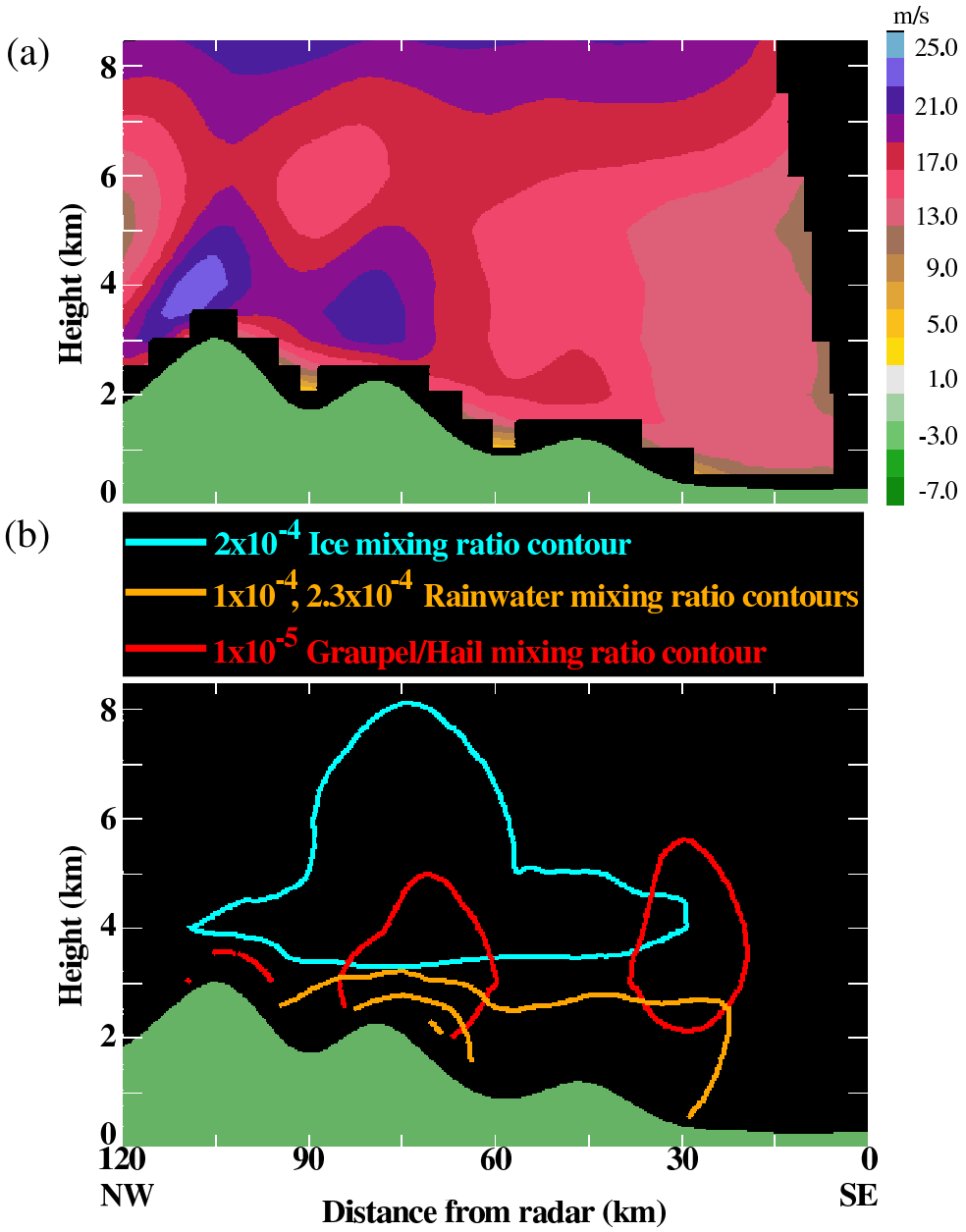

Figure 5.8: Southeast-northwest MC2 vertical cross section along the white line shown in Fig. 2.1 during IOP2b of storm mean (a) radial velocity as observed by S-Pol location and (b) mixing ratio of ice (cyan contour), rain (orange contour), and graupel/hail (red contour).

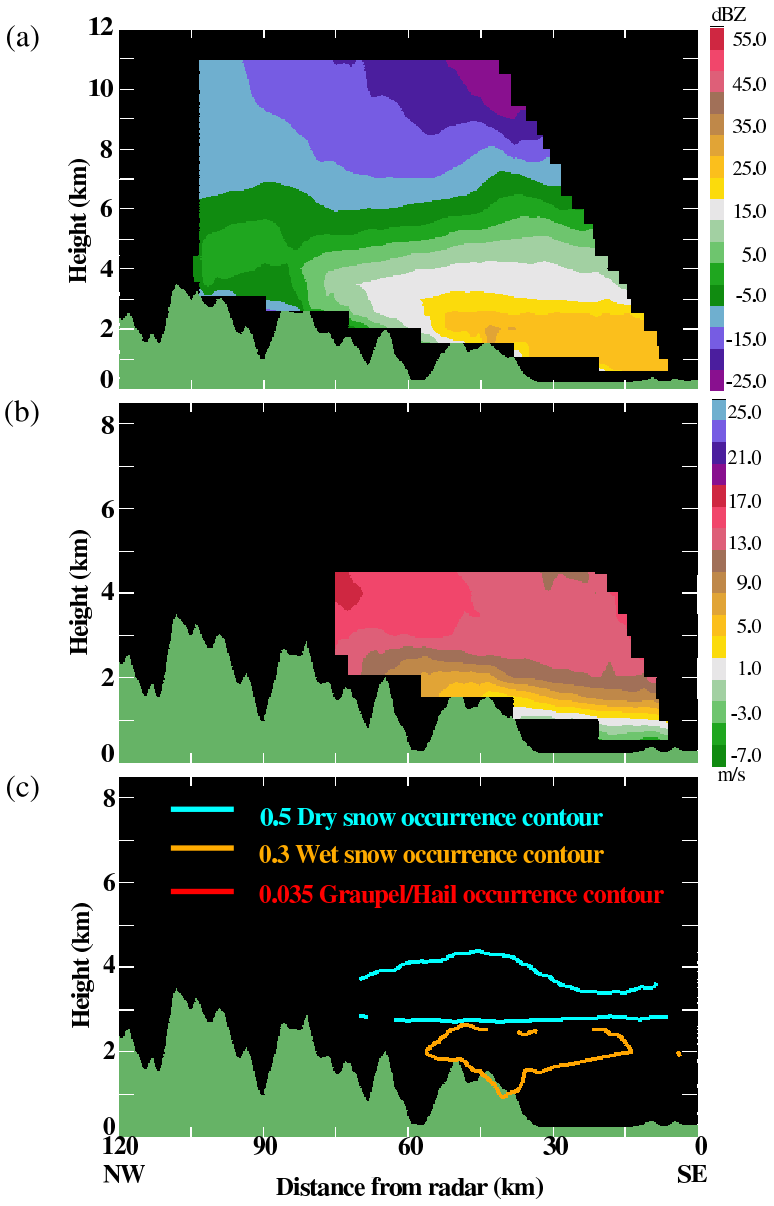

Figure 5.9: Southeast-northwest S-Pol vertical cross section along the white line shown in Fig. 2.1 during IOP8 of (a) storm mean reflectivity, b) storm mean radial velocity and (c) frequency of occurrence of particle types identified by polarimetric radar algorithms. Contours enclose regions of most frequent occurrence of dry snow (cyan contour), wet snow (orange contour), and graupel/hail (red contour).

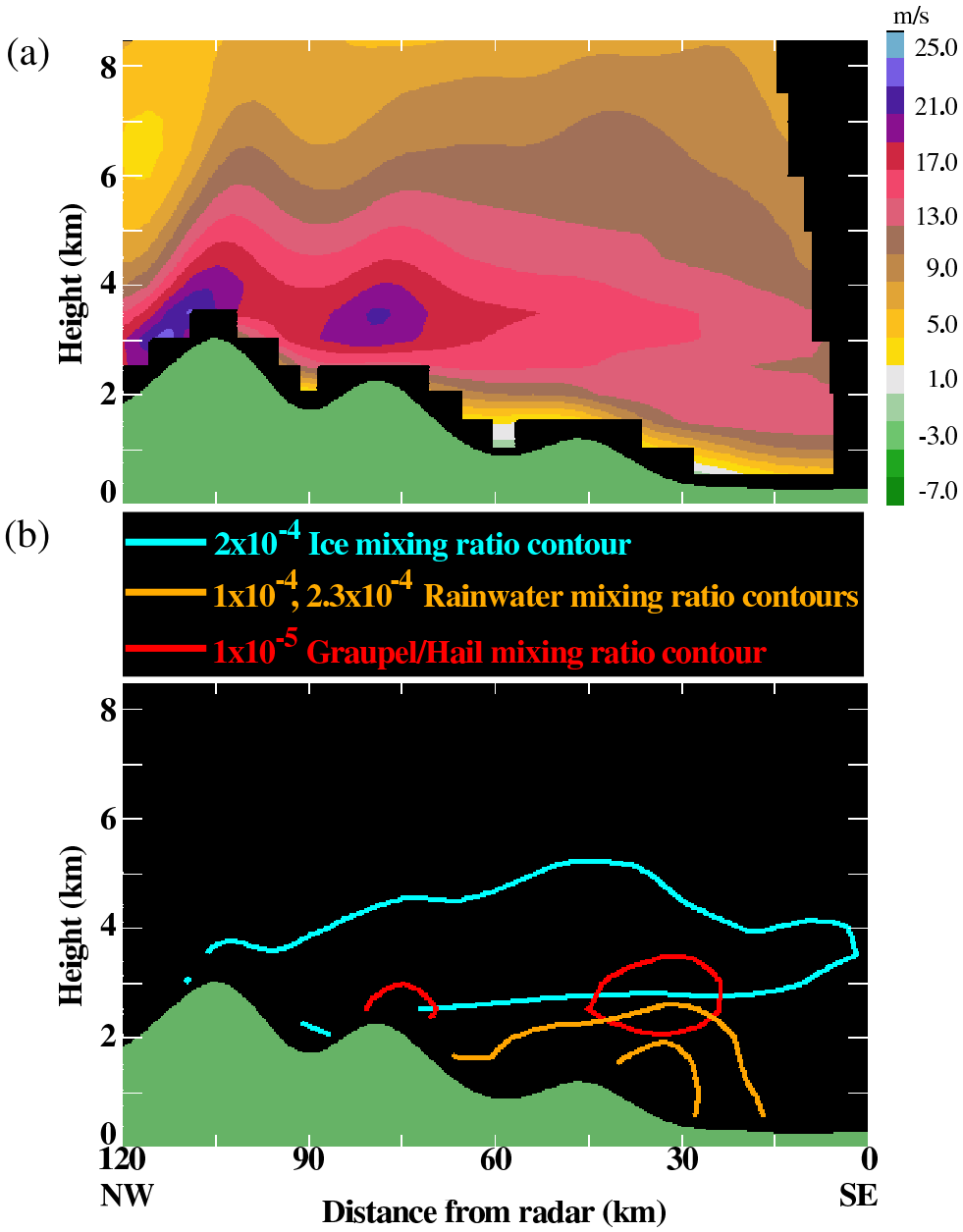

Figure 5.10: Southeast-northwest MC2 vertical cross section along the white line shown in Fig. 2.1 during IOP8 of storm mean (a) radial velocity as observed by S-Pol location and (b) mixing ratio of ice (cyan contour), rain (orange contour), and graupel/hail (red contour).

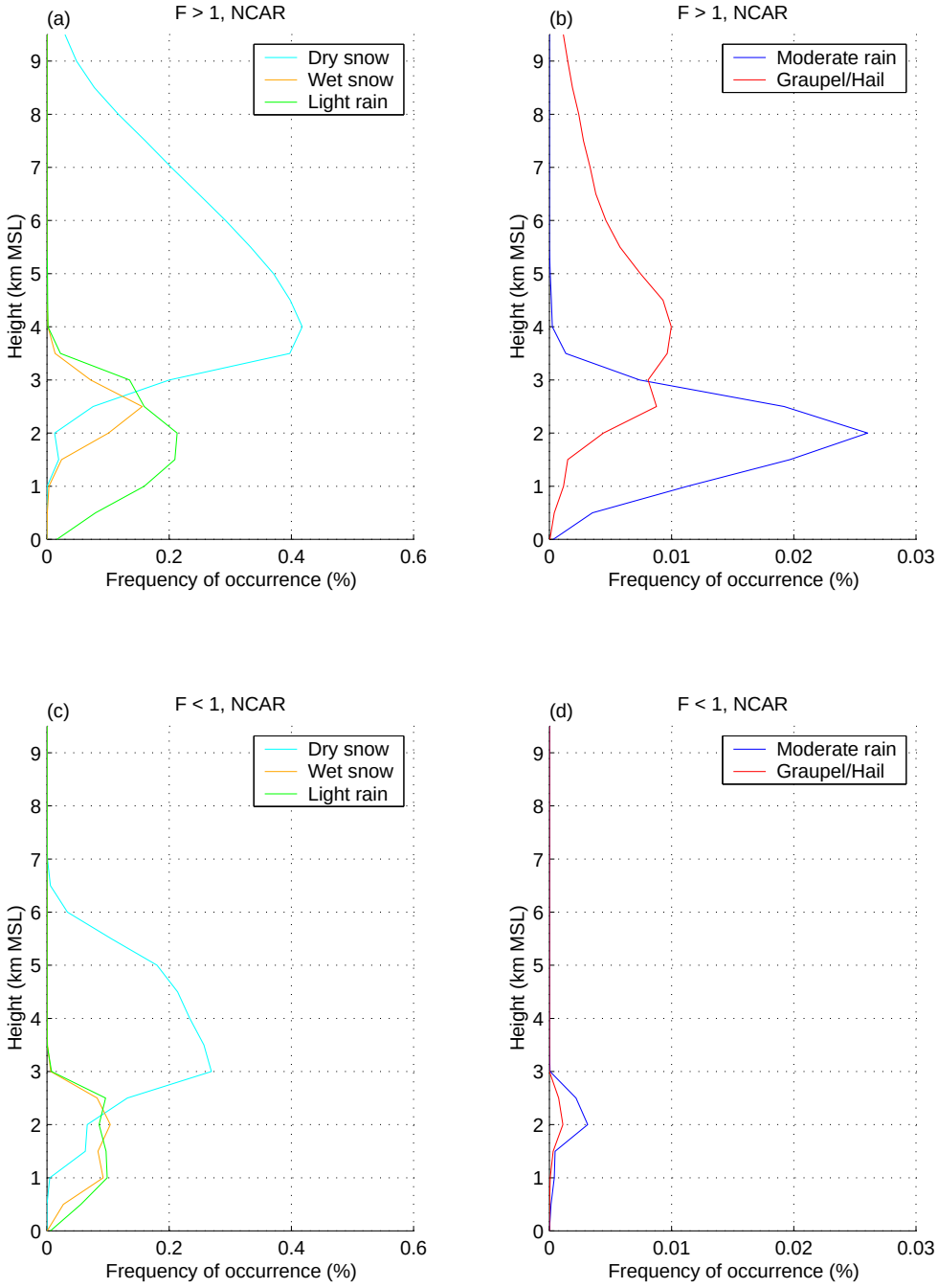

Figure 5.11: Mean frequency of occurrence of particle types identified by the NCAR polarimetric algorithm within a 60 km range and elevation angles $< 20°$ from the S-Pol when the layer-averaged 925-700 hPa flow direction from the Milano sounding was between 112.5-202.5° azimuth and the Froude number was (a)-(b) > 1 and (c)-(d) < 1 during the 1999 MAP season.

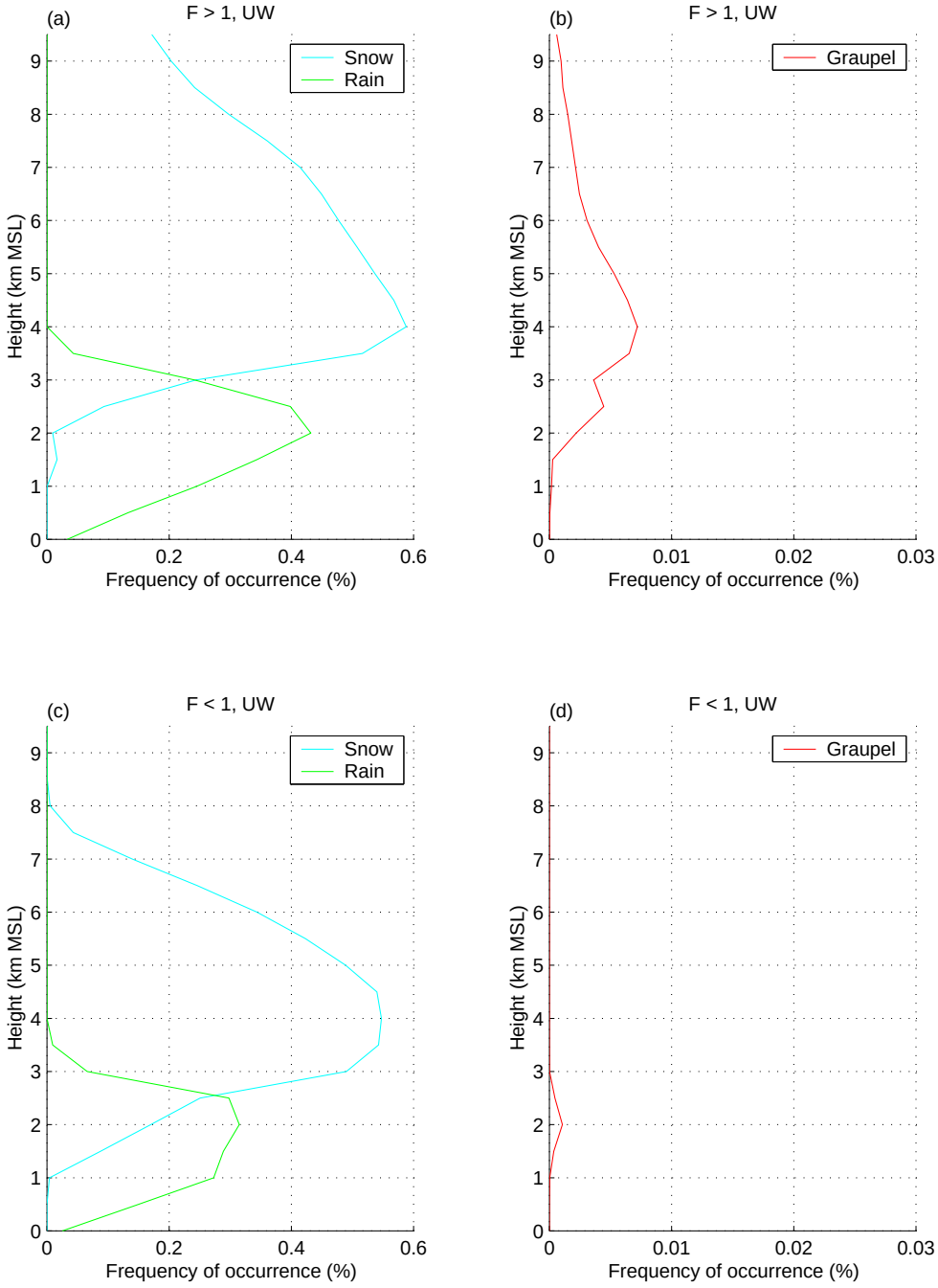

Figure 5.12: Mean frequency of occurrence of particle types identified by the UW polarimetric algorithm within a 60 km range and elevation angles $< 20°$ from the S-Pol when the layer-averaged 925-700 hPa flow direction from the Milano sounding was between 112.5-202.5° azimuth and the Froude number was (a)-(b) > 1 and (c)-(d) < 1 during the 1999 MAP season.

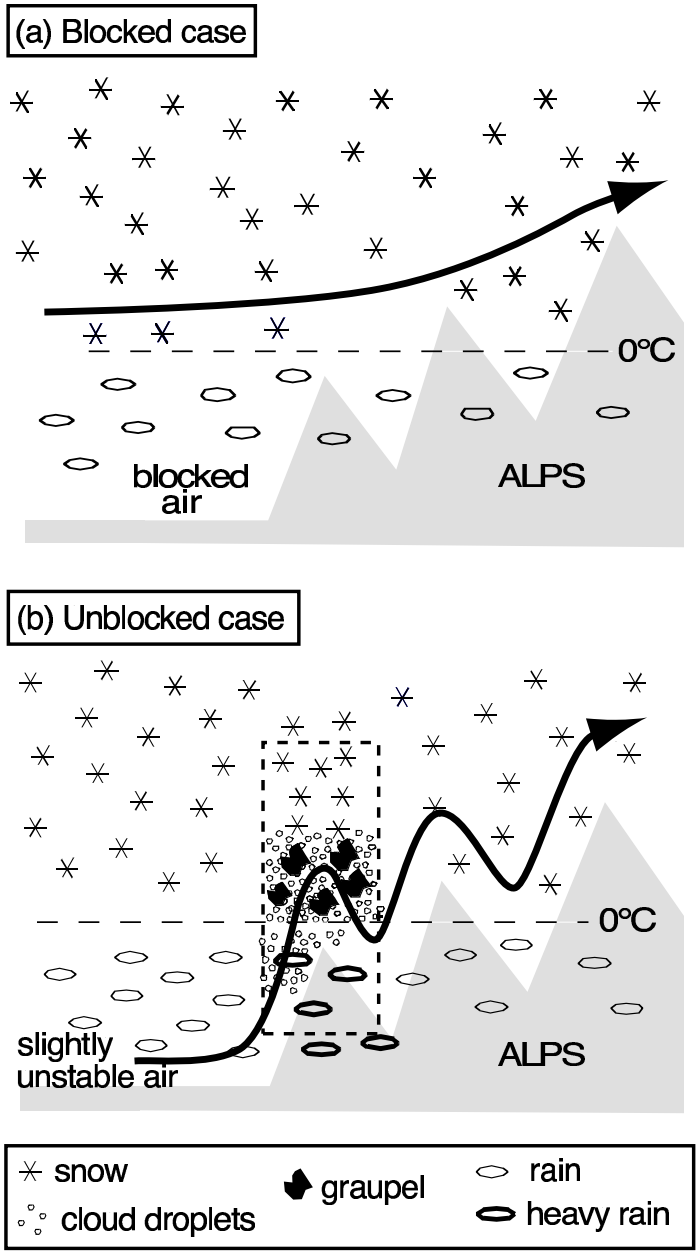

Figure 5.13: Conceptual model of the orographic precipitation mechanisms active in (a) blocked and (b) unblocked flows. The diagrams show the types of hydrometeors present in each case, along with the behavior of the flow. Dashed box in (b) indicates position of embedded convective rainshower.

Chapter 6

CONCLUSIONS

This thesis documented the precipitation growth mechanisms and flow dynamics associated with orographic precipitation during autumn Alpine storms. Firstly, the seasonal climatology of Doppler radar data for the autumn seasons of 1998 and 1999 was presented to document the detailed three-dimensional characteristics of the precipitation structure and accompanying airflow. Radar reflectivity and Doppler radial velocity patterns observed in the two seasons are in close agreement with each other, suggesting that the MAP season was in general representative of autumn rainfall on the southern side of the Alps. The radar data from the 1998 and 1999 autumn seasons showed that the mean radial velocity during rain events at the 0.5 km level was easterly, veered with height, and became south-southeasterly at the 2 km level, with magnitudes between 4-8 m s^{-1}. Consistent with previous studies of rain gauge data in the Alps (Frei and Schär 1998), the radar reflectivity showed that the heaviest precipitation occurred over the lower windward slopes and decreased in intensity toward higher terrain. Vertical cross-sections of mean reflectivity patterns for both years indicated that most of the growth and fallout of precipitation occurred at low altitudes, usually below the height of the Alpine crest.

Superposed epoch analyses of the Doppler radar data collected in the Lago Maggiore region during autumn 1998 and 1999 indicate that there is a clear relationship between the upstream flow direction and the intensity of precipitation over the Lago Maggiore region. Over the Lago Maggiore region the precipitation was significantly greater when the wind direction around the 2 km level was southerly or southeast-

erly, i.e. perpendicular to the mountain barrier. The rainfall over the lower slopes rapidly dropped off when the flow became either easterly or southwesterly. When the southerly and southeasterly flow had a high Froude number, the flow proceeded directly up and over the terrain, and the precipitation was greatly enhanced over the lower windward slopes and over the portions of the Po Valley just upstream of the mountains. With low Froude number southerly and southeasterly flows were strongly blocked below the 2 km level. However at higher elevations the airstream rose over the terrain fairly easily. Thus, the enhancement of precipitation directly over the lower mountain slopes did not have the participation of the air in the lowest 2 km, which turned eastward in response to blocking. The lifting of the low-level air appears to have been shifted upstream of the barrier crest in the blocked cases.

Secondly, two major rainstorms in MAP (IOP2b and 8) that represent the unblocked and blocked regimes were analyzed in detail. Each storm occurred with the passage of a strong baroclinic wave, and in each case the precipitation patterns on the Mediterranean side of the Alps were highly modified by the Alpine terrain. However, the modification of the large-scale flow differed markedly between the two cases since IOP2b was a high Froude number (unblocked) case while IOP8 was a low Froude number or blocked case.

Unblocked flow conditions (represented by IOP2b) had much more low-level air rising up the terrain. This low-level upslope flow produced more cloud water both below and above the 0°C level, which favored coalescence below the 0°C level and riming (i.e. graupel production) just above the 0°C isotherm. Both the coalescence and the graupel production contributed to locally heavy rain on the mountainsides. During IOP2b, the strong flow toward and over the barrier was possible because the upstream flow had low moist static stability. The precipitation amounts in the the Lago Maggiore region exceeded 100 mm at numerous locations and were double that

in some spots along the lower slopes of the Alps. The low moist static stability contributed to the high Froude number so that the whole layer of air could rise over the terrain. Since the static stability was slightly negative, instability was released as the layer rose. The upstream flow rising over the windward slopes favored the development of embedded convective cells over peaks in the terrain. These cells provided locally strong updrafts which produced locally large concentrations of cloud liquid water. The S-Pol radar observations of low-level reflectivity maximum (reminiscent of that described by Caracena et al. 1979) suggested that these conditions favored rapid drop growth by coalescence at the lowest levels. The S-Pol polarimetric data further indicated a maximum frequency of occurrence of graupel just above the reflectivity maximum, suggesting that the concentrated cloud liquid water in the cells promoted growth of precipitation particles by riming above the 0°C level. Fallout of both the graupel and the coalescence-produced raindrops favored locally heavy precipitation at the top point of the rise of the radial velocity jet over the first major peak of terrain encountered by the upstream flow. The rapid growth by coalescence and riming made the precipitation process quick and efficient over the windward slopes.

In blocking conditions (represented by IOP8), the lower-level air could not rise above the terrain. Therefore, a decoupling occurred, with the air above 850 hPa rising over the terrain, and the air below that level turning back away from the mountains. Clouds and precipitation over the mountains thus depended entirely on condensation of moisture above the 850 hPa level. The stability of the rising layer of air prevented cellular convection from forming and enhancing the orographic rainfall. Despite these handicaps, precipitation amounts were large in IOP8, though not as large as in the unblocked case of IOP2b, and were generally under 100 mm. The radars showed that the rain in IOP8 was produced entirely by a simple stratiform process over the windward slopes. The polarimetric radar observations indicated only dry snow aloft with wet snow in a well-defined melting layer and rain below. In

absence of cellular convection, graupel was not detected at any time during the storm.

The radar observations in the Lago Maggiore region for two fall seasons suggest that under southerly and southeasterly low-level winds, the precipitation events in this region subdivide distinctly into unblocked and blocked cases. IOP2b and IOP8 have proven to be instructive proxy cases for these two storms categories, respectively. The storm mean reflectivity and radial velocity patterns in these two case studies mirror the conditions seen in the high and low Froude number categories in the Lago Maggiore radar climatology. The S-Pol data collected in IOP2b and IOP8 further suggests fundamental microphysical differences between the unblocked and blocked cases. A basic widespread stratiform structure of dry snow aloft, growing by deposition, melting and falling out as rain prevails in both unblocked and blocked cases (Fig. 5.13a and b). In the unblocked case the basic stratiform structure is enhanced, since the lower layer of high Froude number upstream flow rises up the barrier. Cellular convection triggered in the upslope flow is embedded in the stratiform background precipitation (Fig. 5.13b). These enhancements give rise to graupel just above the 0°C level and heavier rain below the 0°C level directly over the major peaks of the windward-side terrain.

In third place, the microphysical analysis for the two case studies was generalized to the autumn season. S-Pol particle-identification fields shows that the microphysical characteristics of IOP2b (IOP8) were representative of the accumulated statistics for $F>1$ ($F<1$) events in the MAP-SOP season. Statistics of the frequency of occurrence of hydrometeors during the season indicate that in unblocked cases, the general background precipitation was stratiform. A deep layer of dry snow lay above a layer of wet snow, which overlaid a layer of light rain. Moderate rain occurred intermittently within this background stratiform structure below the 0°C level. Graupel appeared intermittently above the 0°C level. The graupel particles and moderate rain appar-

ently occurred in convective cells over peaks in the terrain. The statistics show that the graupel generally did not occur in the blocked cases. Those cases had only the background stratiform layering of precipitation, and the layer of precipitation tended to be shallower. This stratiform precipitation could be copious as a result of a prolonged event, as in IOP8, but limited in intensity since the lower layer of air was blocked and did not participate in the lifting and because embedded cells tended not to occur under these more stable conditions. Finally, a conceptual model of orographic precipitation over the Alps has been developed from these observations (Fig. 5.13).

In parallel to the observational study, the performance of a high-resolution mesoscale model (MC2) was documented during the case studies investigated. On the Alpine scale, the precipitation forecast was accurate during IOP2b. The model correctly depicted the airflow and microphysics, but apparently because of smoothing of the topography, the MC2 predicted the graupel maximum over the second terrain peak encountered by the radial flow rather than the first peak. For IOP8, the MC2 forecast atmosphere was less stable than the observed environment. Therefore, the airflow was not blocked through a deep enough layer. The model predicted graupel formation just upwind of the first peak of the terrain. Hence it predicted higher than observed precipitation amounts at the foothills of the Lago Maggiore region. The model appears to produce graupel where the correct combination of airflow and detailed topography are present. Too much smoothing of the topography in the model can lead to misplacements of the graupel production. Incorrect prediction of Froude number or moist stability can lead to prediction of graupel where none occurred.

6.1 Future work

In future work, we will continue the evaluation of the dynamics and microphysics of mesoscale numerical models. In particular, by working with the MC2 research group to rerun individual storms simulations with a higher horizontal resolution, we will test our hypothesis regarding the role individual terrain peaks play on graupel production.

The conceptual model of orographic precipitation that emerged from this thesis will be tested and refined over a different geographic region. The second phase of the Improvement of Microphysical PaRametrizations through Observational Verification Experiment (IMPROVE II) was conducted over the Oregon Cascade Mountains from 26 November - 21 December 2001 (Fig. 6.1). The objective of this project was to verify and improve bulk microphysical parametrizations of orographic precipitation in mesoscale models. Many of the observational assets that were deployed during MAP were also involved in IMPROVE II (e.g. a vertical pointing S-band radar, the dual polarimetric S-Pol radar, Fig. 6.1). In addition, during IMPROVE II, in-situ microphysics observations were collected both by aircraft and ground observers. Therefore, this project provides an extensive dataset that documents the dynamics and microphysics of Pacific Northwest storms over topography and also an opportunity to advance our understanding of orographic precipitation processes in baroclinic storms.

Finally, an evaluation of the representation of orographic precipitation mechanisms in the mesoscale model that was used during IMPROVE II (MM5) will be conducted. By analyzing precipitation types detected by S-Pol and in-situ observations, a validation of the main precipitation growth mechanisms present in the MM5 will be conducted, similar to the MC2 evaluation that was carried on during MAP. The basic plan of our orographic precipitation study is shown in Fig. 6.2. Analysis of the

MAP dataset has led to a conceptual model of orographic enhancement of baroclinic precipitation. The IMPROVEII dataset will be used to test, refine and broaden the conceptual model as necessary. This revised conceptual model will be used as basis for evaluating the performance of the MM5 representation of orographic precipitation over the Cascade Mountains, just as the MC2 performance was evaluated over the Alps.

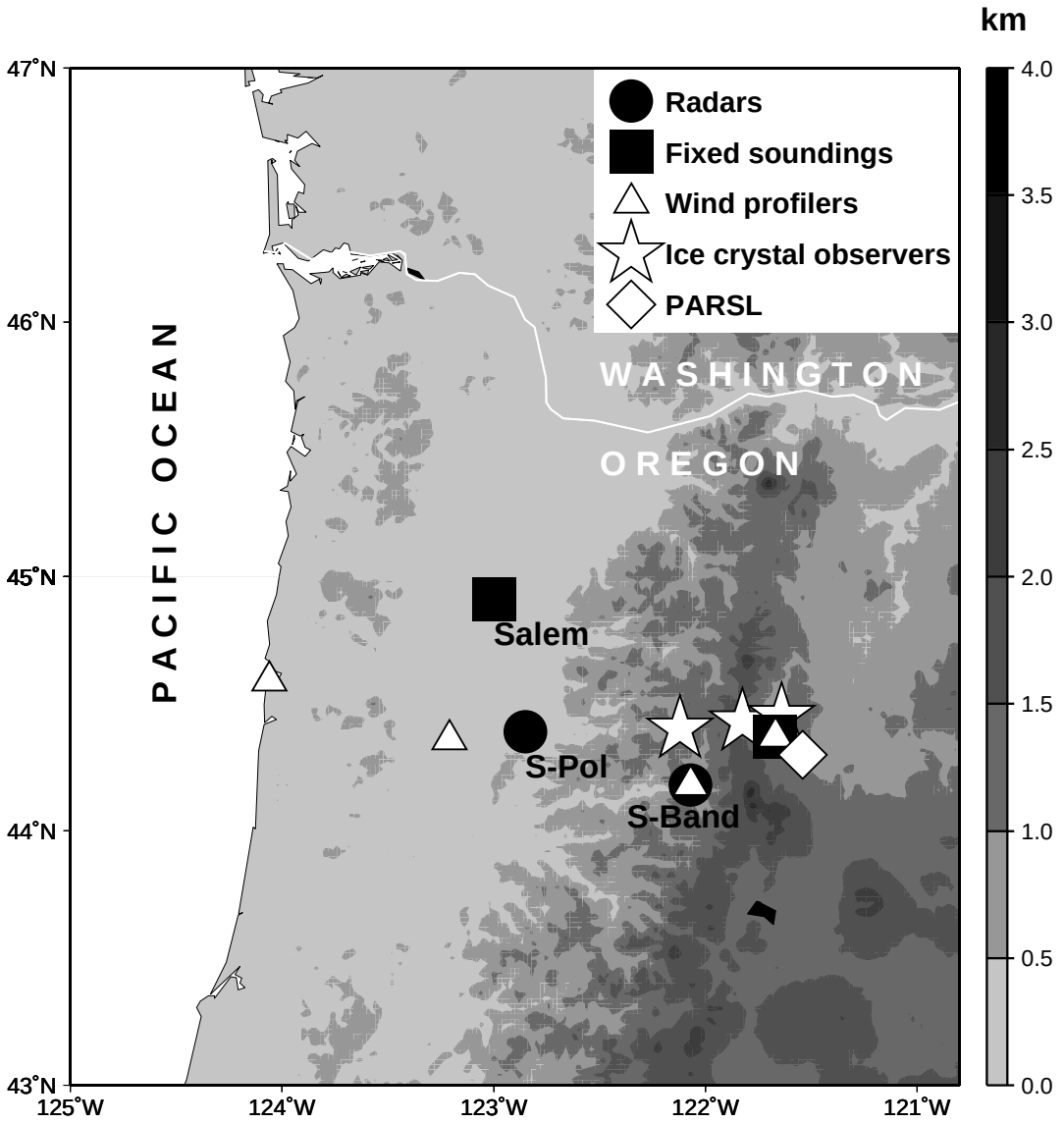

Figure 6.1: IMPROVE II observational area. Western Oregon topography and observational assets. PARSL denotes the location of remote sensing instruments operated by the Pacific Northwest National Lab/Atmospheric Remote Sensing Lab.

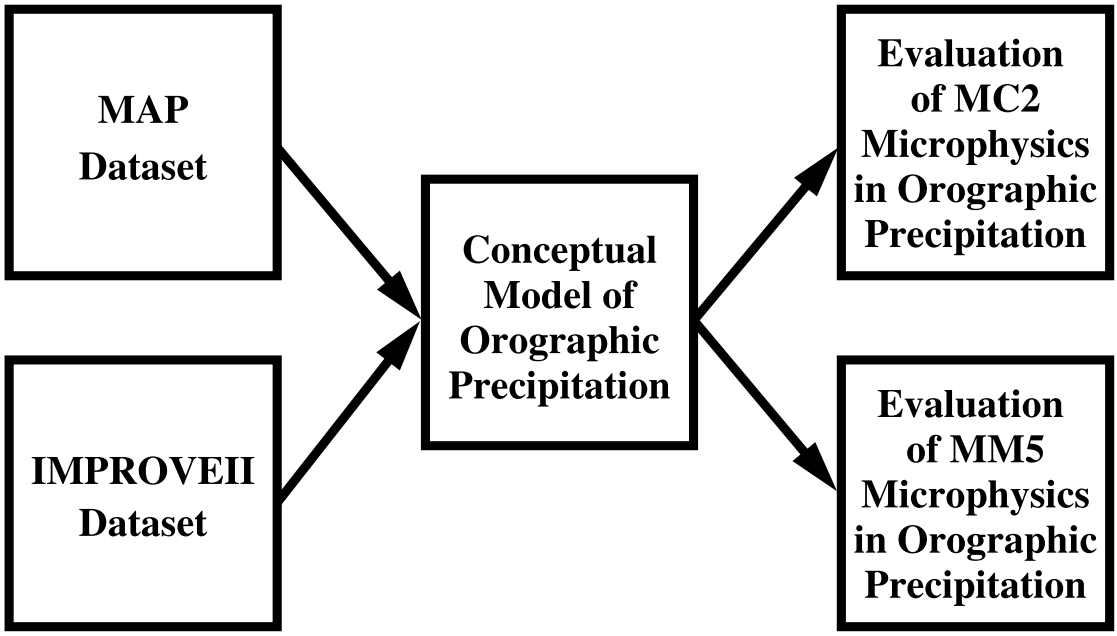

Figure 6.2: Flowchart of the orographic enhancement of precipitation study.

REFERENCES

Benoit, R., M. Desgagne, P. Pellerin, S. Pellerin and Y. Chartier, 1997: The Canadian MC2: A semi-Lagrangian, semi-implicit wideband atmospheric model suited for finescale process studies and simulation. Mon. Wea. Rev., **125**, 2382–2415.

Benoit, R., C. Schär, P. Binder, S. Chamberland, H. C. Davies, M. Desgagne, C. Girard, C. Keil, N. Kouwen, D. Luthi, D. Maric, E. Muller, P. Pellerin, J. Schmidli, F. Schubiger, C. Schwierz, M. Sprenger, A. Walser, S. Willemse, W. Yu, and E. Zala, 2002: The real-time ultrafinescale forecast support during the special observing period of the MAP. Bull. Amer. Meteor. Soc., **83**, 85–109.

Bergeron, T.,1965: On the low-level redistribution of atmospheric water vapor caused by orography. Proc. Int. Conf. Could Physics (suppl.), Tokyo, Japan, 96–100.

Binder, P., and A. Rossa, 1995: The Piedmont flood: Operational prediction by the Swiss Model. Mesoscale Alpine Programme Newsletter, Vol. 2, 12–16.

Bougeault, P., P. Binder, A. Buzzi, R. Dirks, R. Houze, J. Kuettner, R. B. Smith, R. Stienacker, and H. Volkert, 2001: The MAP Special Observing Period. Bull. Amer. Meteor. Soc., **82**, No. 3, 433–462.

Bousquet, O., and B. F. Smull, 2002: Observations and impacts of upstream blocking during a widespread orographic precipitation event. Submitted to the MAP-SOP Special issue of the Quart. J. R. Met. Soc.

Browning, K. A., C. Pardoe, and F. F. Hill, 1975: The nature of orographic rain at wintertime cold fronts. Quart. J. R. Met. Soc., **101**, 333–352.

Buzzi, A., and N. Tartaglione, 1995: Meteorological modeling aspects of the Piedmont 1994 flood. Mesoscale Alpine Programme Newsletter, Vol. 3, 27–28.

Buzzi, A., N. Tartaglione, and P. Malguzzi, 1998: Numerical simulations of the 1994 Piedmont flood: Role of orography and moist processes. Mon. Wea. Rev., **126**, 2369–2383.

Buzzi, A., N. Tartaglione, C. Cacciamani, T. Paccagnella, and P. Patruno, 1995: Preliminary meteorological analysis of the Piedmont flood of November 1994. Mesoscale Alpine Programme Newsletter, Vol. 2, 2–6.

Caracena, F., R. A. Maddox, L. R. Hoxit, and C. F. Chappell, 1979: Mesoanalysis of the Big Thompson storm. Mon. Wea. Rev., **107**, 1–17.

Corbet, J., C. Mueller, C. Burghart, K. Gould, and G. Granger, 1994: Zeb: software for integration, display, and management of diverse environmental datasets. Bull. Amer. Meteor. Soc., **75**, 783–792.

Doswell, C. A., III, C. Ramis, R. Romero, and S. Alonso, 1998: A diagnostic study of three heavy precipitation episodes in the western Mediterranean region. Wea. Forecasting, **13**, 102–124.

Durran, D. R., 1990: Mountain waves and downslope winds. Atmospheric Processes Over Complex Terrain. (W. Blumen, Ed.), Amer. Meteor. Soc., Boston, 59–81.

Durran, D. R., and J.B. Klemp, 1982: On the effects of moisture on the Brunt-Väisälä frequency. J. Atmos. Sci., **39**, 2152–2158.

Ferretti, R., S. Low-Nam, R. Rotunno, 2000: Numerical Simulations of the Piedmont flood of 4-6 November 1994. Tellus, **52A**, 162–180.

Frei, C., and C. Schär, 1998: A precipitation climatology of the Alps from high-resolution rain-gauge observations. Int. J. Climatol., **18**, 873–900.

Frontero, P., L. Lombroso, S. Pugnaghi, and R. Santangelo, 1995: November 1994 Piedmont flood: nowcasting contribution. Mesoscale Alpine Programme Newsletter, Vol. 3, 55–58.

Gabella, M., and R. Mantonvani, 2001: The floods of 13-16 October 2000 in Piedmont (Italy): Quantitative precipitation estimates using radar and a network of gauges. Weather special issue (Water resources and floods), **56**, 337–343.

Hill, F. F., K. A. Browning, and M. J. Bader, 1981: Radar and raingauge observations of orographic rain over South Wales. Quart. J. R. Met. Soc., **107**, 643–670.

Hobbs, P. V., 1975: The nature of winter clouds and precipitation in the Cascade Mountains and their modification by artificial seeding. Part I: Natural conditions. J. Appl. Meteor., **14**, 783–804.

Hobbs, P. V., R. C. Easter, and A. B. Fraser, 1973: A theoretical study of the flow of air and fallout of solid precipitation over mountainous terrain. Part II: Microphysics. J. Atmos. Sci., **30**, 813–823.

Houze, R. A., Jr., 1993: Clouds Dynamics. Academic Press, 573 pp.

Houze, R. A., Jr., C. N. James, and S. Medina, 2001: Radar observations of precipitation and airflow on the Mediterranean side of the Alps: Autumn 1998 and 1999. Quart. J. R. Met. Soc., **127**, 2537–2558.

James, C. N., S. R. Brodzik, H. Edmon, R. A. Houze, Jr. and S. E. Yuter, 2000: Radar data processing and visualization over complex terrain. Wea. Forecasting, **15**, 327–338.

Kong F., and M. K. Yau, 1997: An explicit approach to microphysics in MC2. Atmos.-Ocean, **35**, 257–291.

Lionetti, M., 1996: The Italian floods of 4-6 November 1994. Weather, **1**, 18–27.

Marshall, J. S., and W. M. Palmer, 1948: The distribution of raindrops with size. J. Meteor. **5**, 165–166.

Massacand, A. C., H. Wernli, and H. C. Davies, 1998: Heavy precipitation on the Alpine southside: An upper-level precursor. Geophys. Res. Lett. **25**, 1435–1438.

Mohr, C. G., and R. L. Vaughan, 1979: An economical procedure for Cartesian interpolation and display of reflectivity factor data in three-dimensional space. J. Appl. Meteor., **18**, 661–670.

Paccagnella, T., P. Patruno, and C. Cacciamani, 1995: Operational quantitative precipitation forecast of the Piedmont flood event at the Regional Meteorological Service

of Emilia-Romagna. Mesoscale Alpine Programme Newsletter, Vol. 2, 7–11.

Petterssen, S., 1940: Weather Analysis and Forecasting. McGraw Hill Book Company, Inc., 221–223.

Rogers, R. R., and M. K. Yau, 1989: A Short Course in Cloud Physics. 3d ed. Pergamon Press, 293 pp.

Rotunno, R., and R. Ferretti, 2001: Mechanisms of Intense Alpine Rainfall. J. Atmos. Sci., **58**, 1732–1749.

Rotunno, R., and R. Ferretti, 2002: Comparative Analysis of Rainfall in MAP Cases IOP2b and IOP8. Submitted to the MAP-SOP Special issue of the Quart. J. R. Met. Soc.

Schneidereit, M., and C. Schär, 2000: Idealised numerical experiment of alpine flow regimes and southside precipitation events. Meteorol. Atmos. Phys. **72**, 233–250.

Smith, R. B., 1979: The influence of mountains on the atmosphere. Advances in Geophysics, **21**, Academic Press, 87–230.

Smull, B. F., and O. Bousquet, 2001: Evaluation of real-time MC2 simulation results for a case of significant upstream blocking during MAP. MAP Conf., Schliersee, Germany.

Straka, J. M., D. S. Zrnić, and A. V. Ryzhkov, 2000: Bulk hydrometeor classification and quantification using polarimetric radar data: Synthesis of relations. J. Appl. Meteor., **39**, 1341–1372.

Vivekanandan, J., D. S. Zrnić, S. M. Ellis, R. Oye, A. V. Ryzhkov, and J. Straka, 1999: Cloud microphysics retrieval using S-band dual-polarization radar measurements. Bull. Amer. Meteor. Soc., **80**, 381–388.

Yuter, S. E., and R. A. Houze, Jr., 2002: Microphysical modes of precipitation growth determined by S-band vertically pointing radar in orographic precipitation during MAP. Submitted to the MAP-SOP Special issue of the Quart. J. R. Met. Soc.

Zeng, Z., S. E. Yuter, R. A. Houze, and D. E. Kingsmill, 2001: Microphysics of the rapid development of heavy convective precipitation. Mon. Wea. Rev., **129**, 1882–1904.

Appendix A

POLARIMETRIC RADAR DATA

A linear polarimetric radar normally transmits and receives horizontally and vertically polarized radiation. The linear polarimetric observables depend (and hence also give information) on the physical characteristics of the hydrometeors, such as particle size, shape, thermodynamic phase and spatial orientation. The physical characteristics of the main precipitation particles relevant to this thesis are:

Graupel: Formed by ice particles that have grown by riming to such an extent that is not possible to recognize the original shape of the ice crystal. It has an approximately spherical shape.

Hail: Formed by an extreme case of growth of ice particles by riming. According to Straka et al. (2000), the orientation of hail when falling is not fully understood. However, it has been reported that hailstones fall with tumbling motion, producing a spherical statistical shape.

Dry snow: Formed by randomly oriented ice particles with a low dielectric constant.

Wet snow: It has a outer layer of water characterized by a large complex refraction index.

Rain: Raindrops become more oblate at they increase their size and they tend to fall with its largest axis horizontally oriented.

The cross-polar and co-polar reflectivity factors are some of the most important measurements made with a polarimetric radar. The cross-polar reflectivity factor

is obtained by transmitting radiation in one direction and measuring the return in the direction orthogonal to the emitted pulse. The main parameters measured by a polarimetric radar are: reflectivity (dBZ), differential reflectivity (ZDR), linear depolarization ratio (LDR), and specific differential propagation phase (K_{DP}), given by:

$$dBZ = 10\ log_{10}(Z_{HH}) \tag{A.1}$$

$$ZDR = 10\ log_{10}\left(\frac{Z_{HH}}{Z_{VV}}\right) \tag{A.2}$$

$$LDR = 10\ log_{10}\left(\frac{Z_{HV}}{Z_{HH}}\right) \tag{A.3}$$

$$K_{DP} = \frac{d\Phi_{DP}}{dr} \tag{A.4}$$

where Z_{HH}, Z_{VV}, Z_{HV} are the horizontally transmitted/horizontally received, vertically transmitted/vertically received, and horizontally transmitted/vertically received reflectivity factors, respectively. Φ_{DP} is the differential propagation phase shift (i.e. the difference between the propagation phase shift of the radar wave at horizontal and vertical polarization during two way propagation) and r is range from the radar. The different hydrometeors produce distinct signatures on one or more of the polarimetric variables. Table A.1 shows the range of values that each hydrometeor type produces in the different polarimetric variables:

dBZ**:** Depends on number concentration and particle diameter to the sixth power. Hence the larger particles (e.g. hailstones) produce the stronger signals.

ZDR**:** It is proportional to the ratio between the horizontal co-polar and the vertical co-polar reflectivities. The oblateness and orientation when falling of the raindrops produces a signal. Furthermore, this signal is proportional to the size of

the raindrops. Wet snow produces a strong return. Spherical hail produces low values, so does dry snow due to its low dielectric constant.

LDR: A pulse emitted in the horizontal direction impinging over a spherical particle will excite a response in all directions, however given the symmetry of the particle, all the vertical responses will cancel each other, giving a null value of Z_{HV} and making $LDR \rightarrow -\infty$. However if the particle does not have an axis of symmetry in the vertical direction (for example a titled column-shaped ice crystal) then the vertical responses excited by the horizontal pulse will not cancel each other and LDR will have a value different from $-\infty$. Rain has symmetric shapes and small canting angles which gives low LDR values. Dry snow also produces small values since it has a low dielectric constant. Irregular graupel and hail have a strong LDR signature, as well as wet snow due to its outer water layer.

K_{DP}: According to Straka et al. (2000), in a volume filled with horizontally oriented hydrometeors (e.g. rain), a horizontally polarized wave has larger phase shifts (per unit length) and propagates more slowly than a vertically polarized wave (the opposite holds for a vertically oriented hydrometeor). K_{DP} measures the difference between propagation constants for horizontally and vertically polarized waves. Hence, it can discern between statistically isotropic and anisotropic hydrometeors. Isotropic hydrometeors produce similar phase shifts for horizontally and vertically polarized waves. In general the magnitude of K_{DP} increases with oblateness and with dielectric constant. For hail K_{DP} has a small value due to its small dielectric constant, low concentration and tumbling motion when falling (which make it statistically isotropic). Graupel fulfills similar conditions as hail. K_{DP} has a strong signal when statistically anisotropic hydrometeors like rain are larger than 1 mm.

Table A.1: Polarimetric Radar Variables$^{\diamond}$

Hydrometeor	dBZ (dBZ)	ZDR (dB)	LDR (dB)	K_{DP} ($^{\circ}km^{-1}$)
Graupel	High (20–50)	Low (-0.5–2)	High (< -20)	Low (0–1.5)
Hail*	Very High (45–80)	Low (-2–0.5)	High (> -26)	Low (-0.5–1)
Dry snow	Low (< 35)	Low (0–1)	Low (< -25)	Low (0–0.2)
Wet snow	High (< 45)	Very High (0.5–3)	High (-10 to -20)	High (0–0.5)
Heavy rain†	High (44–60)	High (> 2)	Low (-30 to -25)	High (> 0.6)
Light rain‡	Low (< 20)	Low (0–0.7)	Low (< -32)	Low (0–0.03)

* D$>$ 5 mm, † D$>$ 2 mm, ‡ D$<$ 1 mm

$^{\diamond}$Values based on Straka et al. (2000)